Modulated Model Predictive Control and Fault Diagnosis for the Cascaded H-Bridge (CHB) Inverters

MODULATED MODEL PREDICTIVE COTNROL AND FAULT DIAGNOSIS FOR THE CASCADED H-BRIDGE (CHB) INVERTERS

BY

YUE PAN, B.Eng.

A THESIS

SUBMITTED TO THE DEPARTMENT OF ELECTRICAL & COMPUTER ENGINEERING

AND THE SCHOOL OF GRADUATE STUDIES

OF MCMASTER UNIVERSITY

IN PARTIAL FULFILMENT OF THE REQUIREMENTS

FOR THE DEGREE OF

MASTER OF APPLIED SCIENCE

Master of Applied Science (2023) McMaster University

(Electrical & Computer Engineering) Hamilton, Ontario, Canada

TITLE: Modulated Model Predictive Control and Fault Diagnosis for the Cascaded H-Bridge (CHB) Inverters

AUTHOR: Yue Pan

Bachelor of Engineering

McMaster University, Hamilton, ON, Canada

SUPERVISOR: Dr. Mehdi Narimani

NUMBER OF PAGES: xiv,133

Abstract

Multilevel inverters (MLI) have been widely applied in medium and high voltage applications for their advantages in high quality of output waveforms. Among various multilevel topologies, cascaded H-bridge (CHB) inverters have attracted more attentions for its modular structure, which simplifies the design and implementation. In addition, the modularity of CHB also expands diverse power ratings without many changes in the hardware setup. In a CHB inverter, the AC output voltage can be produced at different voltage levels depending on the number power cells that are cascaded at the output.

To produce the AC output voltage, different modulation schemes and control algorithms have been studied and applied to the CHB inverter. Model predictive control (MPC) has been widely employed among all control algorithms in multilevel topologies due to their advantages such as good dynamic performance, multiple control targets, inclusion of nonlinearity, and flexibility to add more performance objectives. However, one disadvantage of the MPC is that the switching frequency is variable compared with other modulation schemes. Therefore, a new MPC method called modulated model predictive control (M^2PC) has been researched to obtain a fixed switching frequency, which improves the harmonic spectrum of load currents and simplifies the filter design.

In the modulated model predictive control, the mathematical model is obtained by electrical model of the system. It means that the operation of the M^2PC algorithm relies on the accuracy of the given parameters and model. If there is an error in parameters and model, the performance of the control will be affected negatively. To solve this problem, modulated model-free predictive control (M^2FPC) algorithm has been introduced. With this method, the mathematical model is established with measured values instead of given values and model.

Reliability is one of the most important issues in the design of power converters. However, the failure of power switches will lead to the distortion of load currents and voltage waveforms. Also, the distortion in load currents and voltage waveforms causes power imbalance between faulty and healthy phases. To reduce the negative effects of IGBT failure in power converters, the faulty power cells should be found and isolated. Therefore, fault detection and localization algorithm (FDL) should be introduced to detect the fault in power converters and localize the faulty power switches.

FDL algorithm based on the given M^2PC scheme is proposed in this thesis for the CHB inverter to make the system more reliable. The FDL algorithm utilizes the phase voltages and load currents to detect the open fault in the CHB inverter and localize the single and

multiple open switches by measuring the expected and actual phase voltages. With the faulty information, the faulty power cell can be isolated, and the fault-tolerant control can be applied to make the system work normally even though there is an open fault.

In this thesis, without losing the generality, a seven-level CHB inverter is considered where there are three power cells in each phase. The M^2PC algorithm was introduced to obtain the fixed switching frequency with the design of possible voltage vector set and carrier phase-shifting modulation. Based on the proposed M^2PC algorithm, the FDL algorithm is designed to detect and localize the open switches to improve the system reliability.

The theoretical analysis and simulation results validate the feasibility of the proposed M^2PC algorithms and open fault diagnosis scheme. All possible open-circuit scenarios in power cells are discussed and the M^2PC-based FDL algorithm has been verified.

Experimental results verify the feasibility of the proposed M^2PC. The experimental result of M^2PC algorithm is presented to verify its operation. Also, diverse open scenarios can be diagnosed in the experiments.

Acknowledgements

Firstly, I should express sincere gratitude to my supervisor, Dr. Mehdi Narimani, for his support, guidance, and professional suggestions. He offers me this precious research opportunity and helps me immensely in my academic work. For his work and appreciation, I have the chance to gain knowledge and experience in my research work.

I want to thank my colleagues in HiPEL for their help in my research. Dr. Zhituo Ni always shares his ideas and experience in my research work, which makes me learn more during my graduate study. Also, Dr. Ahmed Abuelnaga also shares his experiment experience throughout his graduate study with me. I am grateful for their assistance in the hardware setup and the knowledge I increase.

Finally, I need to thank my parents. They always support and encourage me in my research work. In my graduate study, they offer me everything I need, and their efforts cannot be ignored.

Contents

List of Tables

List of Figures

Chapter 1

Introduction

Medium voltage (MV) converters have been under research and study from mid-1980 when the gate-turned-off (GTO) thyristors becoming available [1], [2]. With the advent of other state-of-the-art switching devices, like insulated gate bipolar transistor (IGBT), motor drives are improved for the higher voltage and power applications due to smaller switching loss, ease of control signals, and advanced switching characteristics. With the application of motor drives, the frequency and amplitude of output voltages can be set with fixed three-phase input voltages. Therefore, the speed and torque of a motor can be controlled.

Medium voltage drives cover the voltages from 2.3kV to 15kV. In addition, the power rating of MV drives ranges from 0.2MW to 20MW. In recent years, medium voltage motor drives have been widely applied in various applications, including high-speed railway systems, pumps in petrochemical industries, traction applications in transportation systems, rolling machines in mining industries, reactive power compensation, renewable conversion systems and water delivery systems [2]-[4].

According to the study in [5], MV drive market is predicted to increase significantly worldwide and the fastest growing market is Asia Pacific. The MV AC motor drive market

is expected to reach $3.3 billion by 2031. In [6], most MV AC motor drives need the multiphase transformers at the front end and multilevel converters to eliminate the current harmonics. MV drives are always competitive at the high rated power. With the motor drive, the motor speed and torque should be adjusted casually, and the soft start of the system should be obtained. Therefore, motor drives should be developed to reduce the maintenance cost, extend the lifetime, and optimize the energy efficiency.

There are various motor drive products in the market. In MV motor drives, diverse power converters are applied with corresponding control schemes. Every topology has its advantages but with some limitations [7]. Many companies are proficient in the design of motor drives. The manufacturers and products are shown in Table.1.1. From the survey on MV drive products, many products are designed with cascaded H-bridge and neutral point topologies.

TABLE 1.1 MV DRIVE PRODUCTS

Companies and Products	**Converter Topology**	**Power Range(MVW)**
Rockwell Automation PowerFlex 6000[8]	Cascaded H-Bridge(CHB)	0.32-5.6
Schneider Electric ATV6000[9]		0.16-20
Siemens GH180[10]		0.3-60
Toshiba T300MV2[11]	Neutral Point Clamped(NPC)	0.22-8.22
Toshiba MX2-60[12]		2.61-4.47
ABB ACS1000[13]		0.315-5
Eaton SC9000 CI[14]		0.075-1.816
Alstom VDM6000 Synphony[15]	Flying Capacitor(FC)	Air:0.3-3 Water:2.2-8
Alstom VDM5000[15]	Two-level Voltage Source Inverter(VSI)	1.4-7.2

The structure of MV AC motor drives always includes four important components: transformer, rectifier, DC filter, and inverter. The structure of MV motor drive is shown in Fig.1.1. In the line- and motor-side, the filter can be added to improve the waveforms.

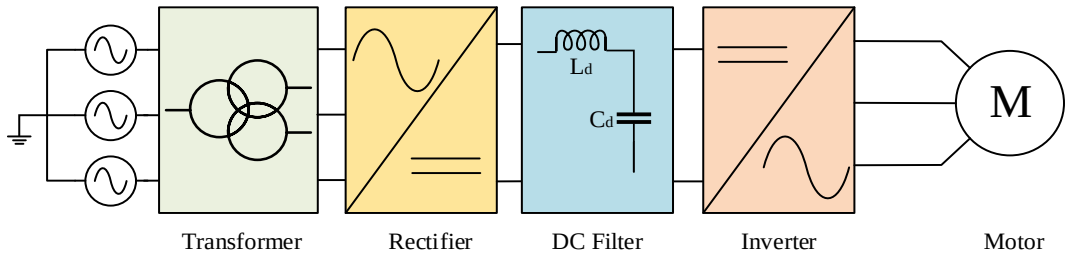

Fig.1.1. Structure of A MV AC Motor Drive [7]

In a motor drive, the three-phase transformer is used to eliminate the current harmonics in the line side. With the rectifier, the DC voltage can be generated and the voltage ripple can be mitigated with a DC filter. Finally, the output AC voltage can be controlled to make the motor work normally at different speed and torque.

There are several technical requirements and challenges in the design of motor drives [7] which requirements in the line side, challenges in the motor side, and switching devices:

1. Line Side Requirements

a) Reduce large current distortion to comply with the standard.

b) Improve input power factor.

2. Motor Side Challenges

a) Reduce *dv/dt* and common mode voltage.

b) Improve waveform quality to avoid motor derating.

c) Suppress LC resonance.

3. Switching Devices Constraints

a) Apply low switching frequency to reduce the switching loss.

b) Implement a reliable voltage equalization scheme to protect switching devices.

In the AC/DC section, multi-pulse diode rectifier can be applied to improve the line current quality. Common multi-pulse rectifiers are 12-pulse, 18-pulse, and 24 pulse rectifiers. The typical configurations of these multi-pulse rectifiers are shown as Fig.1.2. A phase-shifting transformer with several secondary windings is applied into rectifiers to provide the DC voltage and make the line-side currents meet the THD requirement.

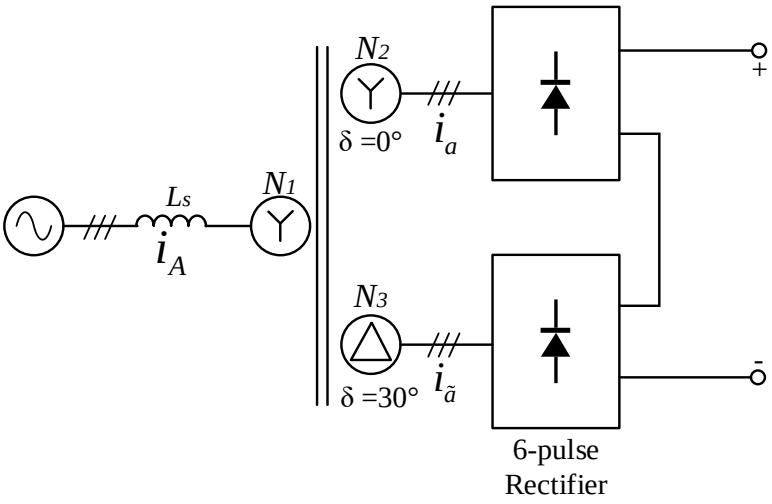

(a) 12-pulse Rectifier

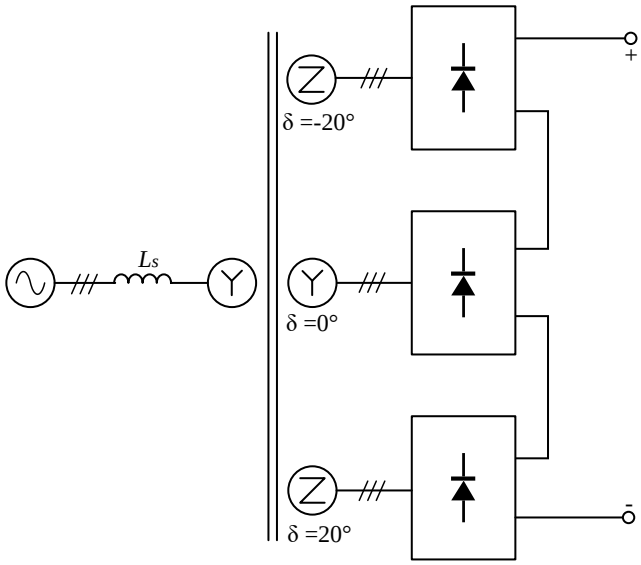

(b) 18-pulse Rectifier

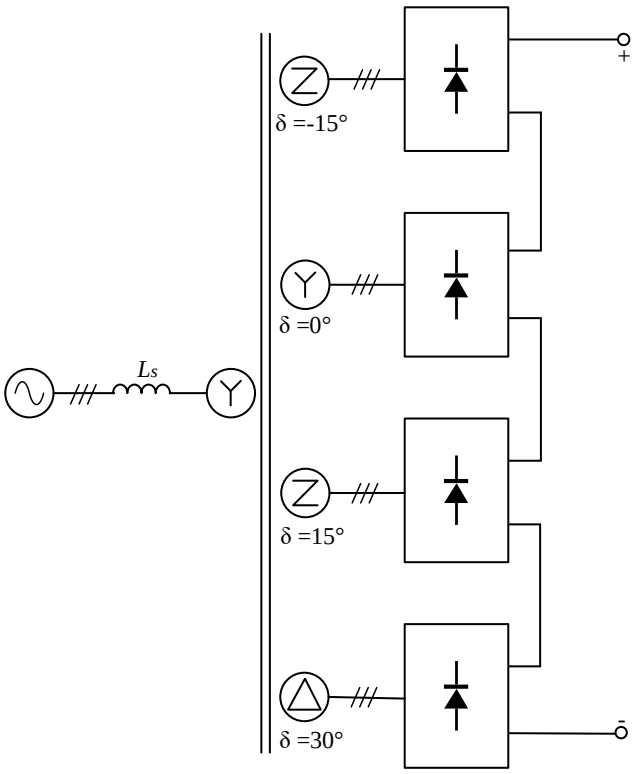

(c) 24-pulse Rectifier

Fig.1.2. Multi-pulse Rectifiers [7]

For the 12-pulse rectifier, the turns ratio between N_2 and N_3 in the transformer can be subject to [7]:

$$\frac{N_1}{N_2} = 2 \text{ and } \frac{N_2}{N_3} = \frac{1}{\sqrt{3}} \quad (1.1)$$

With this ratio, amplitudes of referred currents, $i_a^{'}$ and $i_{\tilde{a}}^{'}$, have the same value and the harmonics of line currents can be offset. The Fourier expressions of referred currents are as given:

$$i_a^{'} = \frac{\sqrt{3}}{\pi} I_d (sin\,\omega\, t - \frac{1}{5} sin\, 5\, \omega t - \frac{1}{7} sin\, 7\, \omega t + \frac{1}{11} sin\, 1\, 1 \omega t + \frac{1}{13} sin\, 1\, 3 \omega t$$
$$- \frac{1}{17} sin\, 1\, 7 \omega t - \frac{1}{19} sin\, 1\, 9 \omega t + \cdots) \quad (1.2)$$

$$i_{\tilde{a}}^{'} = \frac{\sqrt{3}}{\pi} I_d (sin\,\omega\, t + \frac{1}{5} sin\, 5\, \omega t + \frac{1}{7} sin\, 7\, \omega t + \frac{1}{11} sin\, 1\, 1 \omega t + \frac{1}{13} sin\, 1\, 3 \omega t$$
$$+ \frac{1}{17} sin\, 1\, 7 \omega t + \frac{1}{19} sin\, 1\, 9 \omega t + \cdots) \quad (1.3)$$

where I_d is the value of DC output current in the rectifier. With the referred current values, the line current i_A is expressed by:

$$i_A = i_a^{'} + i_{\tilde{a}}^{'} = \frac{\sqrt{3}}{\pi} I_d (sin\,\omega\, t + \frac{1}{11} sin\, 1\, 1 \omega t + \frac{1}{13} sin\, 1\, 3 \omega t$$
$$+ \frac{1}{23} sin\, 2\, 3 \omega t + \frac{1}{25} sin\, 2\, 5 \omega t) \quad (1.4)$$

From the equation, the 5th and 7th harmonics in line currents are cancelled with a 12-pulse rectifier. With the 18- and 24-pulse rectifiers, more harmonics can be eliminated, and line-side requirements can be met.

The design of a suitable inverter is necessary to control the output AC current.

In the MV motor drive products, multilevel topologies, including CHB, NPC and FC topologies, are widely applied for high power applications due to its advantages in high quality of output currents by using more DC voltage levels [16]. Output voltage is synthesized by switching between several voltage levels. Compared with only two voltage levels in conventional two-level voltage source inverter (VSI), the output waveforms are smoother with more voltage levels. Because of the improvement in harmonic spectrum, multiple voltage levels result in smaller *dv/dt*, smaller common mode voltage, and lower switching frequency.

There are some classic multilevel topologies as shown in Fig.1.2:

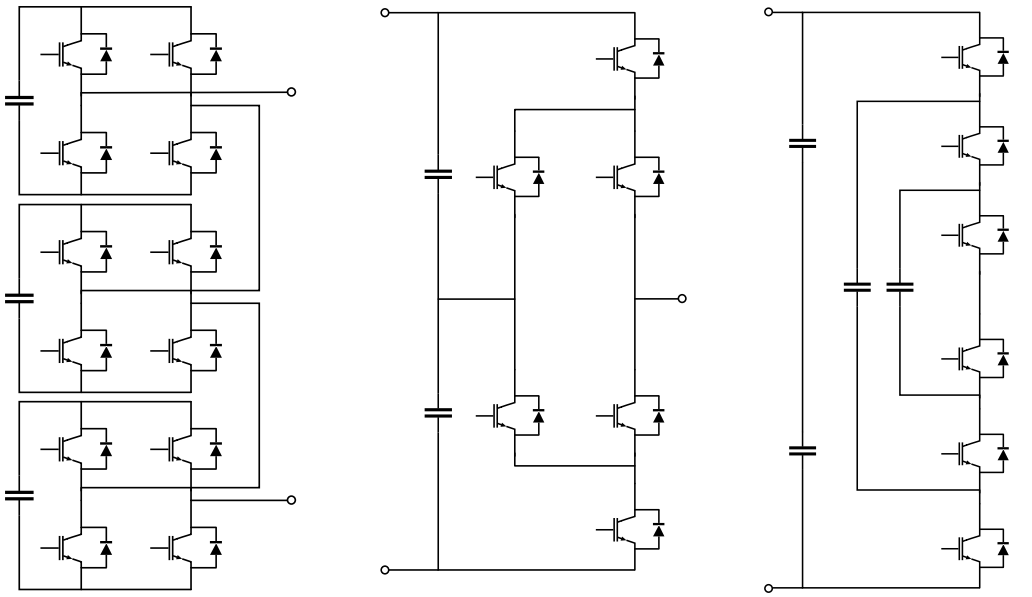

(a) CHB Inverter (b) NPC Inverter (c) FC Inverter

Fig.1.3. MV Multilevel Inverter Topologies [7]

Multi-pulse diode rectifiers and multilevel inverters can help to meet the requirements in the line and motor sides and make them suitable for MV motor drives.

1.1 Research Objective

The cascaded H-bridge inverters attracted much attention in the design of MV motor drives for its modular and scalable structure. It is composed of the series connection of H-bridge power cells. The structure of the CHB inverter features the advantages as [17]:

1) Convenient extension of the power cells
2) Easy design of fault-tolerant control scheme for its modular structure and redundant switching states
3) No need for capacitor voltage balancing, which is obtained with CHB rectifier.

In the power cell of each phase, the three-phase rectifier is utilized to produce the isolated DC voltage. The conventional diode rectifier is shown as Fig.1.4(a). However, the disadvantage of diode rectifier is that the power flow is unidirectional. The power can only flow from the source to the load. Some applications, including downhill conveyors, cranes, and hoists, require bidirectional power flow [18]. Then, the regenerative power cell should be introduced in these applications as shown in Fig.1.4(b). In this thesis, the DC voltage of each power cell is provided by a three-phase diode rectifier.

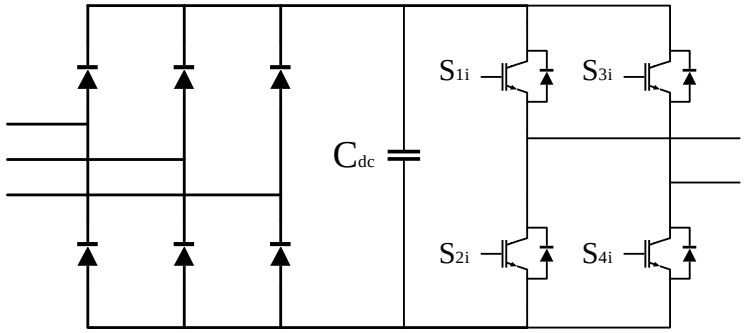

(a) Non-regenerative Power Cell

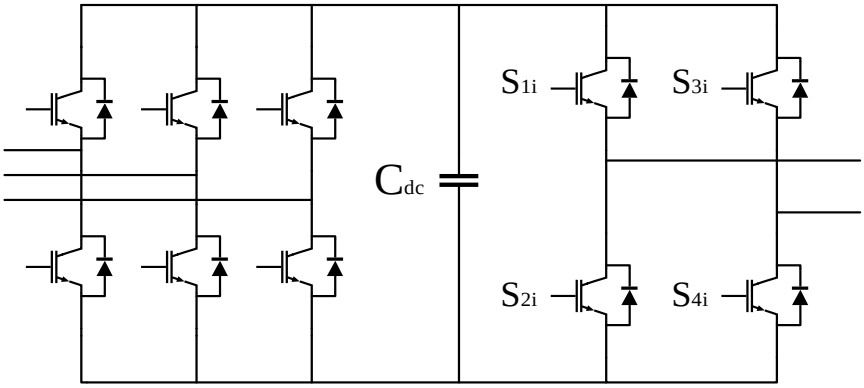

(b) Regenerative Power Cell

Fig.1.4. Structure of Power Cell

In recent years, several modulation schemes have been studied for CHB inverters: (1) sinusoidal PWM (SPWM) scheme (2) selective harmonic elimination (SHE)scheme, and (3) space vector modulation (SVM) [19]. In the control loop, PI, PR and PIR controllers are applied to control the load currents [20]. Compared with conventional modulation algorithms, finite control set model predictive control (FCS-MPC) has also been widely applied in various multilevel converters for its advantages of good dynamic performance, good inclusion for nonlinearity, simple control structure, and multi-objective control [21]-[22]. FCS-MPC predicts the load currents with the mathematical model and compares all

predicted values with reference values to find the optimal switching signals. However, one concern of conventional FCS-MPC algorithm is that the switching frequency is variable [23]-[24]. Therefore, in [25] and [26], modulated model predictive control(M^2PC) has been proposed which can make the motor drive operate at a constant switching frequency. With the fixed switching frequency, the filter is convenient to design, and the current waveform can be improved.

One drawback of the MPC algorithm is that the control performance relies on the accuracy of the parameter and the model [27]. It means that if there is any mismatch in the parameter and model, the deviation in the output currents is large. Under this circumstance, model-free predictive control (MFPC) is an alternative algorithm, which uses data-driven models and avoids the use of explicit model [28]. This algorithm applies a linear model and the prediction requires the observation values in former time intervals. An autoregressive with exogenous input (ARX) model is selected as the prediction model for output currents in [27]. It shows a good performance in the closed-loop control. In the ARX model, the measurement values of phase voltages and load currents are needed.

Coefficients in the ARX model should be estimated and the model is established. Considering the uncertainty of the parameters and model, least square (LS) is applied to calculate the coefficients in the ARX model. However, the LS algorithm needs to calculate the inverse matrix in every sampling time, which increases the computation burden in digital signal processor (DSP). In this thesis, a recursive least square (RLS) is proposed to estimate the coefficients in the ARX model to simplify the algorithm.

Another concern of power converters is the fault detection of power switches, including short-circuit (SC) and open-circuit (OC) faults. [29] shows that 38% of faults in the power converters are from semiconductor failure. One typical cause of SC fault is the high temperature in the switches generated by power consumption [30]. In [31], short switches can be detected by measuring the drain-to-source voltages in MOSFET or collector-to-emitter voltage in IGBT. For OC fault, the main causes are the failure of gate drivers and lift-off of bond wires [32]. Gate driver failure occupies 15% among all electronic failure [33]. Among the two fault situations, SC fault is serious and can be detected by the gate drivers, and the system should be shut down immediately. In this thesis, only OC fault scenarios are discussed.

To improve the reliability of MV motor drives, a fault-tolerant control scheme should be applied to the CHB topology after fault occurs. The framework of fault-tolerant scheme is shown in Fig.1.5. Therefore, the faulty power cell should be identified and isolated from the motor drives. Under this circumstance, the fault-tolerant control can make the motor work under faulty condition.

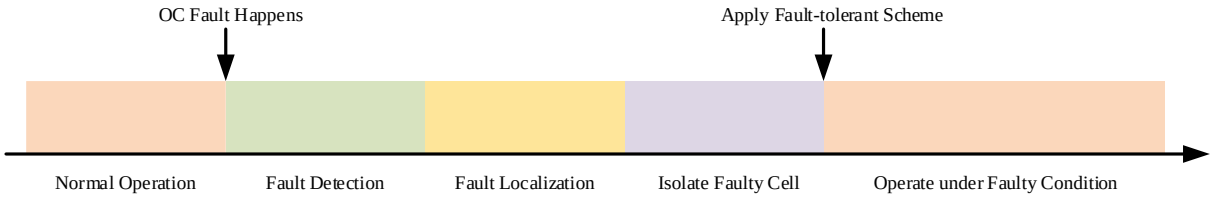

Fig.1.5. Framework of Fault-tolerant Control Scheme [34]

The research objective of this thesis work is to realize the fault diagnosis based on M^2PC algorithm in CHB inverters. This work introduces the proposed M^2PC algorithm with fixed switching frequency. Then, the fault detection and localization (FDL) algorithm

is introduced to detect and localize the open switch fault in CHB topology. In the proposed FDL algorithm, phase voltage and load current sensors are needed. The feasibility of the two algorithms is validated by simulation results with MATLAB/Simulink. Finally, experimental results verify the operation of M^2PC and FDL algorithms.

1.2 Contributions

The contributions of the presented work can be outlined as follows:

- A review of CHB converter has been done and corresponding modulation schemes are discussed. Also, FDL algorithms are reviewed.
- MPC algorithms are studied in terms of performance, advantages, and drawbacks of each method.
- Modulated MPC has been proposed and developed for a CHB inverter, and its advantages compared with the conventional MPC algorithm.
- A modified model-free predictive control (M^2FPC) algorithm is proposed and developed for a CHB inverter. Compared with other M^2PC algorithms, it utilizes the RLS algorithm for current prediction. The RLS algorithm has fast convergence speeds and the current prediction model is built quickly. It's performance under parameter mismatch is also compared with the M^2PC algorithm. In addition, the simulation and experimental results are presented to verify its feasibility.
- A new FDL algorithm to detect and localize the open switch fault in the CHB motor drive is proposed. The performance analysis and principles of the proposed FDL scheme are provided. Simulation results can validate the M^2PC-based FDL algorithm in a CHB inverter.

1.3 Publications

- Yue Pan, Zhituo Ni, Mehdi Narimani，Margarita Norambuena, Jose Rodriguez, " Dead-Time Compensation for Model-free Predictive Control in Multilevel Inverters," in 2023 IEEE International Conference on Predictive Control of Electrical Drives and Power Electronics, in publication, June 2023.
- Yue Pan, Zhituo Ni, Ahmed Abuelnaga, Mehdi Narimani, Jose Rodriguez, " Fault Diagnosis of Cascaded H-Bridge Inverter Using Model Predictive Control," in 2023 IEEE International Conference on Predictive Control of Electrical Drives and Power Electronics, in publication, June 2023.

1.4 Thesis Structure

The thesis is structured as follows:

Chapter 2 introduces the CHB topology, including the structure and the operation of CHB inverter. Then, the conventional control algorithm, SPWM modulation in CHB inverter will be reviewed.

Chapter 3 provides the conventional model predictive control algorithm for a CHB inverter. The method of current prediction and selection of optimal switching signals will be introduced.

Chapter 4 proposes a M^2PC algorithm based on conventional FCS-MPC in CHB inverter. The definition of the voltage set in the α-β coordinate is introduced and optimal voltage vector is obtained with the cost function. The simulation and experimental results of the proposed M^2PC algorithm are provided in this chapter.

Chapter 5 analyzes the model-free predictive control applied in the proposed M^2PC algorithm. This chapter proposes a method of designing the mathematical model with the measured values in several sampling times by RLS algorithm. The simulation results with RL and PMSM are provided. Also, the performance of M^2PC and M^2FPC algorithms is compared under parameter mismatch.

Chapter 6 analyzes the FDL algorithm based on M^2PC algorithm. Firstly, a comprehensive background of the FDL algorithm is provided. This chapter will introduce the details of a new FDL algorithms and analyze effects of various open fault scenarios. Then, the faulty situations are categorized by common and special cases. The FDL algorithm based on the two situations will be validated with simulation results. Simulation results also verify the feasibility of the FDL algorithm.

Chapter 7 provides the experimental results of M^2PC and M^2FPC algorithms. The waveforms of load currents under steady-state and dynamic performances are given. Also, their performances under parameter mismatch are compared. From the experiments, the feasibility of M^2PC and M^2FPC algorithms is validated.

Chapter 8 will provide the conclusion of the thesis and future works to do based on current research work.

Chapter 2

Cascaded H-Bridge (CHB)Inverters

2.1 Structure of a Cascaded H-Bridge (CHB) Inverter

H-bridge inverter features a simple structure and can be connected in series to produce multilevel AC voltage at the output with better quality. The inverter with cascaded structure is called cascaded H-bridge (CHB) inverter. The CHB inverter has several advantages such as scalability, modularity, redundancy in switching states, and better output waveforms. The CHB inverter is widely applied in medium voltage systems.

A typical structure of a CHB motor drive is shown in Fig. 2.1. Fig.2.1(b) shows the structure of a power cell. In CHB inverters, DC isolated voltages are produced by a multi-pulse diode rectifier. Typically, IGBT is selected for the power switches. The output phase voltage is the summation of voltage of all power cells in one phase.

For the non-regenerative power cells as shown in Fig. 2.1(b), there are three components including; diode rectifier, DC capacitor, and H-bridge inverter. Diode rectifier is to convert the three-phase AC voltage to DC voltage. DC capacitor is used to reduce the voltage ripples and obtain the stable DC voltage. With the H-bridge inverter, the DC voltage

can be converted to AC output voltage. Finally, all power cells in one phase are connected to provide multilevel output voltages and have small voltage stress in switching devices.

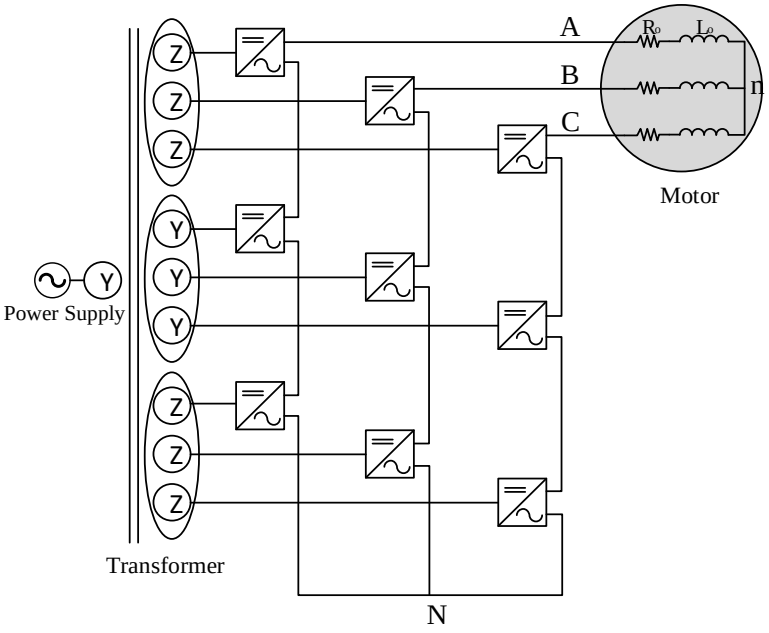

(a) Seven-level CHB drive

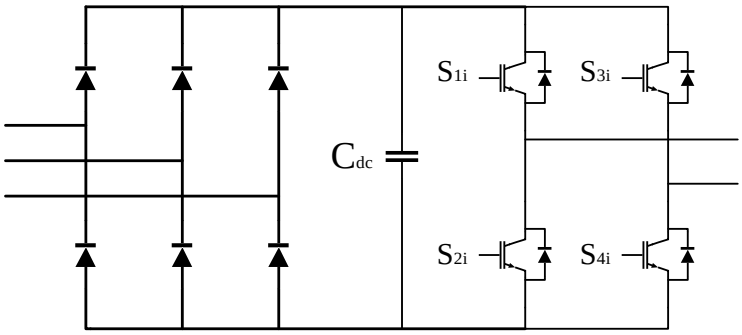

(b) Non-regenerative Power Cell

Fig.2.1. Seven-level CHB Drive Topology

In the regenerative power cell, diode rectifier has been replaced with the active-front-end rectifier. Compared with non-regenerative power cells, regenerative power cell has advantages as [35]-[37]: (1) bidirectional power flow between motor and grid, (2) improve the harmonic profile in the secondary side of the transformer and a phase-shifting transformer is not required, (3) regulate DC voltages and reduce DC voltage ripples, and (4) improve the displacement power factor.

In the primary side, the phase-shifting transformer should be applied to: (1) reduce low-order harmonics in the line currents, (2) isolate the input voltages, (3) reduce the common mode voltage stress, and (4) adjust the input voltage by modifying the turns ratio. In this thesis, without losing the generality, a 7-level CHB topology (three cells per phase) along with a 18-pulse diode rectifier are employed.

2.2 Operation and Modulation Scheme of CHB Inverters

On the motor side, a single-phase H-bridge inverter as shown in Fig. 2.2 is applied and cascaded with other power cells to provide voltage levels. The inverter includes two legs and two IGBT devices in each leg. The constant input voltage V_{dc} is obtained by the diode rectifier in the power cell.

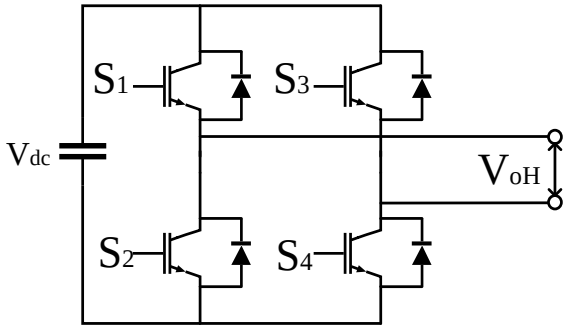

Fig.2.2 Structure of Single-phase H-Bridge Inverter

As discussed above, sinusoidal pulse-width modulation (SPWM), selective harmonic elimination pulse-width modulation (SHE-PWM), and space vector modulation (SVM) typically employed to control H-bridge switches. The switching signals of IGBTs in the same leg are complementary, which means only switching signals of S_1 and S_3 should be determined in one H-bridge. SPWM algorithm is the common modulation scheme. For the H-bridge inverter, there are two common SPWM modulation schemes: unipolar and bipolar modulations.

Fig.2.3 shows the typical waveforms of a single-phase H-bridge inverter with bipolar modulation. In this case, the modulation index m_a is 0.8 and the frequency modulation index m_f is 15. V_m is the modulation waveform and V_{cr} is the carrier waveform. S_{c1} and S_{c3} are control signals for the upper switches S_1 and S_3. The two control signals are generated by the comparison between V_{cr} and V_m. Lower switches are complementary with upper

switches. For the output voltage, the output voltage can be determined by $V_{oH}=(S_{c1}-S_{c3})\ V_{dc}$. The output voltage in each power cell is shown in Table.2.1.

TABLE 2.1 OUTPUT VOLTAGE IN SINGLE-PHASE H-BRIDGE

S_{c1}	S_{c3}	V_{oH}
0	0	0
0	1	$-V_{dc}$
1	0	V_{dc}
1	1	0

In this case, the output voltage waveform switches between $+V_{dc}$ to $-V_{dc}$ in the whole period. Therefore, the modulation scheme is bipolar modulation [7].

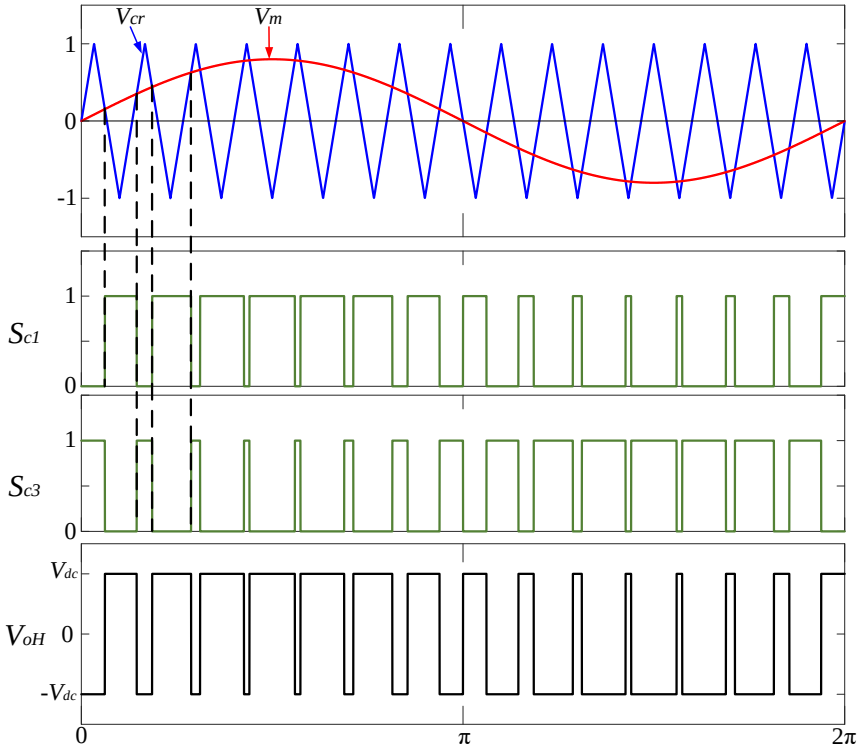

Fig.2.3. A Typical Bipolar Modulation Scheme (m_a=0.8, m_f=15)

Fig.2.4 shows the waveforms of H-bridge with unipolar modulation. For unipolar modulation, there are two types of modulation waveforms, V_m and V_{m-}. The two modulation waveforms should be compared with triangular carrier waveform V_{cr}. Therefore, the control signals of S_1 and S_3 , S_{c1} and S_{c3}, are provided. The two upper switches do not commutate simultaneously. For this reason, the output voltage V_{oH} switches between 0 and $+V_{dc}$ in the positive cycle and $-V_{dc}$ in the negative cycle. Therefore, the modulation scheme is unipolar modulation.

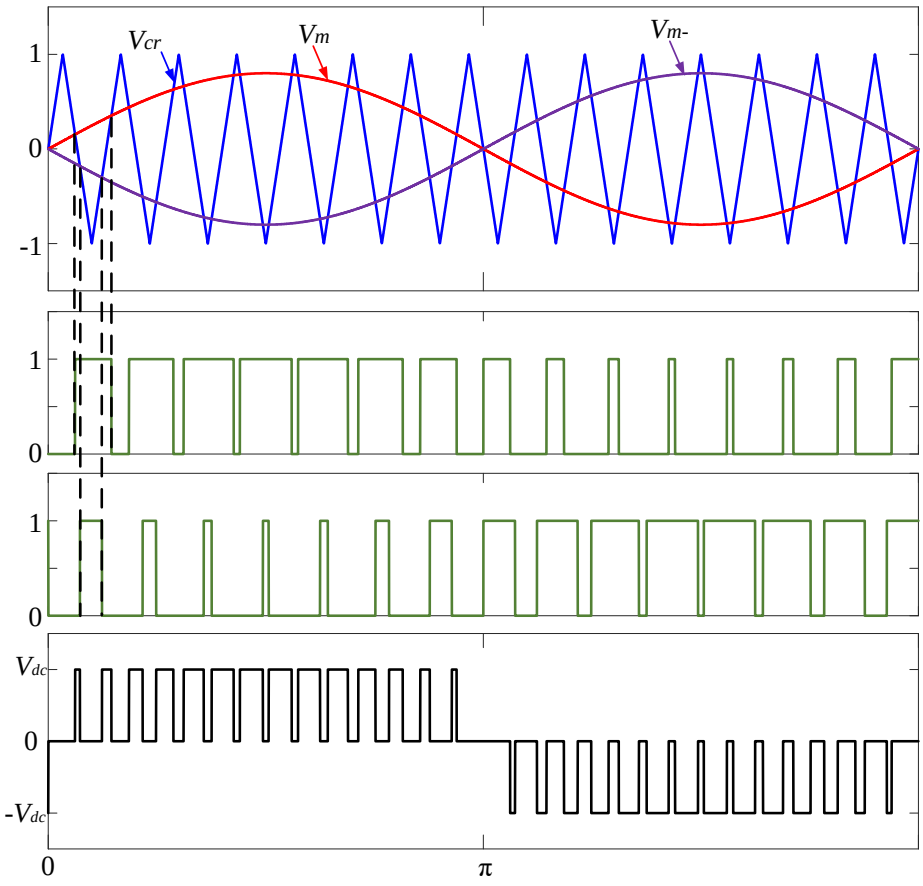

Fig.2.4 A Typical Unipolar Modulation Scheme (m_a=0.8, m_f=15)

Among the two SPWM modulation schemes, unipolar modulation attracts more interests because more harmonics in the output voltage can be eliminated compared with bipolar modulation.

Carrier-shifted modulation schemes are applied to provide switching signals for power cells in CHB inverters. Carrier-based modulation schemes are categorized into phase-shifted and level-shifted modulations [7].

In a CHB inverter, if *N* is the number of power cells in each phase, then the number of phase voltage levels *m* is determined by

$$m = 2N + 1 \tag{2.1}$$

The number of carrier waveforms m_c is expressed by

$$m_c = 2N \tag{2.2}$$

In phase-shifted modulation, all triangular carrier waveforms have the same amplitude and frequency. The phase difference φ_{d} between two adjacent waveforms are determined by

$$\varphi_d = \frac{180^\circ}{N} \tag{2.3}$$

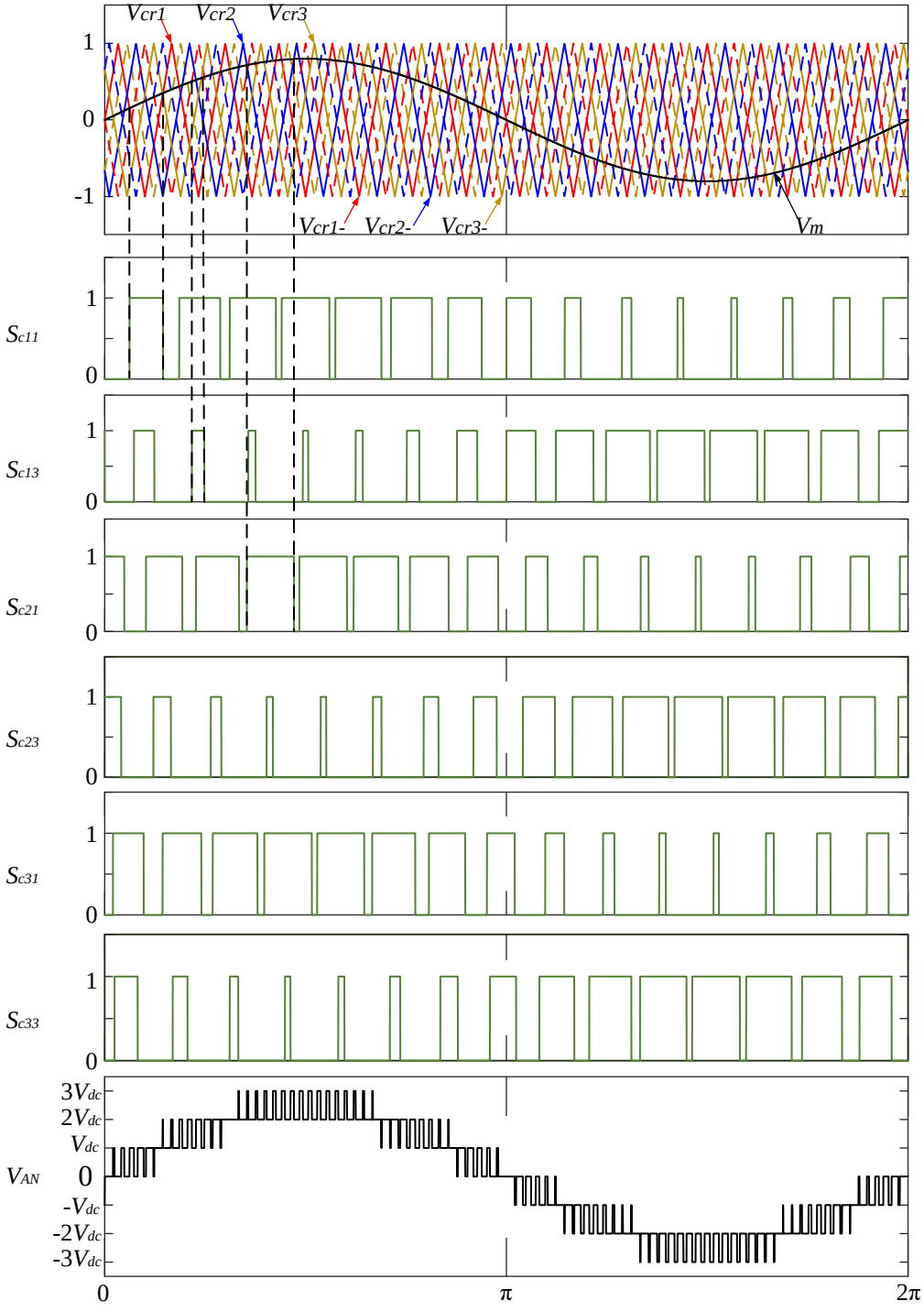

Fig.2.5. Phase-shifted Modulation in a Seven-level CHB Inverter

Fig.2.5 shows the principle of phase-shifted modulation in a seven-level CHB inverter. Like unipolar modulation in single-phase H-bridge inverter, the control signals for three power cells are generated by the comparison between carrier and modulation waveforms. The phase voltage, V_{AN}, is the sum of output voltage in all power cells as:

$$V_{AN} = V_{oH1} + V_{oH2} + V_{oH3} = V_{dc}(S_{c11} + S_{c21} + S_{c31} - S_{c13} - S_{c23} - S_{c33}) \quad (2.4)$$

where V_{oHi} is the i^{th} power cell. S_{cij} is the control signal of power switch S_j in the i^{th} power switch. The phase voltage is formed by seven discrete voltage levels from -3V_{dc} to 3V_{dc}.

With the phase-shifted modulation algorithm, the maximum fundamental line-to-line voltage, $V_{AB1,max}$, is expressed by[7]

$$V_{AB1,max} = 1.224NV_{dc} \quad (2.5)$$

The level-shifted modulation scheme is another unipolar modulation for CHB inverters. In this modulation scheme, the carrier waveforms are vertically distributed and their bands are contiguous. Similar to phase-shifted modulation, the carrier waveforms have the same amplitude and frequency. Also, there are 2N carrier waveforms in the level-shifted modulation scheme. The amplitude modulation index m_a is defined by

$$m_a = \frac{V_m}{2NV_{cr}} \quad (2.6)$$

where V_m is the peak value of modulation waveform and V_{cr} is the amplitude of carrier waveforms.

There are three common level-shifted modulation algorithms [38]: (1) in-phase disposition (IPD), (2) alternate phase opposite disposition(APOD), and (3) phase opposite disposition(POD). Fig.2.6 shows the carrier modulation schemes. In the level-shifted modulation, the modulation waveform should be compared with carrier waveforms to generate the switching signals.

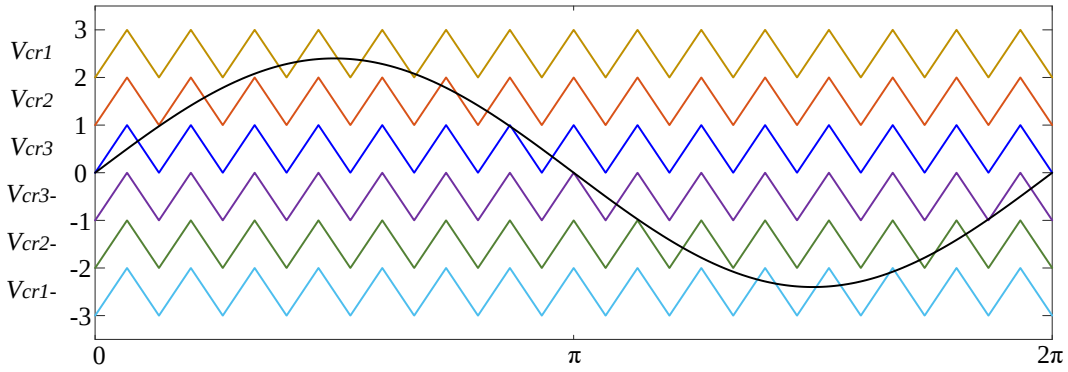

(a) In-phase Disposition(IPD)

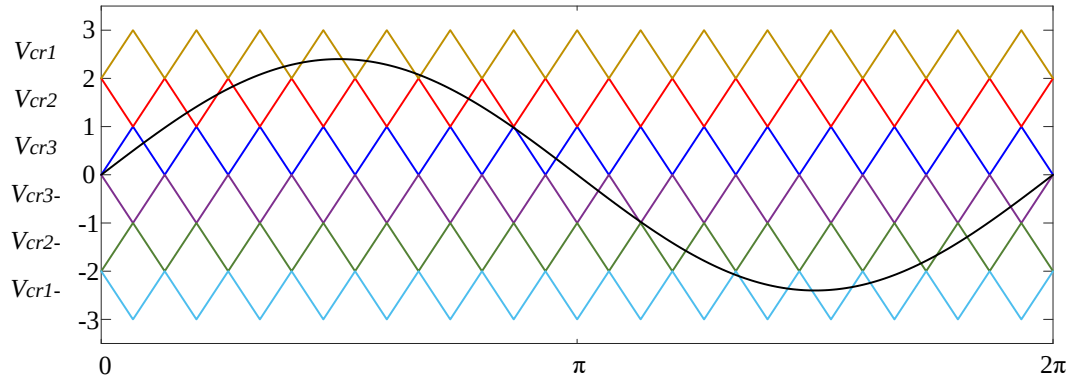

(b) Alternate Phase Opposite Disposition(APOD)

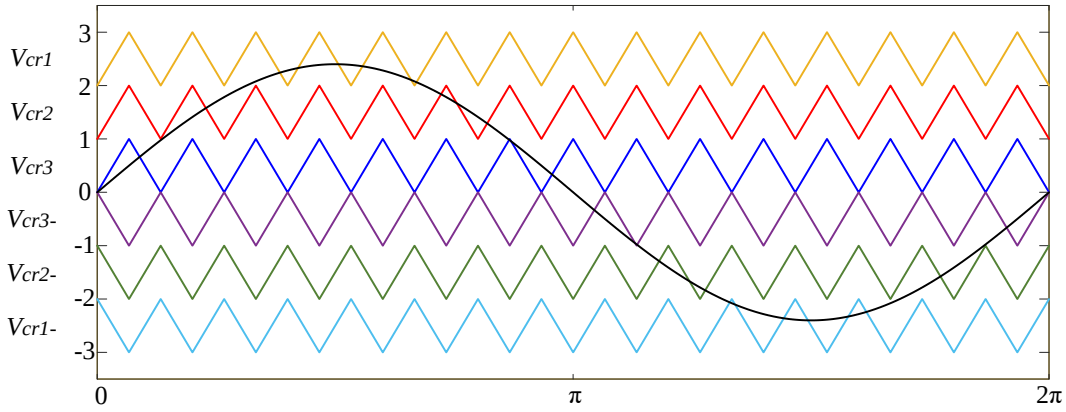

(c) Phase Opposite Disposition(POD)

Fig.2.6. Level-shifted Modulation for a Seven-level CHB Inverter (m_f=15, m_a=0.8)

Phase-shifted modulation has a higher THD value compared with the level-shifted modulation [39]. Among all PWM schemes, SPWM has the simplest structure and can be implemented in multilevel converters easily.

Space vector modulation (SVM) scheme requires the selection of switching states and dwell time calculation of switching states with voltage-second theorem in α-β coordinates in each sampling time. It has better utilization of DC input voltages in CHB inverter compared with SPWM algorithm [40]. However, if the number of voltage levels increases, the computation burden will increase and the algorithm will become more complex with SVM algorithm [41].

The SHE-PWM modulation reduces the low order harmonics in the output currents by modifying the firing angles to provide highest quality output compared with other PWM schemes [42]-[43]. However, the control algorithm is more complicated than all other algorithms and it increases the computation burdens. Also, another major problem in SHE-PWM is to solve the nonlinear equations [44].

2.3 Summary

This chapter introduces the structure and modulation schemes of the CHB topology. A number of power cells are connected to generate multiple voltage levels. The number of power cells are determined by manufacturing cost, THD requirement, and input voltage[7].

DC input voltage is produced by CHB diode rectifiers fed by phase-shifting transformer and carrier-based SPWM modulation scheme is used for CHB inverter. Phase- and level-shifted modulation schemes are introduced in this section. Another two control algorithms are space vector modulation and selective harmonic elimination pulse-width algorithms.

The structure of CHB topologies have the advantage in modular and scalable structure, convenience for fault-tolerant control, lower *dv/dt* and THD values. However, it requires many power switches and isolated DC input voltages.

Chapter 3

Model Predictive Control (MPC) of CHB Inverters

3.1 Introduction

In Chapter 2, the modulation schemes have been introduced for CHB inverters. In this chapter, finite control set model predictive control (FCS-MPC) will be reviewed. In this control algorithm, the load current with various switching signals in the next sampling time can be predicted with the discrete-time mathematical model of the system. In this process, the output current in the time interval k should be measured. The predicted value in the sampling time k+1 should be compared with the reference value and the optimal switching signal is selected by minimization of a cost function. MPC shows a good dynamic performance considering multiple control objectives. The block diagram of the MPC algorithm is shown in Fig.3.1.

In section 3.2, the mathematical model of load current with RL load permanent magnet synchronous motor (PMSM) is reviewed. Section 3.3 illustrates the method to obtain the control signals with a cost function.

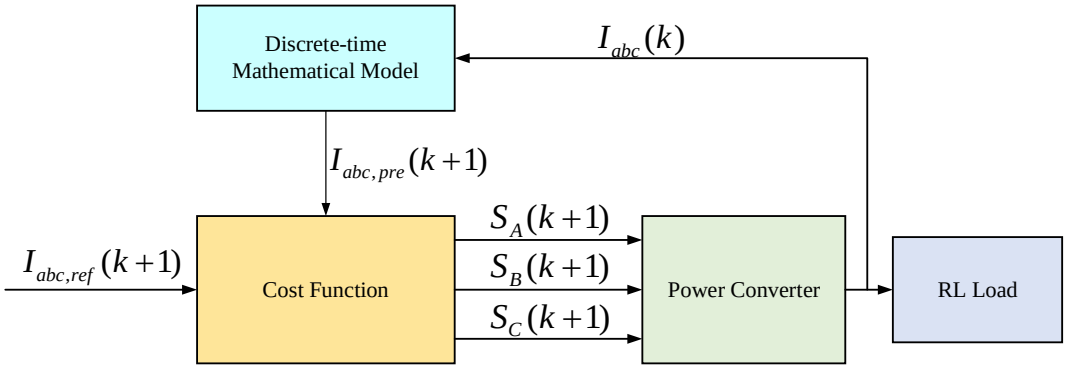

Fig.3.1. General MPC Algorithm with RL Load

3.2 Mathematical Model of the System

A. With RL Load

In this section, the continuous-time mathematical model with RL load is defined. The RL load of three-phase motor drive is as Fig.3.2. Kirchhoff's voltage law is applied to the converter circuit as the following equation.

$$V_{xn} = R_o i_x + L_o \frac{di_x}{dt} \tag{3.1}$$

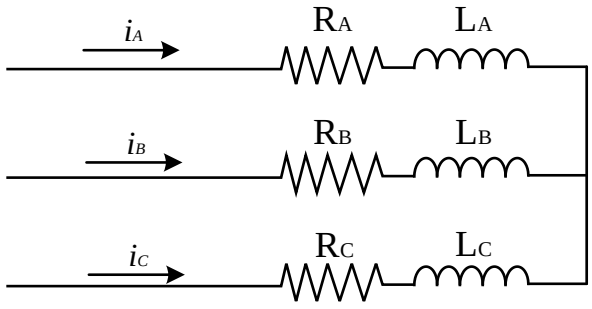

Fig.3.2. RL Model for CHB Motor Drive

where V_{xn}, x=a, b, and c, is the load voltage. i_x is the output current in each phase. R_o and L_o are load resistance and inductance respectively, with the assumption that values in three phases are the same. In this part, load voltages are determined by phase voltages V_{xN} and common mode voltage V_{Nn}. Assuming the three phase load currents are subject to i_a+i_b+i_c=0, the common mode voltage is expressed by (3.2). With the phase voltage and common mode voltage, the load voltage can be obtained with (3.3).

$$V_{Nn} = -\frac{1}{3}(V_{AN} + V_{BN} + V_{CN}) \tag{3.2}$$

$$V_{xn} = V_{xN} + V_{Nn} \tag{3.3}$$

From the two equations, the relationship between phase voltage and load voltage is written in (3.4) [45]:

$$\begin{bmatrix} V_{An} \\ V_{Bn} \\ V_{Cn} \end{bmatrix} = \frac{1}{3}\begin{bmatrix} 2 & -1 & -1 \\ -1 & 2 & -1 \\ -1 & -1 & 2 \end{bmatrix}\begin{bmatrix} V_{AN} \\ V_{BN} \\ V_{CN} \end{bmatrix} \tag{3.4}$$

With equation (2.4), phase voltages can be determined with switching signals. The discrete-time model can be built based on the continuous-time model. The first-order derivative can be calculated with backward Euler method [46] as follows:

$$\frac{di_x}{dt} = \frac{i_x(k+1) - i_x(k)}{T_s} \tag{3.5}$$

where T_s is the sampling time.

By applying equation (3.5) to (3.1), the discrete-time mathematical model of RL load is expressed by (3.6):

$$i_x(k+1) = \frac{T_s}{L_o + R_o T_s} V_{xn}(k+1) + \frac{L_o}{L_o + R_o T_s} i_x(k)$$

$$x=A, B, \text{ and } C \tag{3.6}$$

Therefore, the load current in the time instant k+1 can be predicted with phase voltages and current value in the sampling time k as (3.7):

$$\begin{bmatrix} i_a(k+1) \\ i_b(k+1) \\ i_c(k+1) \end{bmatrix} = \frac{T_s}{3(R_o T_s + L_o)} \begin{bmatrix} 2 & -1 & -1 \\ -1 & 2 & -1 \\ -1 & -1 & 2 \end{bmatrix} \begin{bmatrix} V_{AN}(k+1) \\ V_{BN}(k+1) \\ V_{CN}(k+1) \end{bmatrix} + \frac{L_o}{R_o T_s + L_o} \begin{bmatrix} i_a(k) \\ i_b(k) \\ i_c(k) \end{bmatrix} \tag{3.7}$$

B. With PMSM Load

Similar to RL model, a continuous-time model for PMSM can be developed. The control scheme for PMSM uses the *d-q* rotating frame to control the output currents. With *d-q* reference frame, the three-phase AC voltages and currents are converted to two DC variables in the direct and quadrature axes. Therefore, it simplifies the analysis of the control schemes for PMSM. The block diagram of FCS-MPC algorithm for PMSM is shown in Fig.3.3. In my simulation results, the PMSM has the non-salient rotor, which means L_d=L_q.

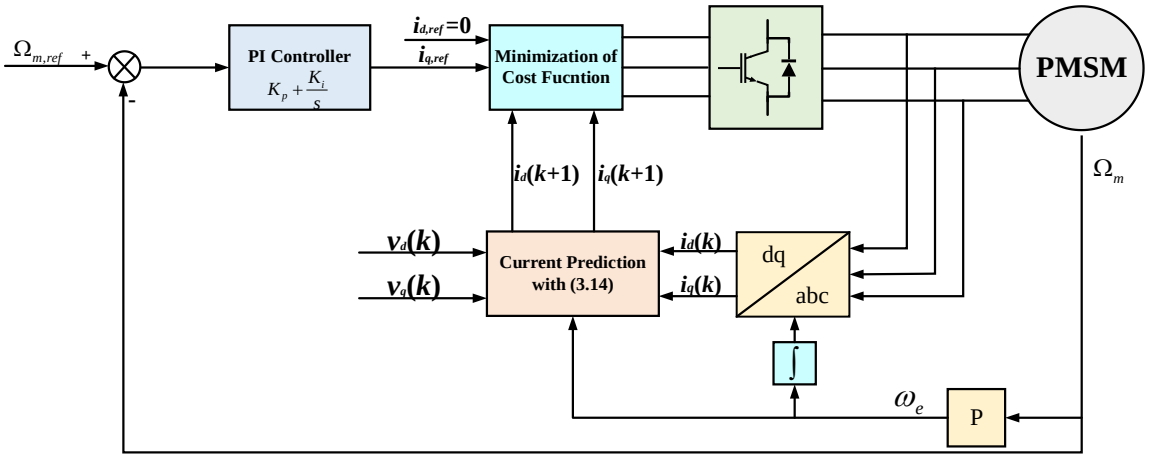

Fig.3.3. MPC Algorithm with PMSM Load

The conversion of three-phase variables to two variables in *d-q* coordinate includes two parts. The first step is to convert the three-phase variables to two variables in *α-β* coordinate by Clark transformation. The Clark transformation matrix is as (3.8):

$$\begin{bmatrix} x_\alpha \\ x_\beta \end{bmatrix} = \frac{2}{3} \begin{bmatrix} 1 & -\frac{1}{2} & -\frac{1}{2} \\ 0 & \frac{\sqrt{3}}{2} & -\frac{\sqrt{3}}{2} \end{bmatrix} \begin{bmatrix} x_A \\ x_B \\ x_C \end{bmatrix} \tag{3.8}$$

The voltages vectors in the first sector in *α-β* plane are as Fig.3.4. For a multilevel CHB converter, the number of voltage vectors is expressed by $12N^2+6N+1$(*N* is the number of power cells in each phase). In the seven-level CHB inverter, the number of voltage vectors in FCS-MPC is 127.

Then, the electrical position *θ* is applied to turn the two variables in *α-β* coordinate to those in *d-q* coordinate by Park transformation. The Park transformation is as (3.9):

$$\begin{bmatrix} x_d \\ x_q \end{bmatrix} = \begin{bmatrix} \cos\theta & \sin\theta \\ -\sin\theta & \cos\theta \end{bmatrix} \begin{bmatrix} x_\alpha \\ x_\beta \end{bmatrix} \tag{3.9}$$

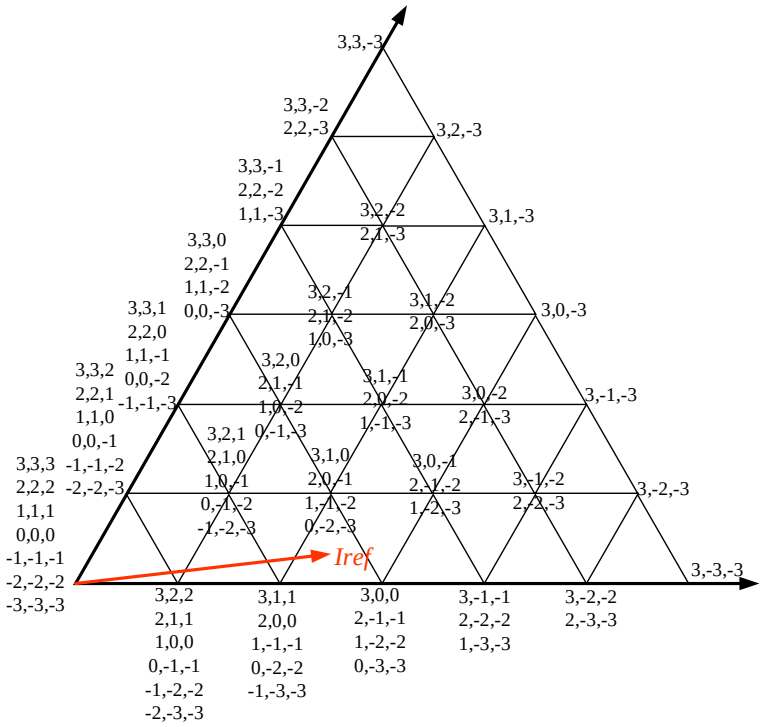

Fig.3.4. Space Vectors for a Seven-level CHB Topology (Sector I)

The continuous-time mathematical model in *d-q* coordinate is given as (3.10) and the electromagnetic torque T_e is as (3.11) [47]:

$$\begin{cases} v_d = R_s i_d + \frac{d\Psi_d}{dt} - \omega\Psi_q \\ v_q = R_s i_q + \frac{d\Psi_q}{dt} + \omega\Psi_d \end{cases} \tag{3.10}$$

$$T_e = \frac{3}{2} P\left(\Psi_d \cdot i_q - \Psi_q \cdot i_d\right) \tag{3.11}$$

where P is the number of pole pairs. i_d and i_q are stator currents in d-q coordinate. v_d and v_q are stator voltages in d-q coordinate. ω is the electrical speed. Ψ_d and Ψ_q are motor linkage fluxes in d-q coordinate. Electrical speed and motor linkage fluxes are as follows:

$$\omega = P\Omega \tag{3.12}$$

$$\begin{cases} \Psi_d = L_d i_d + \Psi_f \\ \Psi_q = L_q i_q \end{cases} \tag{3.13}$$

where Ω is mechanical speed. L_d and L_q are stator inductances in d and q axes. Ψ_f is the permanent magnet linkage flux.

With equation(3.10), the discrete-time model can be rewritten as (3.14)[48]:

$$\begin{cases} i_d(k+1) = (1 - \frac{R_o T_s}{L_o}) i_d(k) + \frac{T_s}{L_o} v_d(k) + T_s \omega i_q(k) \\ i_q(k+1) = (1 - \frac{R_o T_s}{L_o}) i_q(k) + \frac{T_s}{L_o} v_q(k) - T_s \omega i_d(k) - \frac{T_s}{L_o} \omega \Psi_f \end{cases} \tag{3.14}$$

In this process, the stator currents in the sampling time k+1 can be predicted with the stator voltages and stator currents measured in the time instant k.

From the theory, the electromagnetic torque in (3.11) can be transferred to (3.15). The mechanical speed is obtained from (3.16). In addition, the motor speed is subject to the mathematical model of mechanical dynamics as (3.17).

$$T_e = \frac{3}{2} P \left[\Psi_f + \left(L_d - L_q \right) \cdot i_d \right] \cdot i_q \tag{3.15}$$

$$\Omega = \frac{2\pi f_o}{P} \tag{3.16}$$

$$J\frac{d\Omega}{dt} = T_e - T_l - f\Omega \quad (3.17)$$

Where J is the rotor inertia. T_l is the load torque for PMSM. f_o is the frequency of output currents. f is the friction coefficient to calculate the friction torque.

With (3.6) and (3.14), the discrete-time mathematical models of RL and PMSM loads are provided. The load currents in the next time interval can be predicted. Then, in the next section, the cost function should be defined to compare the error between the reference and actual values. With the minimization of the cost function, the optimal switching signals are found.

3.3 Cost Function Evaluation

With the prediction of output currents, the method to find the optimal control signals is to compare all predicted values with the reference values. For the RL load, the three-phase reference current are sinusoidal waveforms. The reference sinusoidal signals are expressed as (3.18) by Langrage extrapolation [46]:

$$i_{ref}(k+1) = 4i_{ref}(k) - 6i_{ref}(k-1) + 4i_{ref}(k-2) - i_{ref}(k-3) \quad (3.18)$$

In the PMSM model, the reference current in d axis, $i_{d,ref}$, is set to 0 to obtain the maximum torque. From (4.15) and (4.17), the rotor speed relates to quadrature current i_q with i_d=0. To control the motor speed, a PI controller is used to provide the quadrature

reference current, $i_{q,ref}$ with the error between reference and measured rotor speeds. The PI control scheme is as (4.19).

$$i_{q,ref} = K_p\left(\Omega_{m,ref} - \Omega_m\right) + K_i \int \left(\Omega_{m,ref} - \Omega_m\right) dt \tag{3.19}$$

With the PI control in the PMSM, the motor speed can be controlled to the desired value.

With the reference values, the cost function of the error between predicted and actual values can be applied to find the optimal switching signals which make the predicted currents closest to the reference values. The cost function in RL and PMSM loads are as following equations:

$$J(k+1) = ||i_{abc}(k+1) - i_{abc,ref}(k+1)||_2 \tag{3.20}$$

$$J(k+1) = ||i_{dq}(k+1) - i_{dq,ref}(k+1)||_2 \tag{3.21}$$

where $i_{abc} = [i_a \quad i_b \quad i_c]^T$ and $i_{dq} = [i_d \quad i_q]^T$.

With the two given cost functions, the optimal voltage vectors can be selected by minimizing the error between predicted and actual value.

3.4 Simulation Studies of Conventional MPC

In this section, the simulation results of a conventional MPC algorithm with RL and PMSM loads are provided. The simulation is based on MATLAB/Simulink Model. The parameters of the RL and PMSM load are as provided in Section.3.4.1 and 3.4.2.

3.4.1 Simulation Results of Conventional MPC Algorithm with RL Load

For the simulation study with an RL load, the parameters of the model are given as Table. 3.1. The load side of the CHB is connected to RL load. With conventional FCS-MPC algorithm, three-phase currents can be controlled to desired values.

TABLE 3.1 PARAMETERS IN THE SEVEN-LEVEL CHB INVERTER WITH RL LOAD

Parameters	Values
DC input Voltage V_{dc}	70V
DC Capacitance in Each Cell	2.3mF
Load Inductance L_o	5mH
Load Resistance R_o	13Ω
Operation Frequency	60Hz
Switching Frequency	900Hz
Reference Load Current	6-9Arms
Sampling Time T_s	100μs

To test the MPC algorithm, the simulations of steady-state and dynamic performances are provided. In the steady-state performance, the RMS value of load currents is set to 9A.

The waveforms of load currents and phase voltage is as Fig.3.5. In this situation, the THD value of load currents is 1.81%.

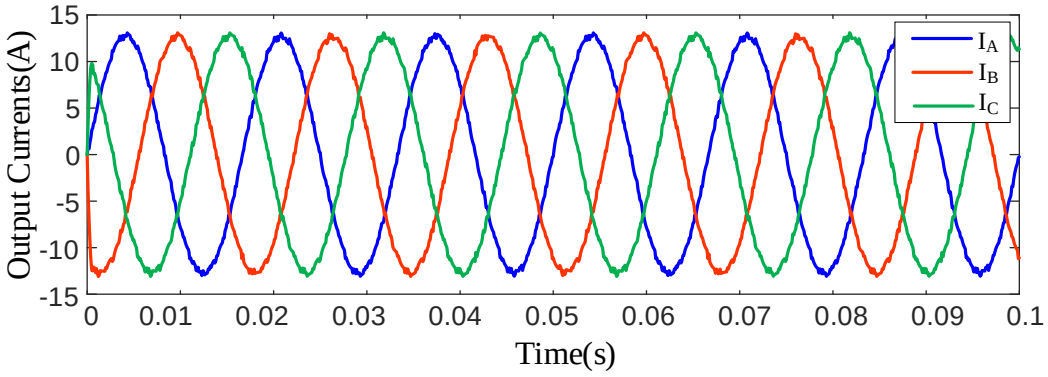

(a) Output Currents

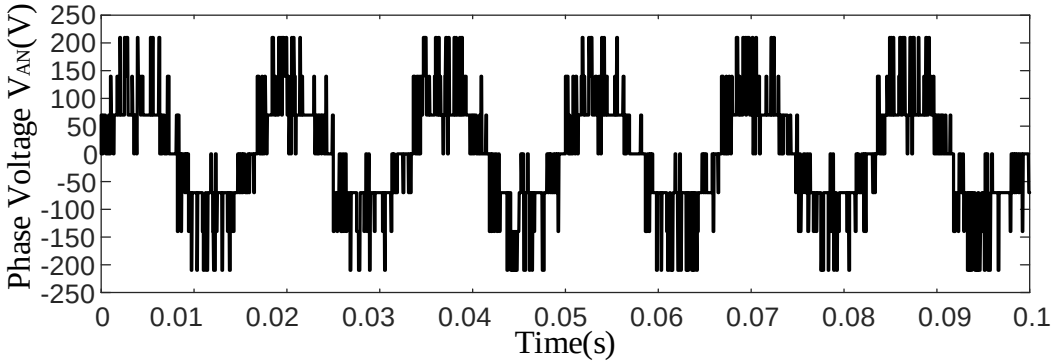

(b) Phase Voltage V_{AN}

Fig.3.5. Steady-state Simulation Results with FCS-MPC Scheme and RL Load

Also, the simulation results of dynamic performance are provided in Fig3.6. Fig.3.6 shows the simulation results of amplitude change which the load currents increase from

6Arms to 9Arms at *t*=0.05s. Fig.3.7 shows the performance of frequency change with FCS-MPC algorithm. The frequency decreases from 60Hz to 10Hz at *t*=0.05s.

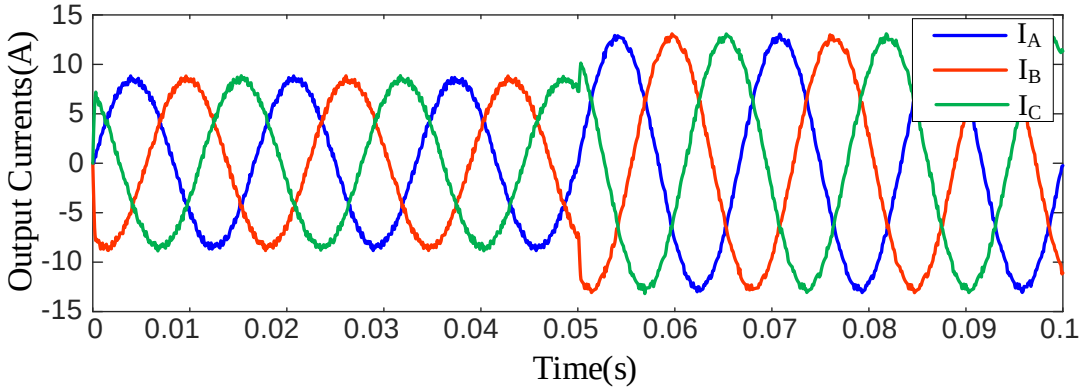

(a) Output Currents

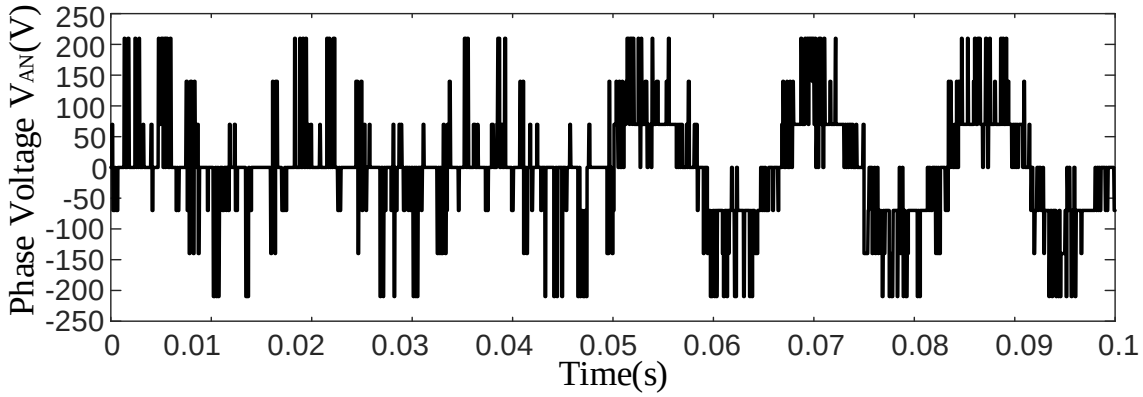

(b) Phase Voltage V_{AN}

Fig.3.6. Simulation Results with FCS-MPC Scheme under Amplitude Change

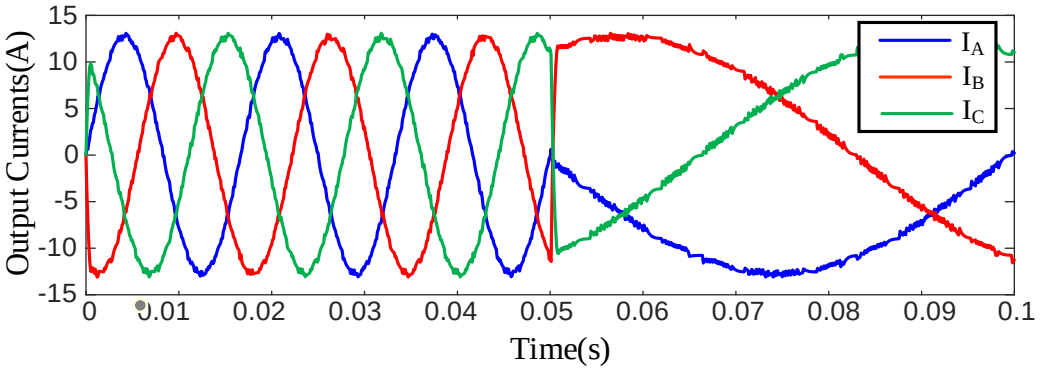

(a) Output Currents

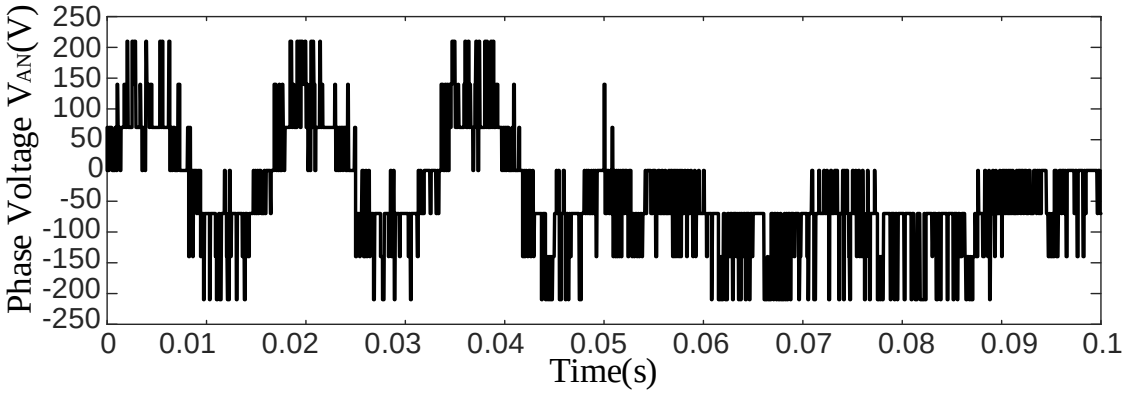

(b) Phase Voltage V_{AN}

Fig.3.7. Simulation Results with FCS-MPC Scheme under Frequency Change

3.4.2 Simulation Studies of Conventional MPC Algorithm with PMSM Load

The parameters of PMSM control are shown in Table.3.2. With the PMSM load, FCS-MPC algorithm realizes the control of motor speed under different load torques.

TABLE 3.2 PARAMETERS IN THE SEVEN-LEVEL CHB MOTOR DRIVE WITH PMSM

Parameters	Values
DC input Voltage V_{dc}	1000V
DC Capacitance in Each Cell	2.3mF
Stator Inductance L_s	177.3mH
Stator Resistance R_s	0.0726Ω
Flux Linkage Ψ_f	7.7Wb
Number of Pole Pairs p	3
Rated Motor Speed Ω_m	1200rpm
Rotor Inertia J	0.9783kg·m^2
Rated Torque T	5570N·m
Sampling Time T_s	100μs

Like the simulation results with RL load, the simulation results of FCS-MPC with PMSM load also include steady-state and dynamic performances.

In the steady-state performance, the motor speed is set to be 800rpm and the load torque is 1500N·m. The THD value of load currents is 2.56%. From the simulation results, the motor speed is controlled successfully.

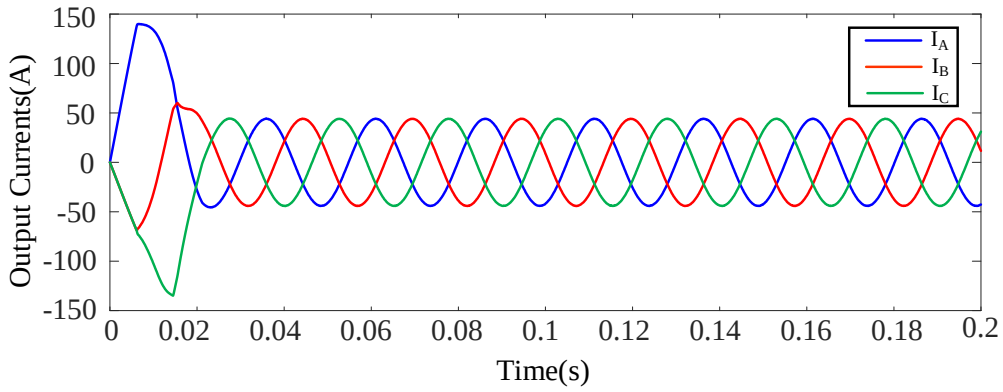

(a) Three-phase Motor Currents

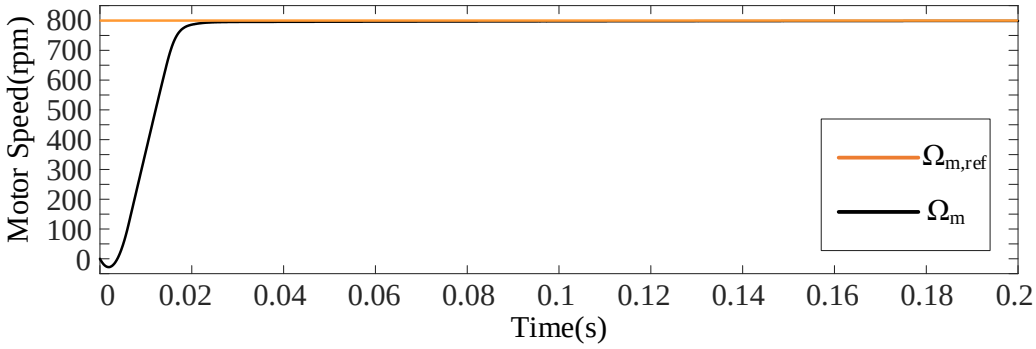

(b) Motor Speed Ω_m

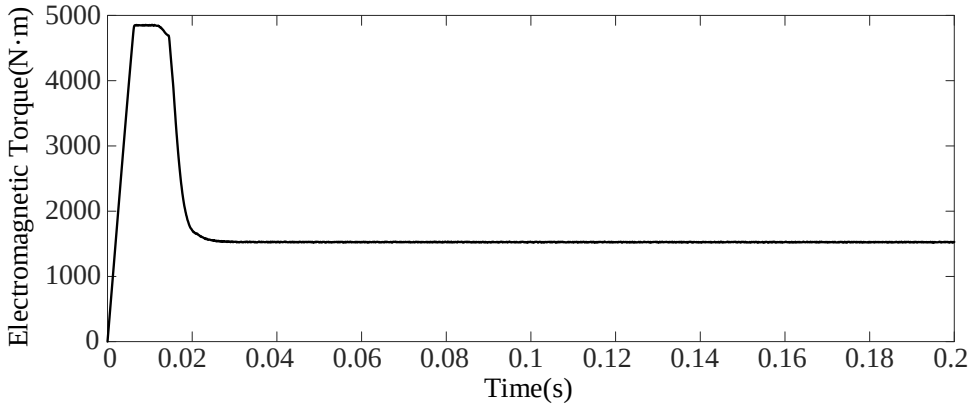

(c) Electromagnetic Torque T_e

Fig.3.8. Steady-state Simulation Results with FCS-MPC Algorithm and PMSM Load

To test the dynamic performance of FCS-MPC with PMSM load, the modification of motor speed and load torque should be simulated. Fig.3.9 shows the simulation results with motor speed increasing from 600 to 750Hz at t=0.1s. In this case, the operation frequency increases from 30 to 37.5Hz. Fig.3.10 shows the simulation results with load torque increasing from 1000 to 1500 N·m at t=0.1s. From the simulation results, the conventional MPC algorithm has a good dynamic performance with speed and load torque changes as that with RL load.

From the simulation results, conventional FCS-MPC performs well in the control of the CHB motor drive with RL and PMSM load. The speed of PMSM can be controlled with the modification of the desired speed and the load torque.

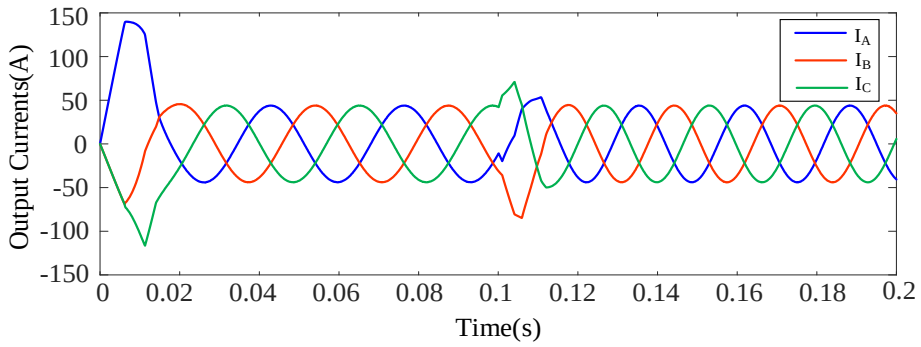

(a) Three-phase Motor Currents

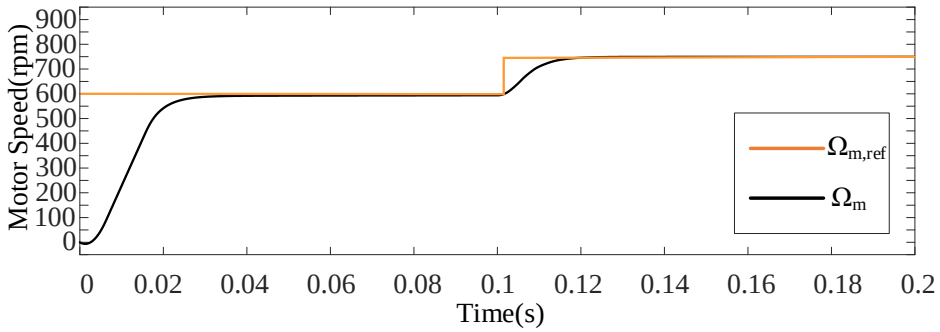

(b) Motor Speed Ω_m

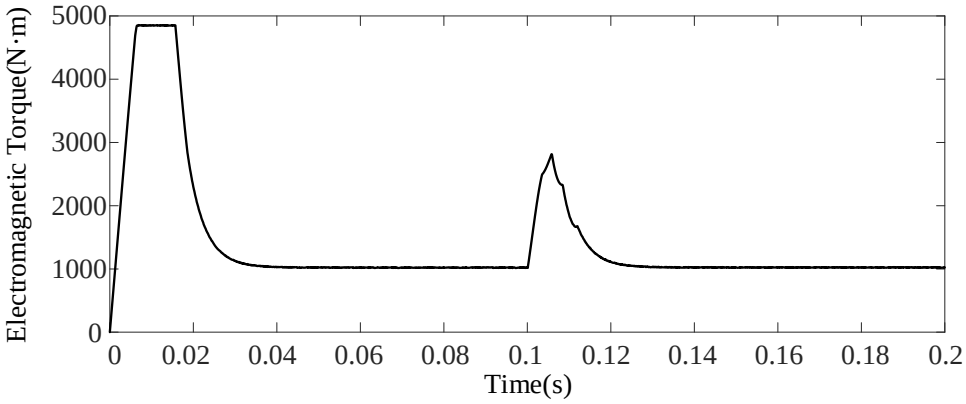

(c) Electromagnetic Torque T_e

Fig.3.9. Simulation Results under Speed Change with M^{2}PC Algorithm with PMSM

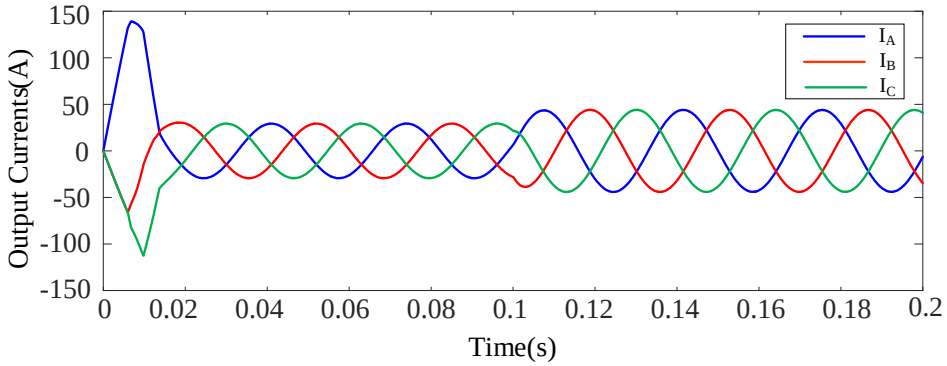

(a) Three-phase Motor Currents

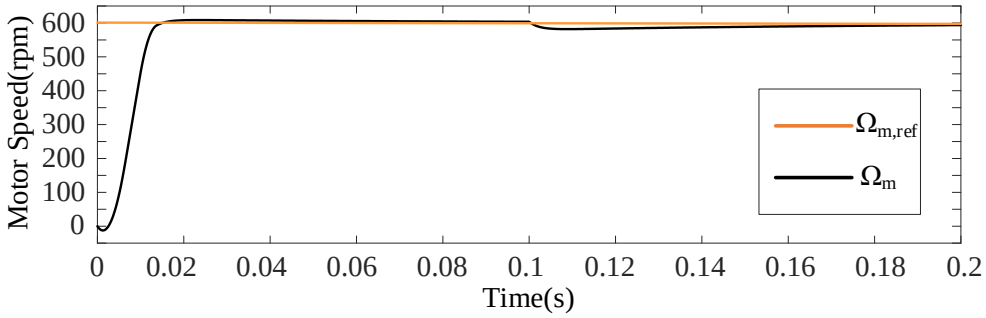

(b) Motor Speed Ω_m

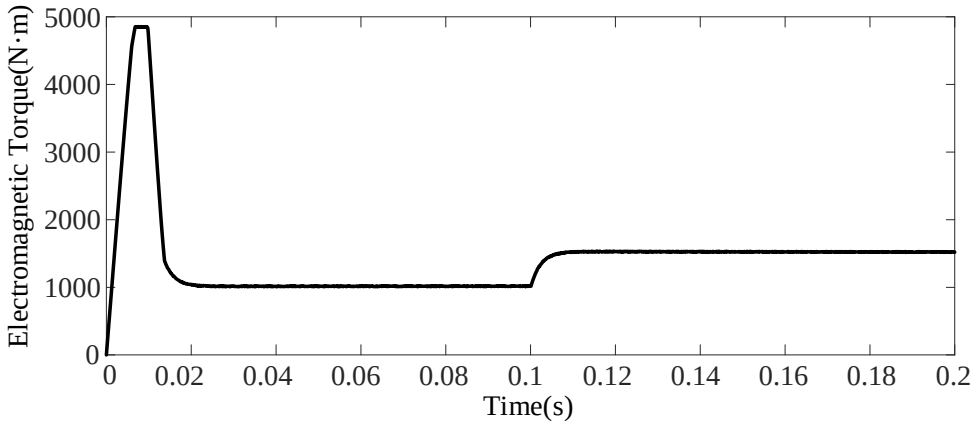

(c) Electromagnetic Torque T_e

Fig.3.10. Simulation Results under Load Torque Change with MPC Algorithm with PMSM

3.5 Summary

With the FCS-MPC algorithm, the optimal switching signals can be found by the minimization of cost function. It has a simple structure with good dynamic performance and multiple control objectives. However, one drawback is that the switching frequency is variable with the dynamic performance. Compared with a variable switching frequency MPC method, a fixed switching frequency method can improve the harmonic spectrum and be suitable for the filter design. Therefore, the MPC algorithm with fixed switching frequency is under study. Also, for the CHB inverter, the number of voltage vectors is large and it is a large computation burden for DSP.

In Chapter 4, a control algorithm called modulated model predictive control (M^2PC), is introduced. With the M^2PC algorithm, it obtains the low fixed switching frequency in the control with the advantages of conventional FCS-MPC. In addition, the number of voltage vectors to analyze is smaller than that in the conventional FCS-MPC. In this control scheme, the output currents are transformed to α-β reference frame, and the optimal voltage vector is selected.

Chapter 4

Modulated Model Predictive Control (M^2PC) for CHB Inverters

4.1 Introduction

In this chapter, principles of M^2PC algorithm are analyzed. For this algorithm, the three-phase voltages and currents are transformed to α-β coordinate with Clark transformation. The voltage vector set is defined in the domain of voltage vector in the sampling time. The current vector can be predicted with measured current and control signals. Then, the cost function is built to find the optimal voltage vector by minimizing the error between reference and actual currents. Finally, a modulation scheme is applied to generate the control signals. The M^2PC algorithm has been applied in the CHB static synchronous compensator (STATCOM) in [49]. In the thesis, the M^2PC algorithm has been applied in the CHB motor drive.

[22] introduces a modulated model predictive control for a three-level NPC inverter. In the M^2PC algorithm, space vector modulation is applied to provide the control signals for power switches. In this algorithm, the duty cycles of two voltage vectors and zero voltage vector are obtained by the cost functions of all voltage vectors. Also, [23] applied the M^2PC algorithm in the matrix converter. In these two papers, the switching frequency is fixed. However, the M^2PC algorithm applied in the thesis is based on the definition of

voltage vectors in α-β coordinate with the search step determined by the difference between reference and measured current vectors. The search step is adaptive for a suitable domain and modifies the value by the current difference. Under this circumstance, the evaluated control set can be selected and defined.

In this chapter, the simulation and experiments are based on RL and PMSM loads. The block diagram of the M^{2}PC algorithm with RL and PMSM loads are shown in Fig.4.1. With the application of the proposed M^{2}PC, the switching frequency is fixed and the computation burden can be reduced [50].

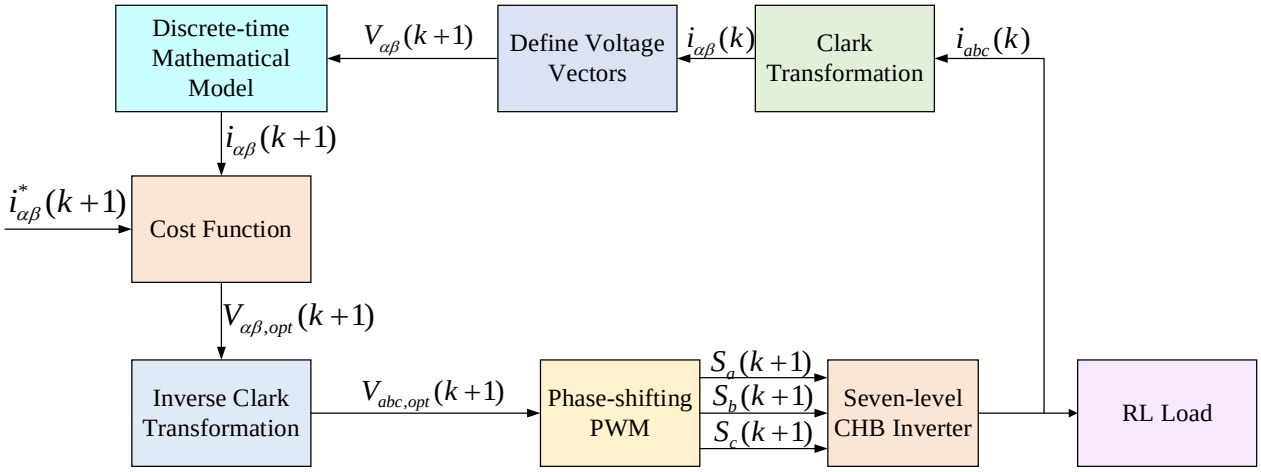

(a) RL Load

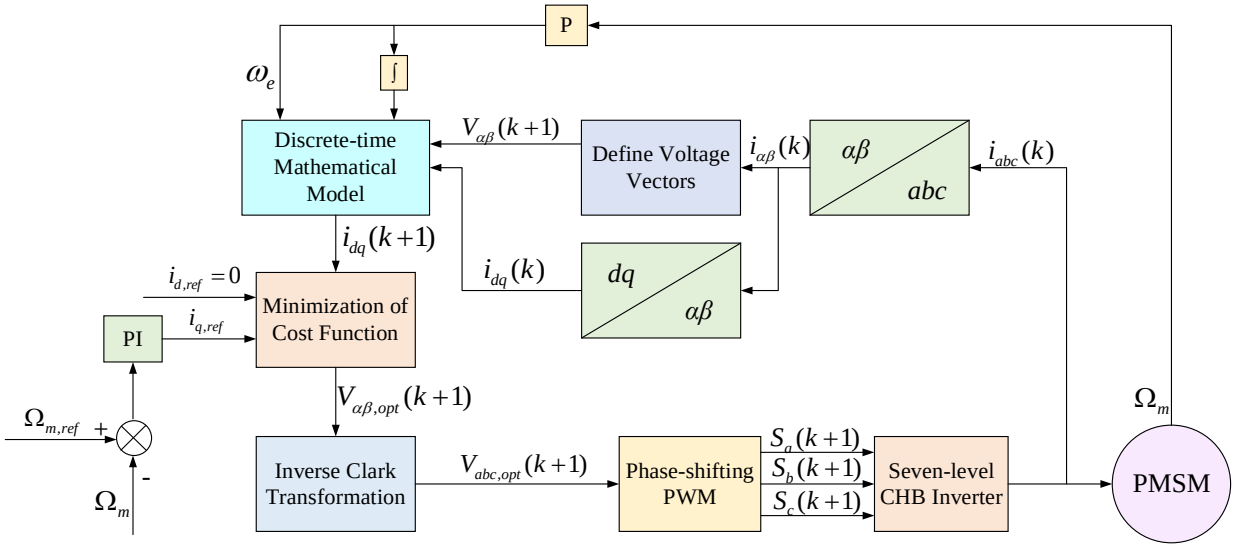

(b) PMSM Load

Fig.4.1. Block Diagram of Modulated Model Predictive Control

4.2 Principle of Modulated Model Predictive Control (M^{2}PC)

4.2.1 Output Current Prediction

As discussed above, the output currents can be predicted with equation (3.6). The system model of RL load can be transferred to α-β coordinate as (4.1).

$$\begin{bmatrix} i_\alpha(k+1) \\ i_\beta(k+1) \end{bmatrix} = \frac{T_s}{L_o+R_oT_s}\begin{bmatrix} V_\alpha(k+1) \\ V_\beta(k+1) \end{bmatrix} + \frac{L_o}{L_o+R_oT_s}\begin{bmatrix} i_\alpha(k) \\ i_\beta(k) \end{bmatrix} \quad (4.1)$$

where i_α and i_β are output currents in α and β axes. V_α and V_β are load voltages in α and β axes. The PMSM model is still as (3.14).

With equation (4.1), the predicted output currents, $i_\alpha(k+1)$ and $i_\beta(k+1)$, can be calculated with measured currents in the time instant k, voltage vector in the time instant $k+1$, sampling time T_s, and load resistance R_o and inductance L_o.

4.2.2 Definition of Voltage Vector Set

In equation (4.1), the output currents can be measured with the current sensor. However, the predicted load voltages, $V_\alpha(k+1)$ and $V_\beta(k+1)$, are important components in the model. Therefore, the voltage vector set needs to be determined. It is assumed that they are in the domain of load voltages in the time interval k. To make the set of voltage vectors simple, a rectangular domain is defined as Fig.4.2 [49]. In this voltage vector set, there are nine possible voltage vectors in α-β coordinate. The voltage vector set is defined as (4.2). The values of m and n are to define the search range.

$$\begin{bmatrix} V_\alpha(k+1) \\ V_\beta(k+1) \end{bmatrix} = \begin{bmatrix} V_\alpha(k) \\ V_\beta(k) \end{bmatrix} + \begin{bmatrix} m\Delta V_\alpha(k) \\ n\Delta V_\beta(k) \end{bmatrix} \tag{4.2}$$

$$m, n \in -1, 0, +1$$

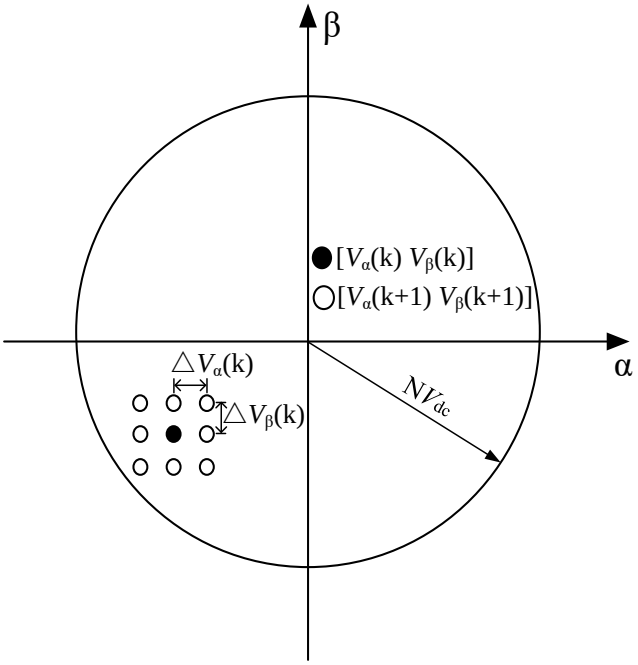

Fig.4.2. Domain of Possible Voltage Vectors

In this equation, adaptive search steps, $\Delta V_\alpha(k)$ and $\Delta V_\beta(k)$, are important factors in the definition of voltage vectors. The adaptive search steps are calculated by the difference between reference and measured current values as shown in (4.3). If the error between reference and actual values is too large, the search step increases to improve the dynamic performance. Also, if the error is small, the search step decreases to reduce the oscillation in the control. Therefore, the adaptive search step is suitable for the M^{2}PC algorithm.

$$\begin{bmatrix} \Delta V_\alpha(k) \\ \Delta V_\beta(k) \end{bmatrix} = \frac{NV_{dc}}{I_{amp}(k)} \begin{bmatrix} |i_\alpha^*(k) - i_\alpha(k)| \\ |i_\beta^*(k) - i_\beta(k)| \end{bmatrix} \tag{4.3}$$

where N is the number of power cells in each phase. I_{amp}(k) is the amplitudes of reference output currents in α and β axes. $i_\alpha^*(k)$ and $i_\beta^*(k)$ are reference output currents in the time instant k. $i_\alpha(k)$ and $i_\beta(k)$ are measured output currents in the time instant k.

Meanwhile, there is a maximum and a minimum in the adaptive search step. Under this circumstance, a saturation function is needed to limit the values of search steps. The function $Sat(\Delta V)$ is defined as (4.4):

$$Sat(\Delta V) = \begin{cases} \Delta V_{\max} & (\Delta V_{\max} > \Delta V) \\ \Delta V & (\Delta V_{\min} \le \Delta V \le \Delta V_{\max}) \\ \Delta V_{\min} & (\Delta V_{\min} < \Delta V) \end{cases} \tag{4.4}$$

where $\Delta V_{\max}$ and $\Delta V_{\min}$ are maximum and minimum of search steps, which are set to $0.2NV_{dc}$ and $0.05\ NV_{dc}$.

In the selection of predicted voltage vectors, they should be in the circle with radius of NV_{dc} as shown in (4.5). Voltage vectors outside this circle are not discussed. The block diagram of voltage vector definition is as given.

$$V_\alpha^2(k+1) + V_\beta^2(k+1) \leq (NV_{dc})^2 \tag{4.5}$$

Therefore, the voltage vector set is defined, and the optimal voltage vector can be obtained with the cost function.

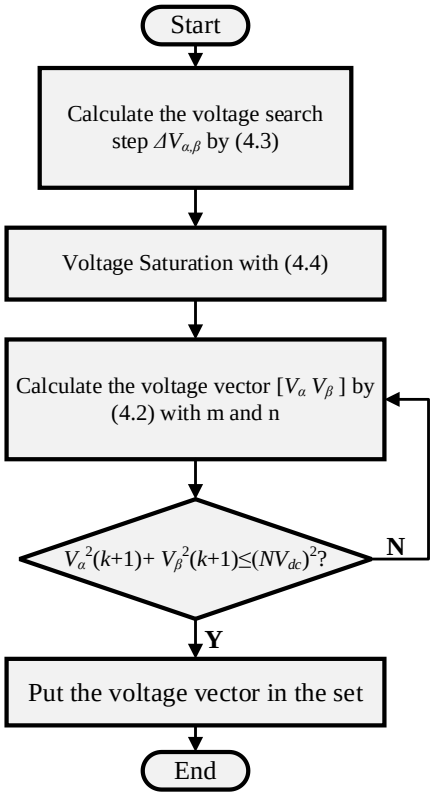

Fig.4.3. Flow Chart of Voltage Vector Definition

In the theory, the voltage vector in α-β coordinate in the time interval k+1 should be in the domain of that in the time interval k. Therefore, the set of voltage vectors are defined in the domain of [$V_\alpha(k)$ $V_\beta(k)$]. Also, the search step is calculated by the difference between measured and predicted values, which can make the load currents reach reference values. In addition, a larger search range can have the fast dynamic response. However, it will increase the computation burden significantly. In my simulation, the nine voltage vectors

have the good performance and there is no need to increase the search range. Therefore, I define the nine voltage vectors and find the optimal voltage vector with the minimization of cost function.

4.2.3 Cost Function Evaluation

With the definition of search step and voltage vector set, the output currents can be predicted with (4.1). Similar to the cost function in Chapter 3, the cost function in α-β coordinate is expressed as (4.6):

$$J(k+1) = ||i_{\alpha\beta}(k+1) - i_{\alpha\beta,ref}(k+1)||_2 \tag{4.6}$$

where $i_{\alpha\beta}$ is the current vector $[i_\alpha \quad i_\beta]^T$ and $i_{\alpha\beta,ref}$ is the reference values.

The flow chart of output current prediction with cost function evaluation is shown in Fig.4.4. In the process, the prediction values with various voltage vectors are calculated and the minimum of the cost function can be found. With the minimum cost function, the corresponding load voltage vector can be obtained.

With the calculation of optimal load voltage vector, the control signals can be provided with PWM scheme. The amplitude of modulation waveforms can be obtained in section.4.2.4.

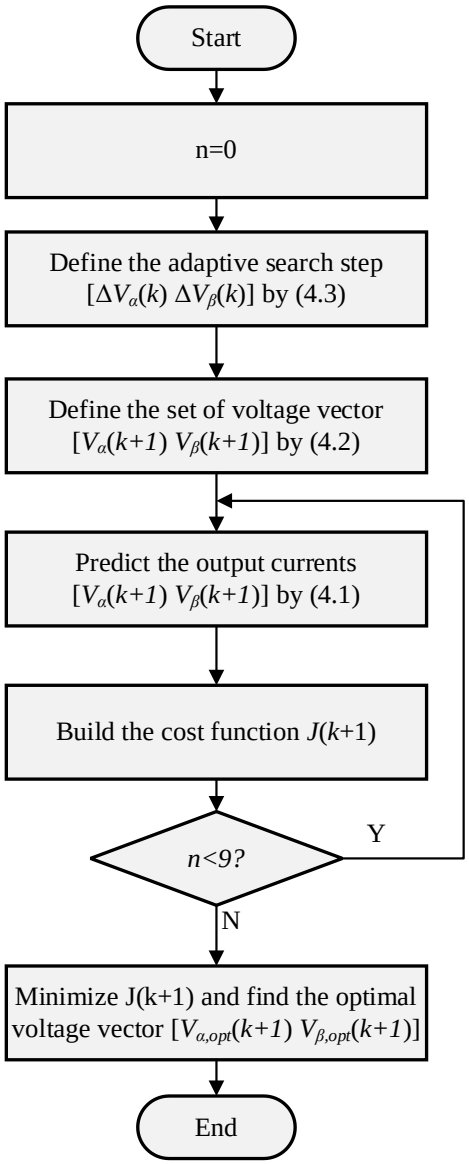

Fig.4.4. Flow Chart of Current Prediction and Cost Function Minimization

4.2.4 Phase-shifted Modulation Scheme

In Section 4.2.3, the optimal voltage vector can be obtained with the minimization of the cost function. Under this circumstance, the modulation scheme can be applied to generate the control signals for power switches. In this condition, carrier phase-shifted

modulation is selected to realize the fixed switching frequency in the system. With the optimal voltage vector $V_{\alpha,opt}(k+1)$ and $V_{\beta,opt}(k+1)$, the three-phase optimal voltages are calculated with inverse Clark transformation as shown in (5.6). Then, the three-phase optimal voltages, $V_{a,opt}$, $V_{b,opt}$, and $V_{c,opt}$, are normalized as (5.7) and compared with carrier waveforms to produce switching signals.

$$\begin{bmatrix} V_{A,opt} \\ V_{B,opt} \\ V_{C,opt} \end{bmatrix} = \begin{bmatrix} 1 & 0 \\ -\frac{1}{2} & \frac{\sqrt{3}}{2} \\ -\frac{1}{2} & -\frac{\sqrt{3}}{2} \end{bmatrix} \begin{bmatrix} V_{\alpha,opt} \\ V_{\beta,opt} \end{bmatrix} \tag{5.6}$$

$$m_x = \frac{V_{x,opt}}{NV_{dc}} \tag{5.7}$$

where m_x (x=A, B, and C) is the modulation reference for each phase. With the phase-shifted modulation as explained in Chapter 2, the control signals can be generated.

With the modulation scheme, the lower fixed switching frequency of the system is obtained. With the lower fixed switching frequency, the harmonic spectrum can be improved and the filter design in the system is more convenient.

4.3 Simulation Studies

The verifications of the proposed developed modulated model predictive control with RL and PMSM loads are conducted in the MATLAB/Simulink model. The DC voltage in the capacitor in each power cell is assumed to be fixed to a constant value.

4.3.1 Simulation Studies with RL Load

For the simulation study with an RL load, the parameters of the model are as Table. 3.1. The load side of the CHB is connected to RL load. With M^{2}PC algorithm, three-phase currents can be controlled to desired values.

The simulation studies include steady-state and dynamic performances. In the steady state of M^{2}PC algorithm, the RMS value of load currents is set to 9Arms. The output currents and phase voltage are as shown in Fig.4.5. The switching frequency is fixed at 900Hz, the sampling time is 0.05s, and the THD value of the load currents is 4.43%.

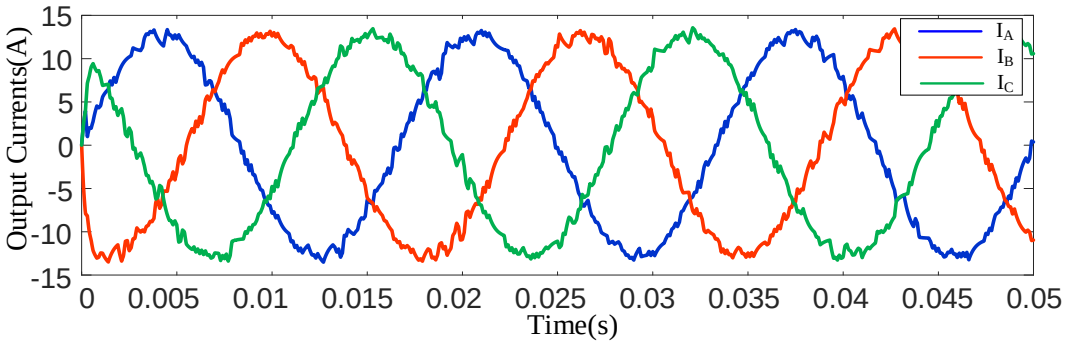

(a) Output Currents

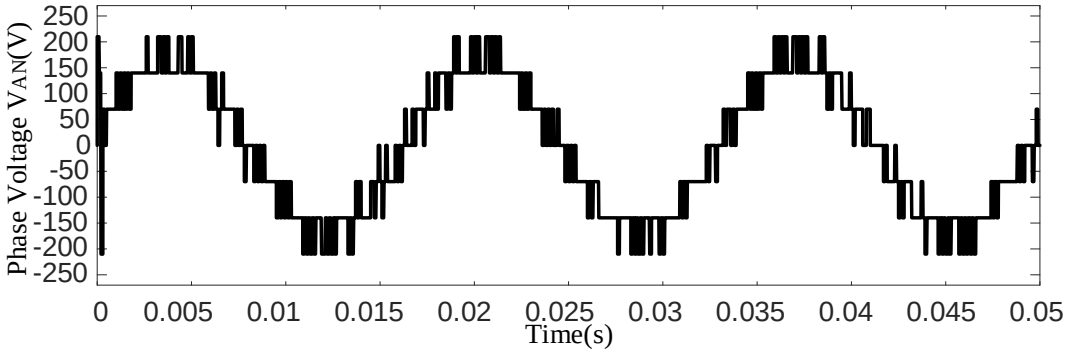

(b) Phase Voltage V_{AN}

Fig.4.5. Steady-state Simulation Results with M^{2}PC Scheme and RL Load

To verify the dynamic performance of the M^{2}PC algorithm, the simulation results of amplitude and frequency changes are provided as shown in Fig.4.6 and Fig.4.7. In the

amplitude change, the RMS value of load currents increases from 6Arms to 9Arms at *t*=0.05s. In the frequency change, the operation frequency decreases from 60Hz to 10Hz at *t*=0.05s. From the simulation results, the provided M^{2}PC algorithm has a fast response.

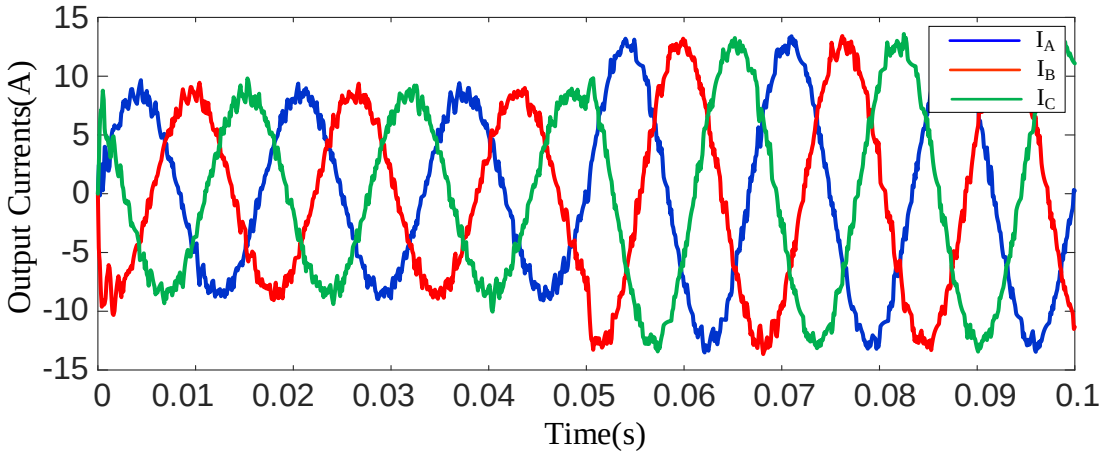

(a) Output Currents

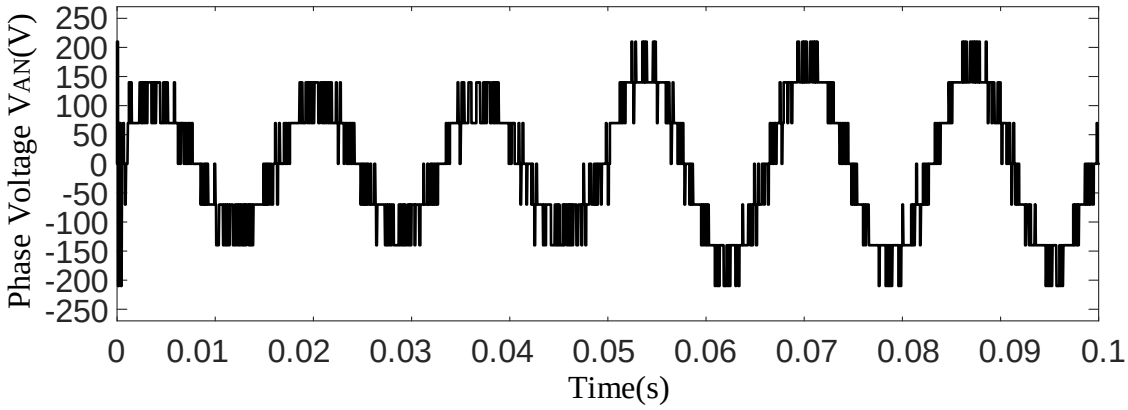

(b) Phase Voltage V_{AN}

Fig.4.6. Simulation Results with M^{2}PC Scheme under Amplitude Change

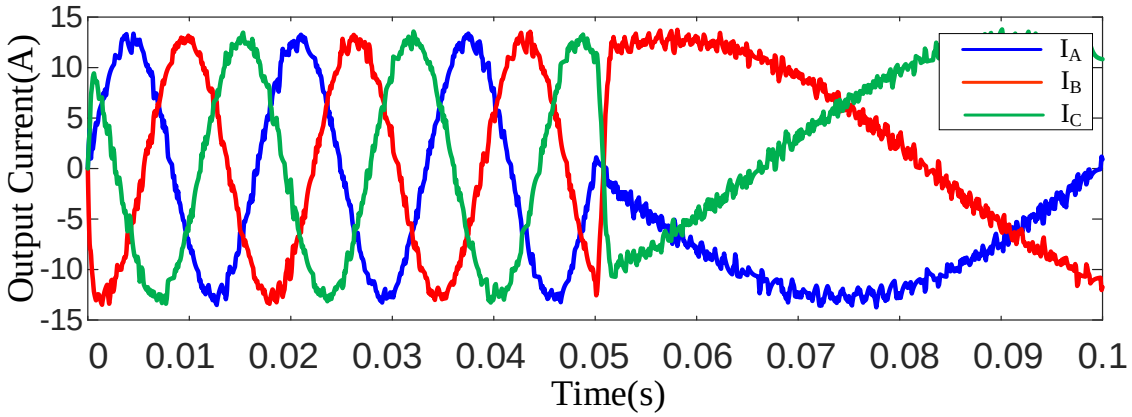

(a) Output Currents

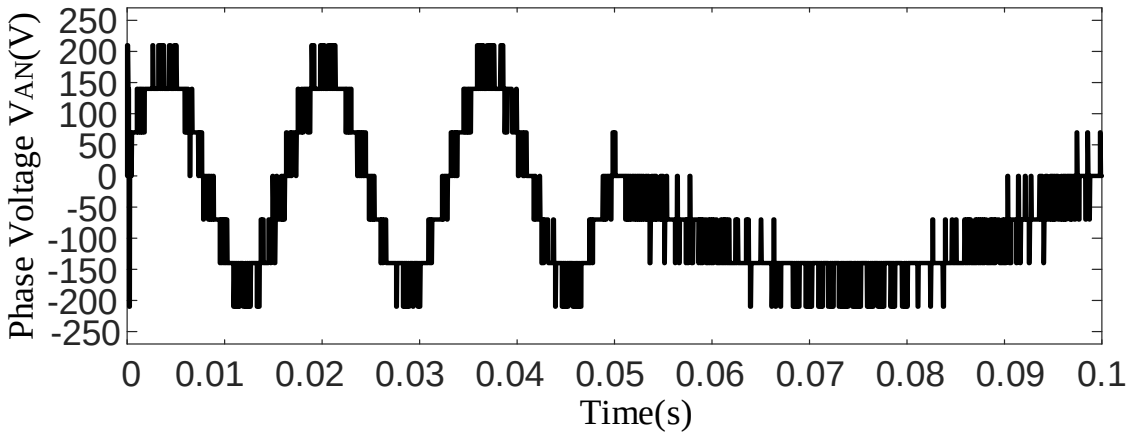

(b) Phase Voltage V_{AN}

Fig.4.7. Simulation Results with M^{2}PC Scheme under Frequency Change

Table.4.1 shows the comparison between conventional FCS-MPC and M^{2}PC algorithms. To compare the THD values, the switching frequency are set to the same value. From the table, the THD of load currents is smaller in M^{2}PC algorithm than that with FCS-MPC algorithm in low switching frequencies.

Also, with the given M^{2}PC algorithm, the number of calculated voltage vectors is reduced from 127 to 9. It means the computation burden for DSP is reduced.

TABLE 4.1 COMPARISON OF THD VALUES WITH FCS-MPC AND M^{2}PC ALGORITHMS

Switching Frequency f_{sw} Average Frequency (for FCS-MPC)	THD of FCS-MPC	THD of M^{2}PC
600	5.99%	5.14%
700	5.48%	4.86%
800	5.10%	4.63%

4.3.2 Simulation Studies with PMSM Load

The parameters of PMSM control depend on Table.3.2. With the PMSM load, M^{2}PC algorithm realizes the control of motor speed with fixed switching frequency.

The simulation of M^{2}PC algorithm includes steady-state and dynamic performance operations of the PMSM. In the first simulation, the motor speed is set to 800rpm and the load torque is 1000 N·m. Fig.4.8(a) shows waveforms of the output currents with PMSM load. Fig.4.8(b) and (c) show the electromagnetic torque T_e and measured motor speed. From the simulation results, the proposed M^{2}PC algorithm performs well under steady state. The THD value of output currents is 1.70%.

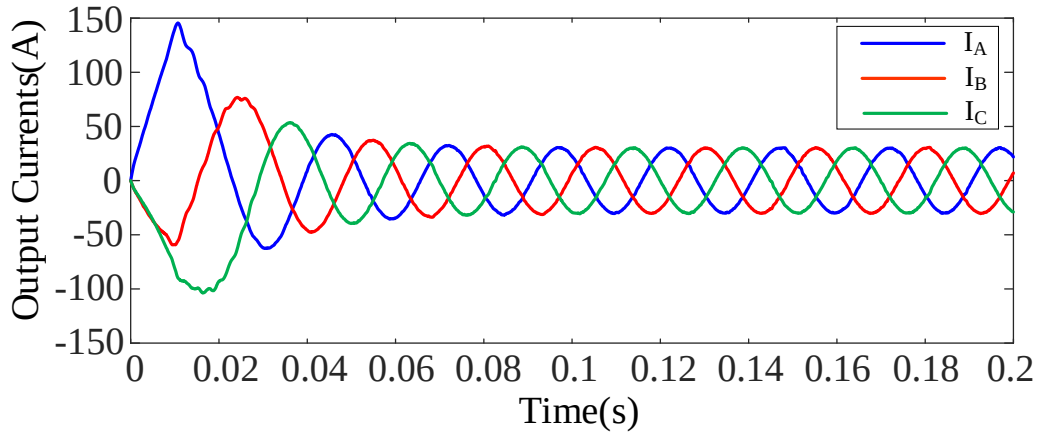

(a) Three-phase Motor Currents

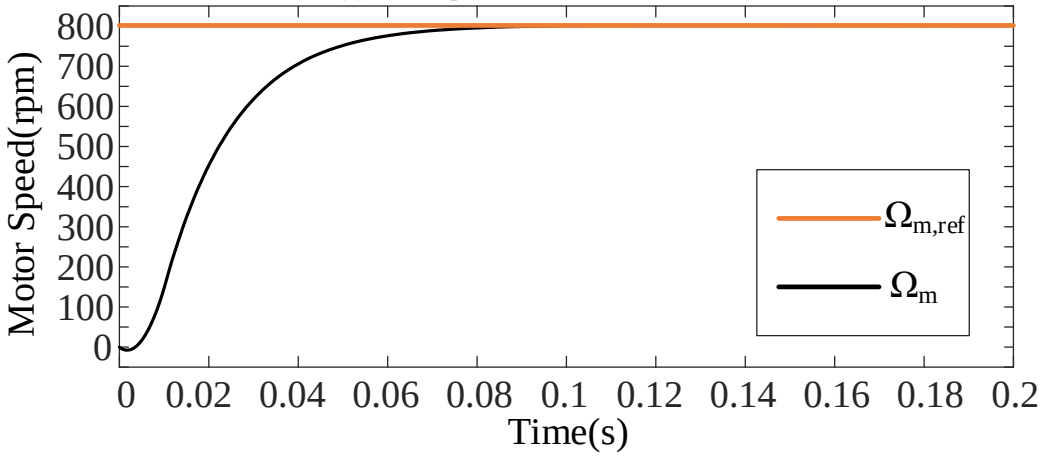

(b) Motor Speed Ω_m

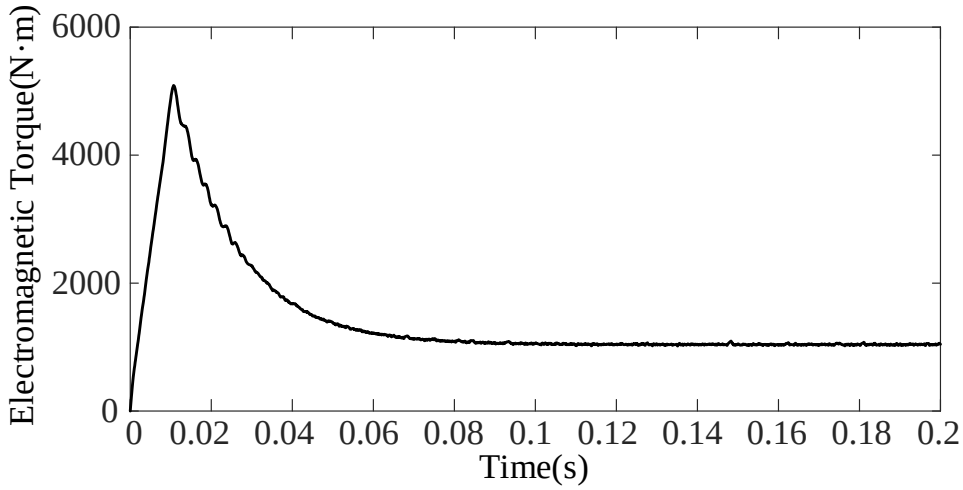

(c) Electromagnetic Torque T_e

Fig.4.8. Steady-state Simulation Results with M^{2}PC Algorithm and PMSM Load

For the dynamic performance evaluation of speed change, the motor speed increases from 600 to 750rpm at time t=0.1s. The simulation waveforms are given in Fig.4.9. The frequency of output currents is determined by mechanical speed from (3.16). In this case, the operation frequency increases from 30Hz to 37.5Hz. The proposed M^2PC algorithm realizes the control of rotor speed. This simulation corresponds with frequency change.

For another dynamic performance evaluation, the change in the load torque is applied while the speed kept at rated speed. The simulation waveforms are shown in Fig.4.10. In this case, the load torque is assumed to increase from 1000 to 1500 N·m and the desired speed is set to 600rpm. With the M^2PC algorithm, the amplitude of output current increases from 34 to 48.5A and the speed is controlled to 600rpm. Also, the drop of motor speed is only 20rpm. The dynamic performance of load torque change is good with M^2PC algorithm.

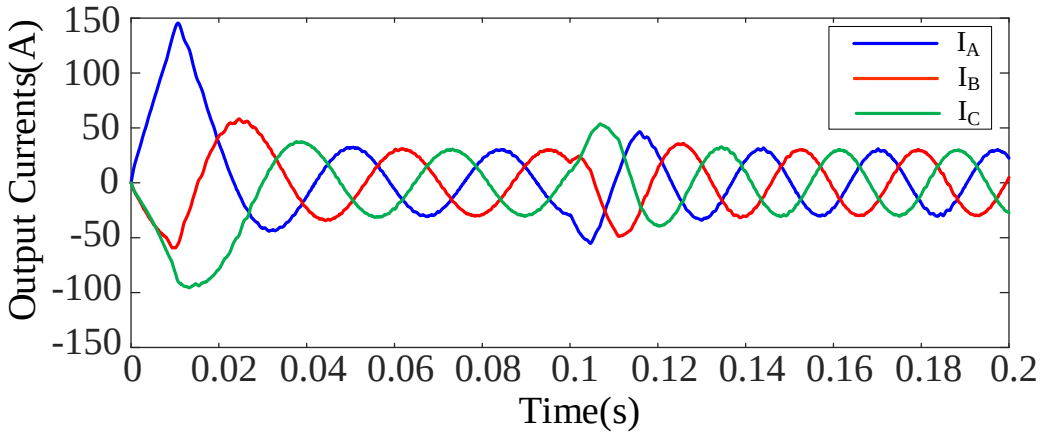

(a) Three-phase Motor Currents

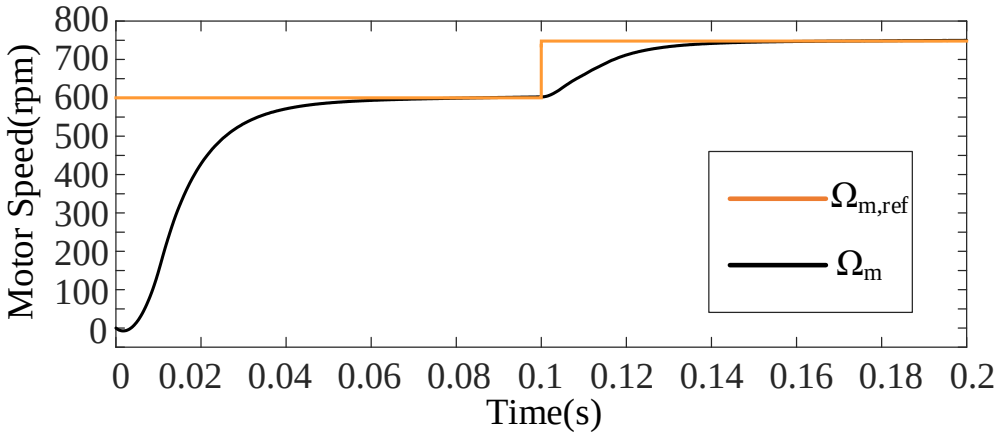

(b) Motor Speed Ω_m

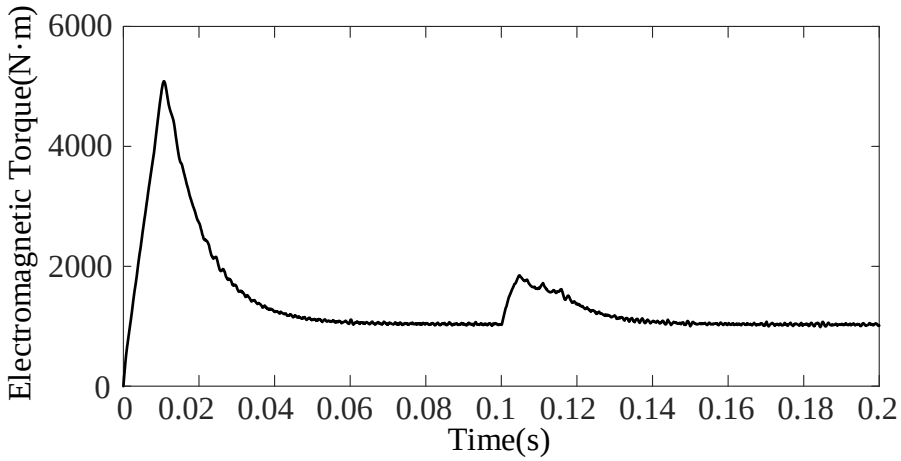

(c) Electromagnetic Torque T_e

Fig.4.9. Simulation Results under Speed Change with M^2PC Algorithm in PMSM.

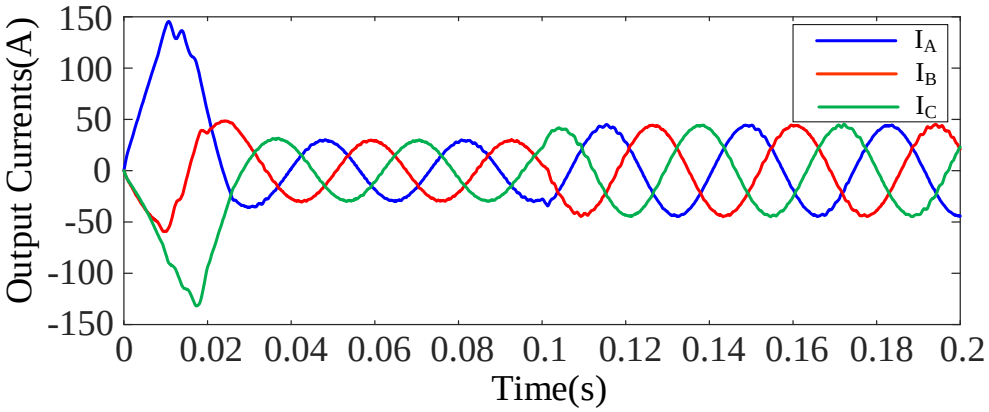

(a) Three-phase Currents

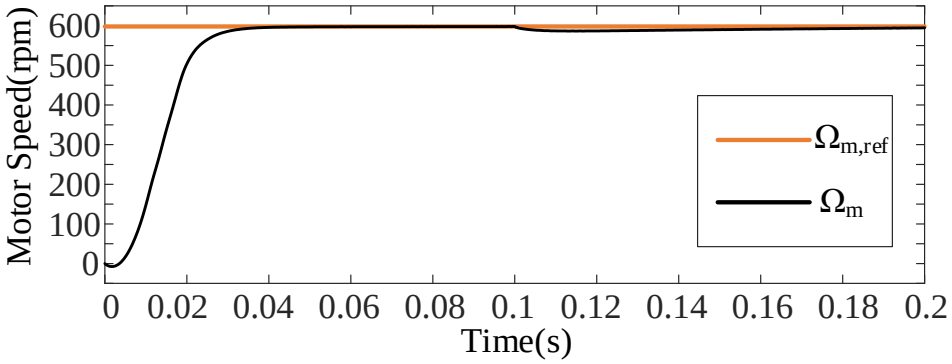

(b) Motor Speed Ω_m

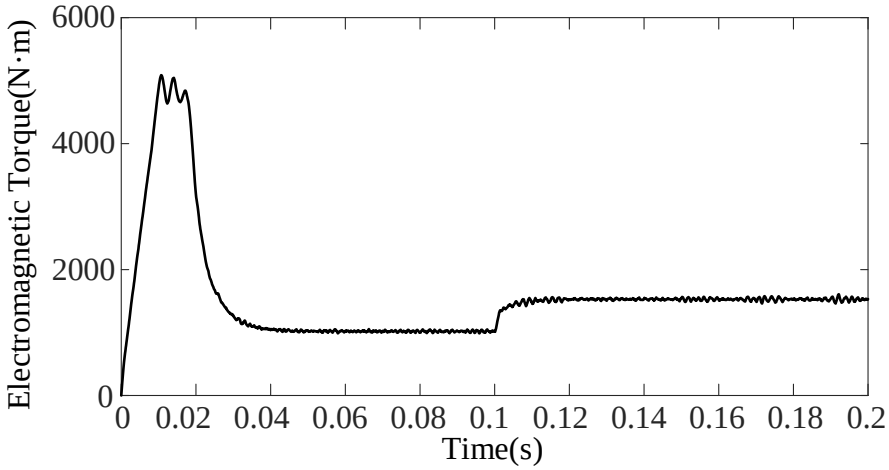

(c) Electromagnetic Torque T_e

Fig.4.10. Simulation Results under Load Torque Change with M^{2}PC Algorithm with PMSM

In these two simulation studies, the M^2PC algorithm can achieve a good dynamic performance with the phase-shifted modulation while the switching frequency is fixed at 900Hz.

From the simulation results, M^2PC algorithm performs well in both RL and PMSM loads.

4.4 Summary

In this chapter, the principles of modulated model predictive control are reviewed. The control algorithm can be applied in the seven-level CHB inverter. In this algorithm, it introduces a new way to define the voltage vector set by calculating the adaptive search step with the error between the measured and reference currents. A cost function is used to obtain the optimal voltage vector. Finally, with the optimal voltage vector, control signals can be provided to control IGBTs in the H-bridges. The simulation results with RL load and PMSM are provided.

With the new algorithm, it inherits the advantages of conventional MPC algorithm and has fixed switching frequency. Also, in this algorithm, only predictions with nine possible voltage vectors are analyzed and the number of current predictions is reduced from 127. However, one concern of the M^2PC algorithm is that the performance of it is based on the accuracy of the parameter and model, which is the drawback of all kinds of MPC algorithms. To reduce the dependency of the performance to model parameters, modulated model-free predictive control is analyzed in the next chapter.

Chapter 5

Modulated Model-Free Predictive Control (M^2FPC) for CHB Inverters

5.1 Introduction

Chapter 4 introduced modulated model predictive control; however, one major concern is that this algorithm relies on the accuracy of parameters and the model. The model is used for the prediction of load currents either as a RL load or PMSM load. In both cases, the model requires accurate value of parameters. It means that the error of parameters and model will make the load currents deviate from the reference values. Therefore, to reduce the negative effects of the parameter and model mismatch, model-free predictive control algorithm (MFPC) is introduced. In this algorithm, the model is built with measured values instead of given values and model. Therefore, the negative effects of parameter and model mismatches can be reduced. The load currents can be controlled normally without considering the error in the model and parameters.

MFPC algorithm is based on the linear model and the prediction relies on observation values. Autoregressive with exogenous input (ARX) model is selected for the prediction of load currents and coefficients are calculated with measurement value by RLS algorithm. In the ARX model, the load currents in α-β coordinates relate to the current and voltage vectors determined in previous time intervals.

In this thesis, the modulated model-free predictive control (M^2FPC) algorithm is studied. Based on M^2PC algorithm, the discrete-time model of (4.1) is replaced with ARX model. The parameters and model do not need to be provided and the model is built with measured values by RLS algorithm. The performance of the proposed modulated model-free predictive control method is compared with conventional MPC. The simulation results verify the better performance of M^2FPC under parameter mismatch.

Compared with the M^2FPC algorithm proposed in the thesis, [51] introduces another M^2FPC algorithm to predict the load currents with current differences with the application of SVM scheme. The currents differences are updated by the current differences and duty ratios in previous sampling times. [52] introduces the ultra-local model to replace the discrete-time electrical model of load currents. Algebraic parameter identification algorithm is applied to estimate the unknown parameters in the RL/PMSM system. [53] also proposes a MFPC algorithm to predict the currents by obtaining the current slope in every sampling time. In this algorithm, the number of voltage vectors can be reduced as well. Compared with other M^2FPC algorithms, the proposed M^2FPC algorithm utilizes the RLS algorithm to realize the current prediction as [27]. In addition, it also applies the M^2PC algorithm to obtain a fixed switching frequency and reduce the computation burden.

Section.5.2 analyzes the RLS algorithm and section.5.3 introduces the M^2FPC algorithm with RL and PMSM loads. Section.5.4 shows the simulation results of M^2FPC and validates its operation. Finally, the performances of M^2PC and M^2FPC algorithms will be compared with a parameter mismatch.

5.2 Recursive Least Square (RLS) Algorithm

Least square mean(LMS) algorithm is a good parameter estimation method with small computation method. However, compared with LMS algorithm, RLS algorithm has faster convergence rates and better control performance[54]. Therefore, to have a better current control in the motor drive, RLS algorithm is applied for parameter estimation for ARX model.

The linear least square(LS) problem is expressed as shown in the equation (5.1):

$$z(i) = H(i)x + \omega(i) \tag{5.1}$$

the vector *x*, which is an unknown constant, is desired to be estimated with the observations by the minimization of cost function as (5.2)[55]:

$$J(k) = \sum_{i=1}^{k} R(i)^{-1}[z(i) - H(i)x]^2 \tag{5.2}$$

$H(i)$ is the known vector for x. $\omega(i)$ is the measurement error in the model. In the cost function, the weighing factor, $R(i)^{-1}$, is used for weighing the importance of each mean square error.

The equation(5.2) can be written in a compact form as (5.3):

$$J(k) = [z^k - H^k x]^T (R^k)^{-1}[z^k - H^k x] \tag{5.3}$$

where z^k is measured vector as (5.4). H^k is the measured matrix as (5.5). R^k is the matrix of weighing factors as (5.6).

$$z^k = [z(1) \quad z(2) \quad ... \quad z(k)]^T \tag{5.4}$$

$$H^k = \begin{bmatrix} H(1) \\ H(2) \\ ... \\ H(k) \end{bmatrix} \tag{5.5}$$

$$R^k = \begin{bmatrix} R(1) & \dots & 0 \\ \vdots & \ddots & \vdots \\ 0 & \cdots & R(k) \end{bmatrix} \tag{5.6}$$

In the LS estimation, the equation (5.3) should be minimized. To find the minimum, the gradient should be set to 0 with respect to *x*. The gradient is obtained by (5.7) and the optimal result of the equation is as (5.8) [55]:

$$\nabla_x J(k) = -2(H^k)^T(R^k)^{-1}[z^k - H^k x] = 0 \tag{5.7}$$

$$\hat{x}(k) = [(H^k)^T(R^k)^{-1}(H^k)]^{-1}(H^k)^T(R^k)^{-1}z^k \tag{5.8}$$

With the matrix of R^k is positive definite, the Hessian of $J(k)$ is positive definite with *x* as well. Therefore, the extremum of cost function with $\hat{x}(k)$ is the minimum. For the discrete-time model, *k* is the sampling time.

With the calculation of $\hat{x}(k)$, the LS estimator is defined. Also, $\hat{x}(k)$ is a random variable if the measurement errors $\omega(i)$ are random variables. In this thesis, it is assumed that $\omega(i)$ are uncorrelated and zero-mean random variables. The expectation of $\hat{x}(k)$ is as (5.9). The covariance matrix of LS estimator $P(k)$ is as (5.10).

$$\begin{aligned} E[\hat{x}(k)] &= [(H^k)^T(R^k)^{-1}H^k]^{-1}(H^k)^T(R^k)^{-1}E(z^k) \\ &= [(H^k)^T(R^k)^{-1}H^k]^{-1}(H^k)^T(R^k)^{-1}E[H^k x + \omega^k] \end{aligned} \tag{5.9}$$

$$\begin{aligned} P[\hat{x}(k)] &= E[\{\hat{x}(k) - E[\hat{x}(k)]\}\{\hat{x}(k) - E[\hat{x}(k)]\}^T] \\ &= E[\{\hat{x}(k) - x\}\{\hat{x}(k) - x\}^T] \\ &= [(H^k)^T(R^k)^{-1}H^k]^{-1}(H^k)^T(R^k)^{-1}E[\omega^k(\omega^k)^T](R^k)^{-1}H^k[(H^k)^T(R^k)^{-1}H^k] \\ &= [(H^k)^T(R^k)^{-1}H^k]^{-1} \end{aligned} \tag{5.10}$$

In (5.8), the inverse matrix should be calculated and updated in each sampling time. The computation burden for inverse matrix is large. Also, to make the algorithm perform better in the DSP platform, a recursive form of LS estimator should be designed. Therefore, the recursive least square algorithm should be applied in the control.

From (5.10), the covariance matrix in the sampling time k+1, $P(k+1)$, can be rewritten as (5.11):

$$\begin{aligned} P(k+1) &= [(H^{k+1})^T (R^{k+1})^{-1} H^{k+1}]^{-1} \\ &= ([(H^k)^T \quad H(k+1)^T] \begin{bmatrix} R^k & 0 \\ 0 & R(k+1) \end{bmatrix} \begin{bmatrix} H^k \\ H(k+1) \end{bmatrix})^{-1} \\ &= [(H^k)^T (R^k)^{-1} H^k + H(k+1)^T R(k+1)^{-1} H(k+1)]^{-1} \\ &= [P(k)^{-1} + H(k+1)^T R(k+1)^{-1} H(k+1)]^{-1} \end{aligned} \tag{5.11}$$

Then, to find the relationship between $P(k+1)$ and $P(k)$, the Woodbury's matrix identity can be used for equation (5.11), which is as (5.12)[56]:

$$(A + uv^H)^{-1} = A^{-1} - \frac{A^{-1} u v^H A^{-1}}{1 + v^H A^{-1} u} \tag{5.12}$$

By applying (5.12) to (5.11), we set A=$P(k)$, u=$H(k+1)^T R(k+1)$, and v=$H(k+1)^T$. The covariance matrix $P(k+1)$ in the sampling time k+1 will be transformed to (5.13).

$$\begin{aligned} P(k+1) &= P(k) - \frac{P(k) H(k+1)^T H(k+1) P(k)}{H(k+1) P(k) H(k+1)^T + R(k+1)} \\ &= \left[I - \frac{P(k) H(k+1)^T H(k+1)}{H(k+1) P(k) H(k+1)^T + R(k+1)} \right] P(k) \end{aligned} \tag{5.13}$$

In (5.12), we define the variable of the gain matrix, $G(k+1)$ as (5.14). With this equation, the covariance matrix can be written as (5.15). With (5.14) and (5.15), the LS estimation $\hat{x}(k)$ can be written as (5.16).

$$G(k+1) = \frac{P(k)H(k+1)^T}{H(k+1)P(k)H(k+1)^T + R(k+1)} \tag{5.14}$$

$$P(k+1) = [I - G(k+1)H(k+1)]P(k) \tag{5.15}$$

$$\hat{x}(k+1) = P(k+1)(H^{k+1})^T(R^{k+1})^{-1}z^{k+1}$$

$$= P(k+1)[(H^k)^T \quad H(k+1)^T]\begin{bmatrix} R^k & 0 \\ 0 & R(k+1) \end{bmatrix}^{-1}\begin{bmatrix} z^k \\ z(k+1) \end{bmatrix}$$

$$= P(k+1)(H^k)^T(R^k)^{-1}z^k + P(k+1)H(k+1)^T R(k+1)^{-1}z(k+1)$$

$$= [I - G(k+1)H(k+1)]P(k)(H^k)(R^k)^{-1}z^k + G(k+1)z(k+1$$

$$= \hat{x}(k) + G(k+1)[z(k+1) - H(k+1)\hat{x}(k)] \tag{5.16}$$

With (5.14)-(5.16), the estimation of $\hat{x}(k+1)$ can be obtained in a recursive form with the previous estimation $\hat{x}(k)$. For the recursive least square algorithm, the gain matrix $G(k+1)$ and $P(k+1)$ should be calculated first. The RLS estimation is updated with the sum of previous estimation and the product of the estimation error and gain matrix.

Therefore, with the RLS estimator, the load currents can be predicted without the electrical models. Therefore, the modulated model-free predictive control performs well with RLS algorithm.

5.3 Modulated Model-free Predictive Control (M^{2}FPC)

Chapter 4 analyzes the M^{2}PC algorithm. Based on M^{2}PC algorithm, M^{2}FPC algorithm applies RLS estimator to predict the load currents in the time instant $k+1$. With

the RLS algorithm, the electrical models of RL and PMSM loads can be replaced by ARX model. Then, the optimal voltage vector can be found using the discrete-time ARX model through the minimization of a cost function. The control signals are also generated by phase-shifting modulation.

The electrical models of RL and PMSM loads are different. Therefore, the modulated model-free predictive control algorithms for the two algorithms are discussed separately:

5.3.1 Modulated Model-Free Predictive Control (M^{2}FPC) with RL Load

In the RL load, the model of load currents is assumed to be linear to simplify the algorithm. Under this circumstance, the ARX model of load currents in α-β coordinate with RL load is defined as (5.17) and (5.18):

$$\begin{aligned} i_\alpha(k+1) = {} & a_1^\alpha i_\alpha(k) + a_2^\alpha i_\alpha(k-1) + \cdots + a_m^\alpha i_\alpha(k+1-m) \\ & + b_1^{\alpha\alpha} u_\alpha(k+1) + \cdots + b_n^{\alpha\alpha} u_\alpha(k+2-n) \\ & + b_1^{\alpha\beta} u_\beta(k+1) + \cdots + b_n^{\alpha\beta} u_\beta(k+2-n) \end{aligned} \tag{5.17}$$

$$\begin{aligned} i_\beta(k+1) = {} & a_1^\beta i_\beta(k) + a_2^\beta i_\beta(k-1) + \cdots + a_m^\beta i_\beta(k+1-m) \\ & + b_1^{\beta\alpha} u_\alpha(k+1) + \cdots + b_n^{\beta\alpha} u_\alpha(k+2-n) \\ & + b_1^{\beta\beta} u_\beta(k+1) + \cdots + b_n^{\beta\beta} u_\beta(k+2-n) \end{aligned} \tag{5.18}$$

In these two equations, i_α and i_β are measured load currents. u_α and u_β are predicted voltages in α-β coordinate in M^{2}PC algorithm with (4.2). m is the order of load currents

and *n* is the order of predicted voltage vectors. The order of polynomial of output current is determined by *m* and *n*.

From (5.17) and (5.18), the values of i_α, i_β , u_α and u_β are known parameters. The measured load currents and predicted voltage vectors are gathered in vectors $\boldsymbol{\varphi_\alpha}$ and $\boldsymbol{\varphi_\beta}$. They are defined as (5.19) and (5.20):

$$\varphi_\alpha = [i_\alpha(k) \quad i_\alpha(k-1) \ldots. \ i_\alpha(k+1-m) \quad u_\alpha(k+1) \quad \ldots \quad u_\alpha(k+2-n) \quad u_\beta(k+1) \quad \ldots \quad u_\beta(k+2-n)]^T \tag{5.19}$$

$$\varphi_\beta = [i_\beta(k) \quad i_\beta(k-1) \quad \ldots \quad i_\beta(k+1-m) \quad u_\alpha(k+1) \quad \ldots \quad u_\alpha(k+2-n) \quad u_\beta(k+1) \quad \ldots \quad u_\beta(k+2-n)]^T \tag{5.20}$$

Similarly, the unknown coefficients of the known values in (5.17) and (5.18) to be identified and can be defined as the vectors $\boldsymbol{\theta_\alpha}$ and $\boldsymbol{\theta_\beta}$ respectively:

$$\theta_\alpha = \left[a_1^\alpha \quad a_2^\alpha \quad \ldots \quad a_m^\alpha \quad b_1^{\alpha\alpha} \quad \ldots \quad b_n^{\alpha\alpha} \quad b_1^{\alpha\beta} \quad \ldots \quad b_n^{\alpha\beta}\right]^T \tag{5.21}$$

$$\theta_\beta = \left[a_1^\beta \quad a_2^\beta \quad \ldots \quad a_m^\beta \quad b_1^{\beta\alpha} \quad \ldots \quad b_n^{\beta\alpha} \quad b_1^{\beta\beta} \quad \ldots \quad b_n^{\beta\beta}\right]^T \tag{5.22}$$

Therefore, the problem has been transformed to a LS problem. The key for the M^{2}FPC algorithm is to calculate the unknown parameters. With the calculations of $\boldsymbol{\theta_\alpha}$ and $\boldsymbol{\theta_\beta}$, the load currents can be estimated with load currents and predicted voltage vectors in previous sampling times.

To determine the unknown vectors of $\boldsymbol{\theta_\alpha}$ and $\boldsymbol{\theta_\beta}$, the RLS estimator should be applied. The weighing factor of each *R* is 1. The equations of (5.14) to (5.16) are transferred to the following equations:

$$G(k) = \frac{P(k-1)\varphi(k)}{\varphi^T(k)P(k-1)\varphi(k)+1}$$

$$P(k) = \big(I - G(k)\varphi^T(k)\big)P(k-1)$$

$$\theta(k) = \theta(k-1) + G(k)e(k) \tag{5.23}$$

In these equations, k represents the variables updated in the sampling time k. Also, $e_x(k)$(x=α and β) is the error between measured and estimated values of the load currents in the previous sampling time as shown in (5.24):

$$e_x(k) = i_x(k) - \varphi_x^T(k-1)\theta_x(k-1) \tag{5.24}$$

Based on these equations, the load current in α-β coordinates can be predicted as (5.25) with ARX model (x=α and β). The mathematical model of (4.1) is replaced by (5.25):

$$i_x(k+1) = \varphi_x^T(k)\theta_x(k) \tag{5.25}$$

The block diagram of RLS algorithm is shown as Fig.5.1. With RLS estimator, the model is built in the M^{2}PC algorithm. Then, the M^{2}FPC algorithm with a RL load can be realized.

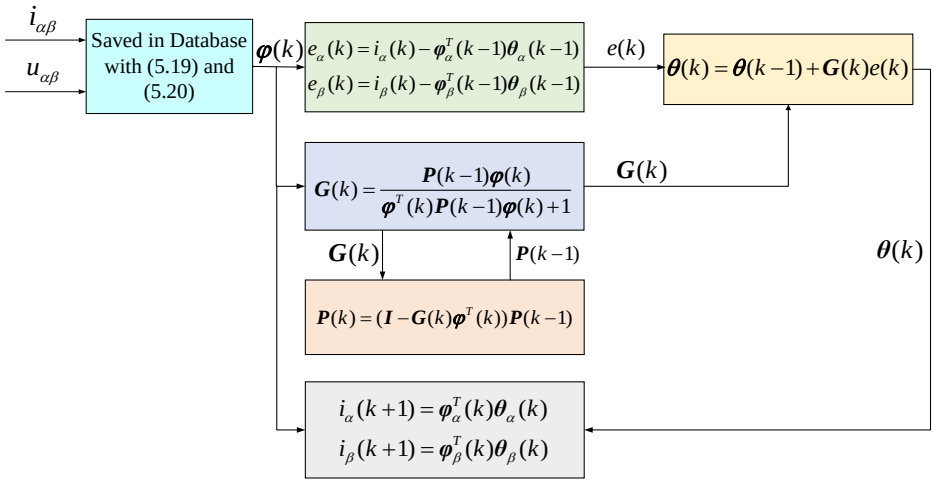

Fig.5.1. The Block Diagram of RLS Algorithm with RL Load

5.3.2 Modulated Model-free Predictive Control with PMSM Load

With the PMSM load, the ARX model is different. The output currents, i_d and i_q, are coupling with each other from (3.14). For the current in another axis, the electrical speed ω is needed because it is not a constant. Therefore, the ARX model with PMSM load is as shown in (5.26) and (5.27):

$$\begin{aligned} i_d(k+1) &= a_1^{dd} i_d(k) + a_2^{dd} i_d(k-1) + \cdots + a_p^{dd} i_d(k+1-p) \\ &+ a_1^{dq} \omega i_q(k) + a_2^{dq} \omega i_q(k-1) + \cdots + a_p^{dq} \omega i_q(k+1-p) \\ &+ b_1^{dd} v_d(k+1) + \cdots + b_s^{dd} v_d(k+2-s) \\ &+ b_1^{dq} v_q(k+1) + \cdots + b_s^{dq} v_q(k+2-s) \end{aligned} \tag{5.26}$$

$$\begin{aligned} i_q(k+1) &= a_1^{qd} \omega i_d(k) + a_2^{qd} \omega i_d(k-1) + \cdots + a_p^{qd} \omega i_d(k+1-p) \\ &+ a_1^{qq} i_q(k) + a_2^{qq} i_q(k-1) + \cdots + a_p^{qq} i_q(k+1-p) \\ &+ b_1^{qd} v_d(k+1) + \cdots + b_s^{qd} v_d(k+2-s) \\ &+ b_1^{qq} v_q(k+1) + \cdots + b_s^{qq} v_q(k+2-s) + c^{\omega} \omega \end{aligned} \tag{5.27}$$

For the prediction of i_d, it includes electrical speed, ω, because i_d has the term of $\Psi_f \cdot \omega$ from (3.14). In the two equations, p and s are the orders of current and voltage vectors respectively.

Similar to the M^{2}FPC algorithm with RL load, the measured load currents and voltages are gathered in vectors $\boldsymbol{\varphi_d}$ and $\boldsymbol{\varphi_q}$. They are defined as (5.28) and (5.29):

$$\begin{aligned} \varphi_d = [&i_d(k) \quad i_d(k-1) \quad \ldots \quad i_d(k+1-p) \\ &\omega i_q(k) \quad \omega i_q(k-1) \quad \ldots \quad \omega i_q(k+1-p) \end{aligned}$$

$$v_d(k+1) \quad \dots \quad v_d(k+2-s)$$
$$v_q(k+1) \quad \dots \quad v_q(k+2-s)]^T \tag{5.28}$$

$$\varphi_q = [\omega i_d(k) \quad \omega i_d(k-1) \quad \dots \quad \omega i_d(k+1-p)$$
$$i_q(k) \quad i_q(k-1) \quad \dots \quad i_q(k+1-p)$$
$$v_d(k+1) \quad \dots \quad v_d(k+2-s)$$
$$v_q(k+1) \quad \dots \quad v_q(k+2-s) \quad \omega]^T \tag{5.29}$$

In addition, the unknown coefficient in the (5.26) and (5.27) are defined as $\boldsymbol{\theta_d}$ and $\boldsymbol{\theta_q}$.

$$\theta_d = [a_1^{dd} \quad a_2^{dd} \quad \dots \quad a_p^{dd} \quad a_1^{dq} \quad a_2^{dq} \quad \dots \quad a_p^{dq}$$
$$b_1^{dd} \quad \dots \quad b_s^{dd} b_1^{dq} \quad \dots \quad b_s^{dq}]^T \tag{5.30}$$

$$\theta_q = [a_1^{qd} \quad a_2^{qd} \quad \dots \quad a_p^{qd} \quad a_1^{qq} \quad a_2^{qq} \quad \dots \quad a_p^{qq}$$
$$b_1^{qd} \quad \dots \quad b_s^{qd} b_1^{qq} \quad \dots \quad b_s^{qq} \quad c^{\omega}]^T \tag{5.31}$$

Similar to RL load, the weighing factor of each *R* is 1. Then, the equations of (5.23) are used to update the vectors of $\boldsymbol{\theta_d}$ and $\boldsymbol{\theta_q}$. In this case, the error between measured and estimated values of the current vector is defined as (5.32)(*x*=*d* and *q*). Therefore, the discrete-time mathematical model of PMSM load in (3.14) is replaced by (5.33).

$$e_x(k) = i_x(k) - \varphi_x^T(k-1)\theta_x(k-1) \tag{5.32}$$

$$i_x(k+1) = \varphi_x^T(k)\theta_x(k) \tag{5.33}$$

The block diagram for RLS algorithm with PMSM load is shown as Fig.5.2. With the RLS estimator, the prediction of load currents with PMSM is realized with the ARX

model similar to the case with RL load. The only difference is modify the load currents are replaces by i_d and i_q.

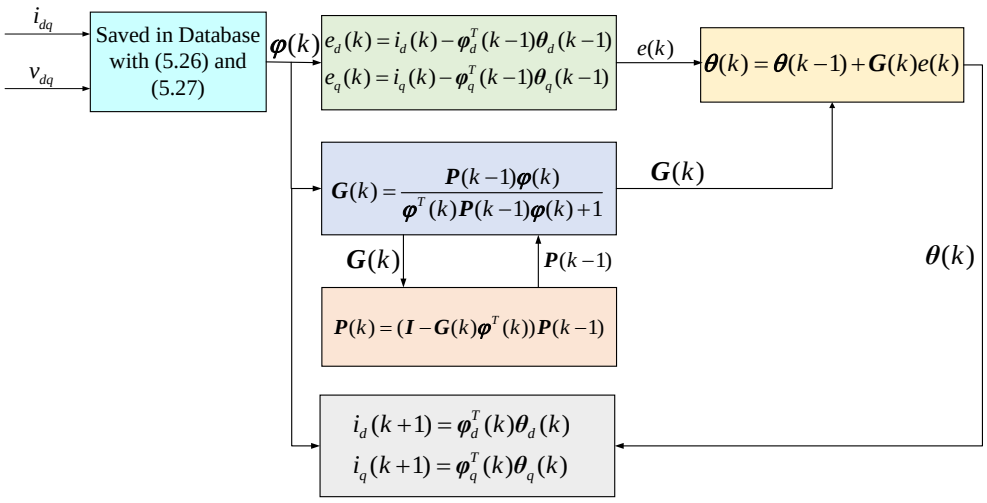

Fig.5.2. The Block Diagram of RLS Algorithm with PMSM Load

Therefore, with RLS algorithm, the discrete-time ARX model of load currents is obtained with measured values instead of given parameters and models. Therefore, the problem of parameter and model mismatch is solved, and the modulated model-free predictive control reduces the dependency of given parameters and models. In the next section, the simulation results of M^{2}FPC algorithm are provided.

5.4 Simulation Results

In the section, simulation studies of M^{2}FPC algorithm with RL and PMSM load are provided to validate the feasibility of M^{2}FPC algorithm. The parameters of the load are as section 4.3. From the simulation results, the M^{2}FPC algorithm performs well with RL and PMSM loads. Also, the comparison of M^{2}PC and M^{2}FPC algorithms with parameter mismatch is provided. The results show that if there is an error in the given parameter, the

amplitude of load currents with M^2PC algorithm cannot reach the controlled value. However, with the M^2FPC algorithm, the load currents can be controlled very well.

5.4.1 Simulation Results of M^2FPC Algorithm with RL Load

In this part, the simulation results of M^2FPC algorithm with RL load are provided. Similar to M^2PC algorithm, the steady-state and dynamic performances of M^2FPC algorithms are given to validates performances of this algorithm. Then, the comparison between M^2PC and M^2FPC algorithms is given to verify the advantages of M^2FPC algorithm with parameter mismatch.

With the steady-state performance, the RMS value of load currents is set to 8A. The waveforms of load currents and phase voltage are shown as Fig.5.3. From the simulation results, M^2FPC algorithm performs well under steady-state performance. The THD value of load currents is 5.12% while the switching frequency is 900Hz.

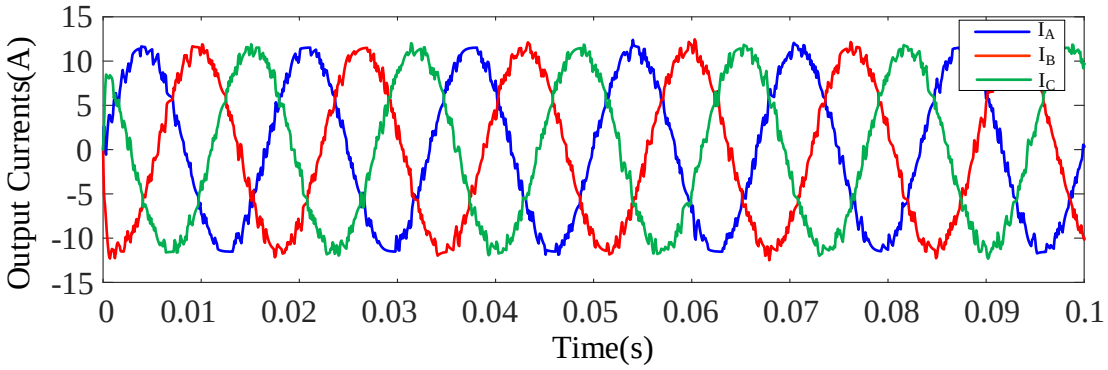

(a) Load Currents

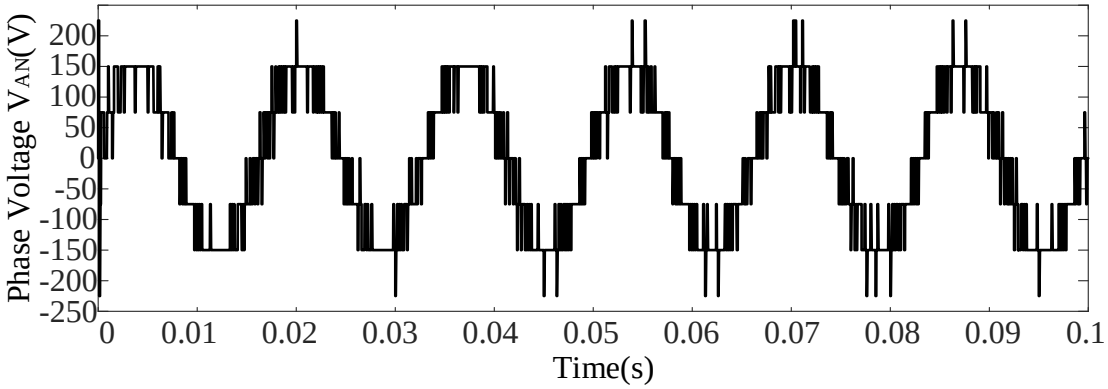

(b) Phase Voltage V_{AN}

Fig.5.3. The Waveforms of M^{2}FPC Algorithm in Steady-State and RL Load

Also, the dynamic performances of M^{2}FPC algorithms are provided as shown in Fig.5.4 and Fig.5.5. Fig.5.4 shows the performance of amplitude change from 6A to 8A at t=0.1s. Fig.5.5 shows the performance of frequency change decreasing from 60Hz to 10Hz at t=0.1s. From the simulation results, M^{2}FPC algorithm demonstrates a good dynamic performance.

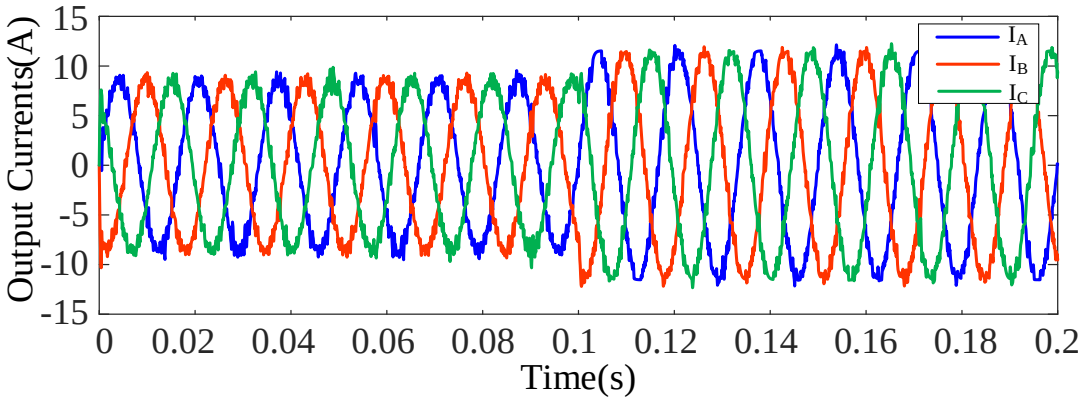

(a) Load Currents

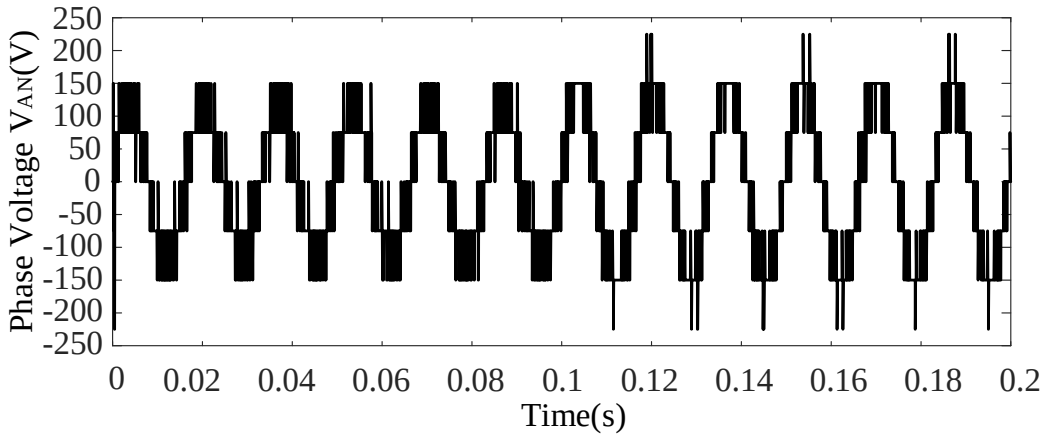

(b) Phase Voltage V_{AN}

Fig.5.4 The Waveforms of M^{2}FPC Algorithm under Amplitude Change with RL Load

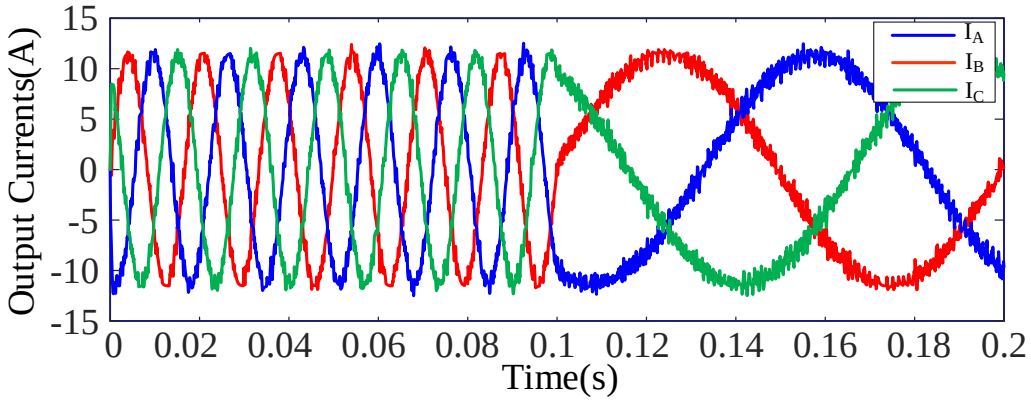

(a) Load Currents

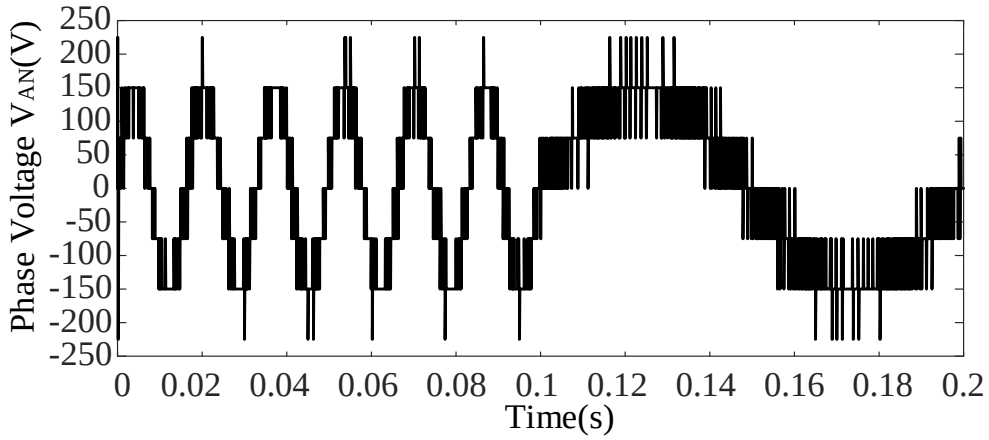

(b) Phase Voltage V_{AN}

Fig.5.5. The Waveforms of M²FPC Algorithm under Frequency Change with RL Load

Finally, the comparison between M²PC and M²FPC algorithms is provided as Fig.5.6 with parameter mismatch. The RMS value of load currents is set to 8A. In the simulation, the parameters of load resistance and inductance in the controller are subject to (5.34).

$$\hat{R_o} = 0.3R_o$$

$$\hat{L_o} = 0.3L_o \tag{5.34}$$

From the waveforms of load currents, the amplitude of load currents deviates from the reference value with M^{2}PC algorithm. However, with the M^{2}FPC algorithm, the load currents are controlled at the desired values.

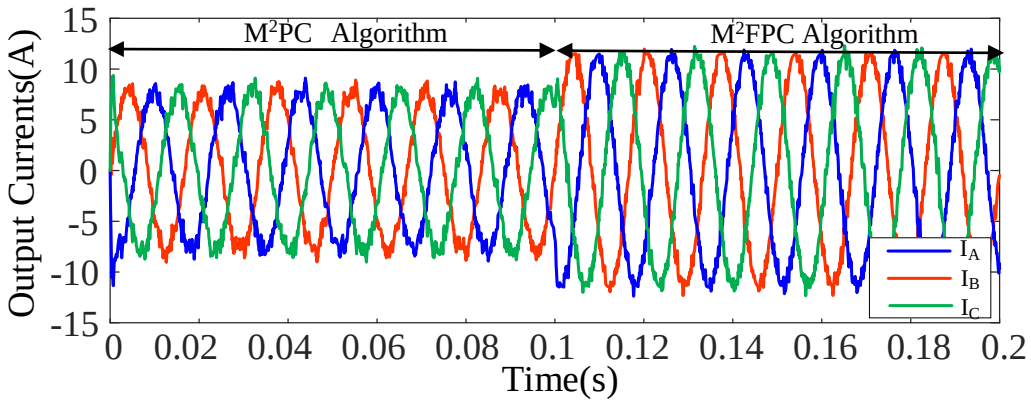

Fig.5.6. Waveforms of Output Currents with M^{2}PC and M^{2}FPC Algorithms with Parameter Mismatch

In the simulation, the M^{2}FPC algorithm realizes the control of output currents with RL load. The M^{2}FPC algorithm has a better performance if there is a parameter mismatch between the controller and the load.

5.4.2 Simulation Results of M^{2}FPC Algorithm with PMSM Load

In this section, the simulation results of M^{2}FPC algorithm with PMSM are provided. The simulation parameters are as stated in Table.3.2. The load currents, motor speed, and electromagnetic torque of M^{2}FPC algorithm under state-state performance are shown as Fig.5.7. The motor speed is 800rpm and the load torque is 1000N·m. As can be seen from the simulation results, the M^{2}FPC algorithm performs well under steady-state performance. The THD value of load currents is 2.53%.

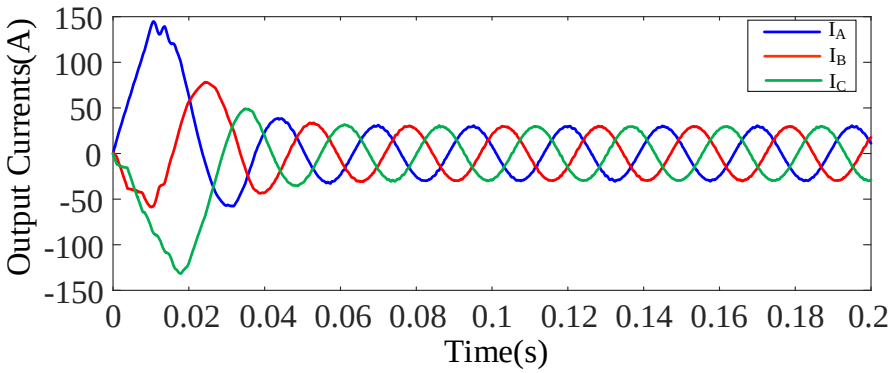

(a) Three-phase Currents

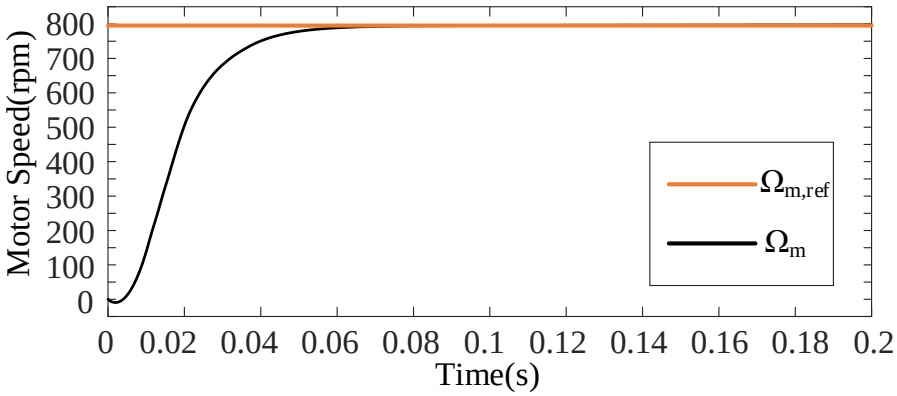

(b) Motor Speed Ω_m

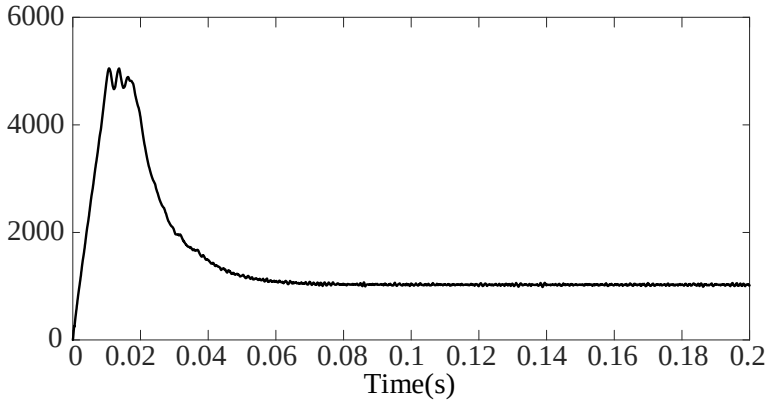

(c) Electromagnetic Torque T_e

Fig.5.7 Steady-state Simulation Results with M^2FPC Algorithm and PMSM Load

Also, dynamic performance of the M^{2}FPC algorithm was studied. Fig.5.8 shows the performance of M^{2}FPC algorithm under the speed change from 600 to 750rpm at t=0.1s. In this case, the operation frequency increases from 30 to 37.5Hz.

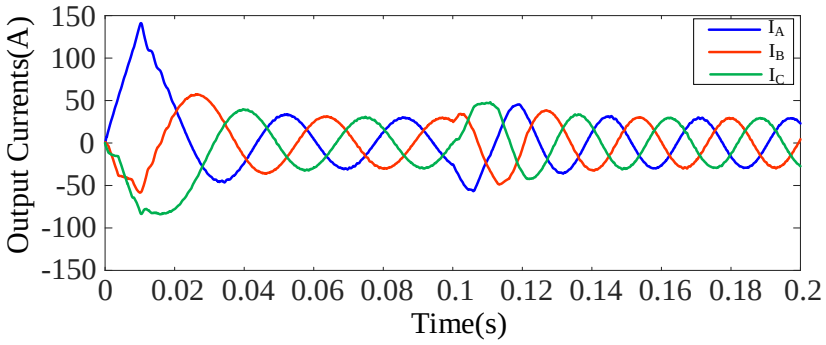

(a) Three-phase Currents

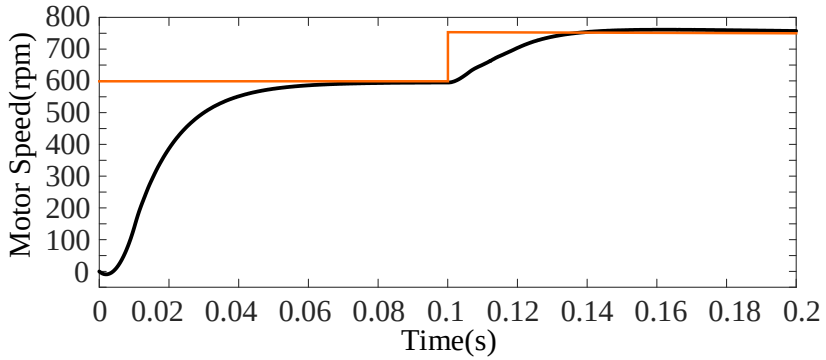

(b) Motor Speed Ω_m

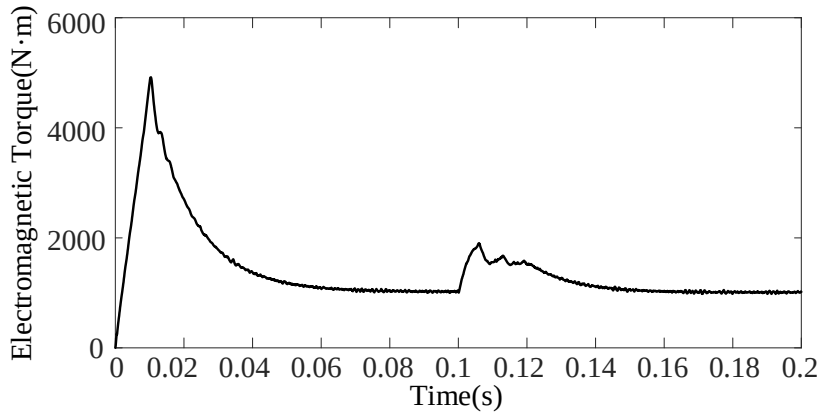

(c) Electromagnetic Torque T_e

Fig.5.8. Simulation Results with M^{2}FPC Algorithm under Speed Change

Fig.5.9 shows the performance of M^{2}FPC algorithm under the change of load torque increasing from 1000 to 1500N·m at t=0.1s. The motor speed is set to be 600rpm. The drop of motor speed is small and can return to the desired value. The amplitude of load currents increases from 30 to 44.5 A. It can be seen that the speed can be maintained at the reference speed while the torque is changing.

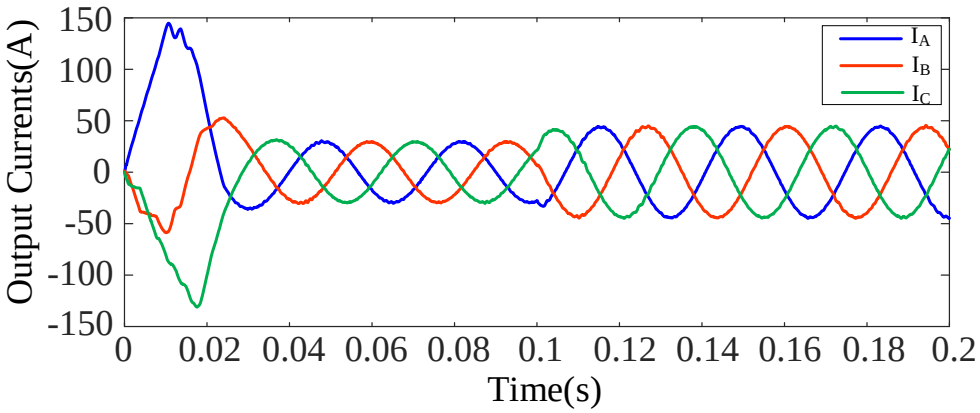

(a) Three-phase Currents

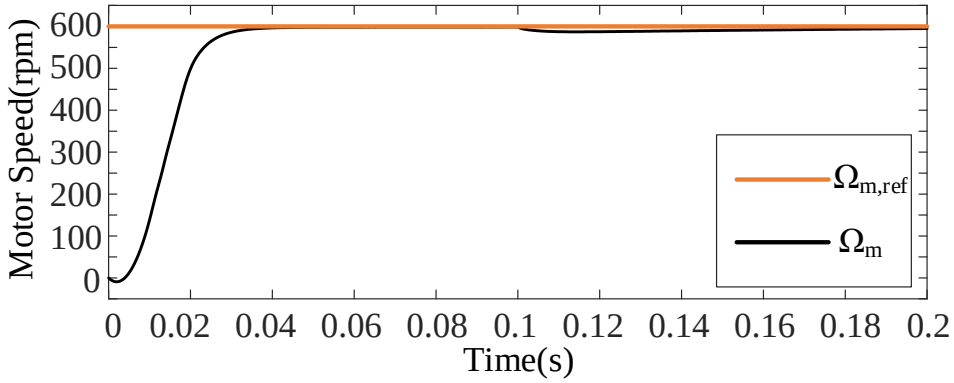

(b) Motor Speed Ω_m

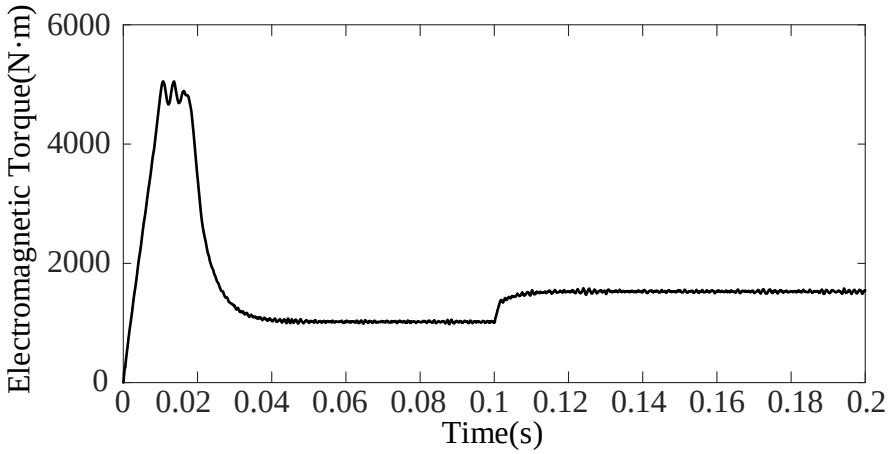

(c) Electromagnetic Torque T_e

Fig.5.9. Simulation Results with M^{2}FPC Algorithm under Speed Change

The two dynamic performances verify the feasibility of M^{2}FPC algorithms with PMSM load. It means the ARX model of PMSM load can be built by RLS algorithm.

Fig.5.10 shows the comparison between the M^{2}PC and M^{2}FPC algorithms under parameter mismatch. In this case, the value of stator inductance in the controller $L_{s\text{-}con}$ is assumed to be 1% of the value in the hardware setup as (5.35). Also, the motor speed needs to be controlled to 600rpm. From the simulation results, the motor speed can be controlled to the desired value with M^{2}FPC algorithm. In addition, with the M^{2}PC algorithm, the motor speed cannot be controlled to 600rpm if there is a parameter mismatch in the system because of false prediction.

$$L_{s-con} = 0.01 L_s \tag{5.35}$$

Therefore, the performance of M^{2}PC algorithm relies on the accuracy of given parameters and model. M^{2}FPC algorithm reduces the dependence on the given parameters

compared with M^{2}PC algorithm. It performs well even if there is a parameter mismatch between the controller and the hardware system.

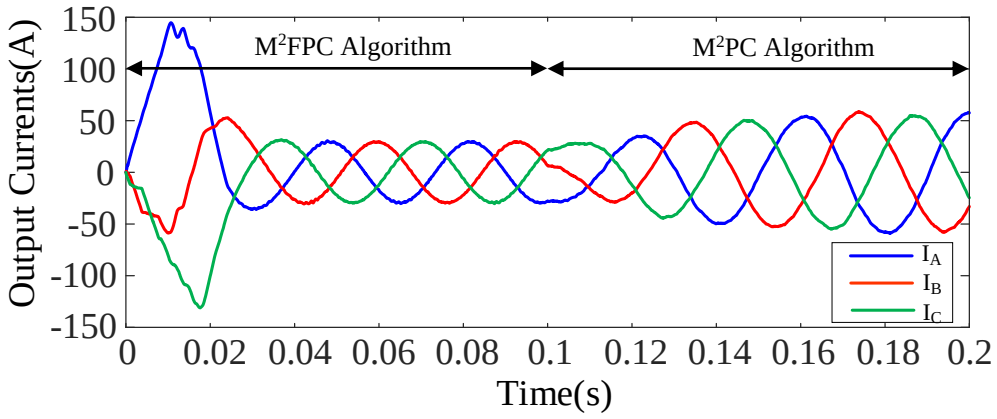

(a) Three-phase Currents

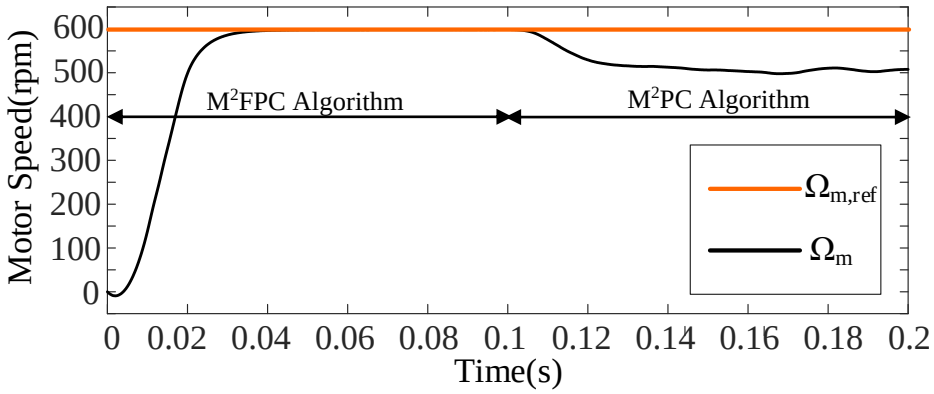

(b) Motor Speed Ω_m

Fig.5.10. Comparison of M^{2}PC and M^{2}FPC Algorithms with Parameter Mismatch

5.5 Summary

In this chapter, M^{2}FPC algorithm with ARX model is studied. From the simulation results, M^{2}FPC algorithm performs well in the CHB inverter with RL and PMSM loads.

The M^2FPC algorithm realizes the goal of building the ARX model for the load current prediction with RLS algorithm. With the RLS estimator, the discrete-time model is built with measured values instead of given parameters and physical model. From simulation results, the M^2FPC does not rely on the given parameters and model, which reduces the negative effects of parameter mismatch. Experimental results are provided in Chapter 7 to validate the feasibility of the developed M^2FPC algorithm.

Chapter 6

Fault Detection and Localization (FDL) in CHB Inverters

6.1. Introduction

In this chapter, a new algorithm for fault detection and localization is developed. One advantage of CHB topology is that it is suitable for fault-tolerant control by isolating the faulty power cell. If there is a fault in one power cell, the CHB inverter will be shut down. Then, the faulty power cell will be bypassed and isolated from the CHB inverter [57]. Finally, the fault-tolerant control algorithm is applied to make the CHB inverter provide the balanced output voltage with the fault in the system.

From Fig.1.5, the fault-tolerant control algorithm is based on the determination of the position of faulty power cells. Under this circumstance, an algorithm to detect and localize the fault is necessary which provides fault information to the CHB inverter for fault-tolerant control operation. A fault detection algorithm is to detect the fault and shut down the CHB inverter. To determine whether there is a fault in the power cells, the expected and actual voltage values should be compared. Also, fault localization algorithm provides the fault information to isolate the faulty power cell by checking the switching signals, current direction, and voltage deviation.

In this chapter, the open circuit (OC) scenarios in the CHB inverter will be discussed. Then, the principles of open-fault detection and localization will be analyzed. With the fault detection algorithm, the OC fault will be detected with the comparison between reference and actual values. Then, based on OC fault detection, the open fault can be localized with the switching states and the value of voltage deviation.

[29] analyze a FDL algorithm for CHB STATCOM using model predictive control. However, it requires sensors to detect the conduction of each power switch for fault localization, which increases the number of current sensors in the system. Also, it cannot detect all OC scenarios. [58] introduces a FDL algorithm in the CHB motor drive by calculating the DC value and the first harmonic in the load currents. However, the algorithm cannot be applied in MPC algorithm because the current distortion with MPC algorithm is small if only one switch is open in one phase. Also, the delay time between fault triggered and fault detection is large. Finally, the calculation of DC value and the first harmonic in load current is too complex in the system and difficult to realize. [59] also proposes a new FDL algorithm. However, the fault location needs to find the possible open switches and isolate all impossible OC fault locations. The algorithm is too complex for the operation of DSP and cannot provide the OC location directly as the proposed FDL algorithm in this thesis.

In this chapter, the simulation results are given to verify the feasibility of the proposed FDL algorithm. In the proposed FDL algorithm, the measured values are as Fig.6.1. The simulation shows a good performance based on MATLAB/Simulink model.

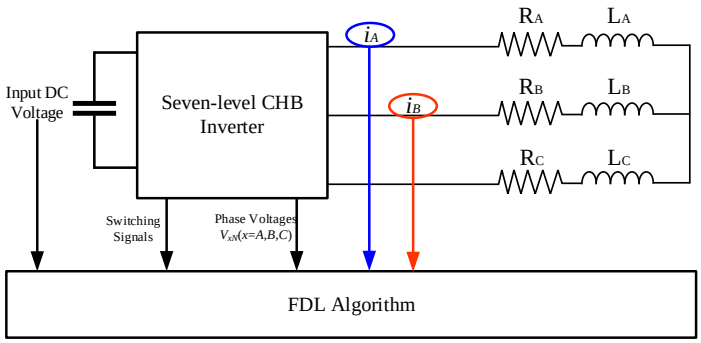

Fig.6.1 Measured Values for FDL Algorithm

In industrial application, the line-to-line voltages are measured instead of phase voltages. Under this circumstance, the common mode voltage V_{Nn} can be measured. With the line-to-line voltages and common-mode voltages, the phase voltages can be calculated and the proposed FDL algorithm can be applied in the CHB inverter.

6.2. Open Switch Fault in The H-Bridge Cell

The H-bridge inverter is shown as Fig.6.2. In this part, the healthy and open-fault conditions in power cells should be discussed and compared. For the H-bridge, the output voltage is subject to $V_{oH}=V_{dc}(S_{c1}-S_{c3})$. This value is the expected value $V_{oH\text{-}exp}$. When an open fault happens in H-bridge, the output voltage will be impacted and deviated from the expected value V_{exp} in some cases because the current will not flow through the open switch. The voltage deviation ΔV_{oH} is defined by:

$$\Delta V_{oH} = Vo - V_{oH-exp} \tag{6.1}$$

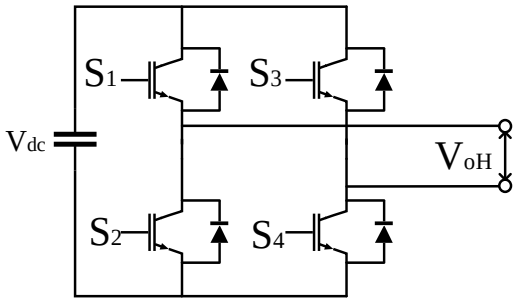

Fig.6.2 Structure of A Single-phase H-Bridge Inverter

In addition, in some cases, there is no deviation in the output voltage because of the current direction. Therefore, the method to detect the open fault is to find the voltage deviation between expected and measured output voltage.

Fig.6.3 shows the current flow comparison between healthy situation and open switch S_1 with positive output currents. The switching signals for S_1 and S_3, [S_{c1} S_{c3}], are assumed to be [1 0]. Signal 1 means the power switch is turned on and 0 means the power switch is turned off. In the healthy state, the current flows through S_1 because in this case, S_1 is turned on. The expected output voltage is V_d. However, if there is an OC fault in S_1, the current will be blocked and flow through the diode in S_1. Therefore, with the conduction of S_2, the actual output voltage is 0. With equation (6.1), the voltage deviation is V_d. With the voltage deviation, the faulty H-bridge can be found.

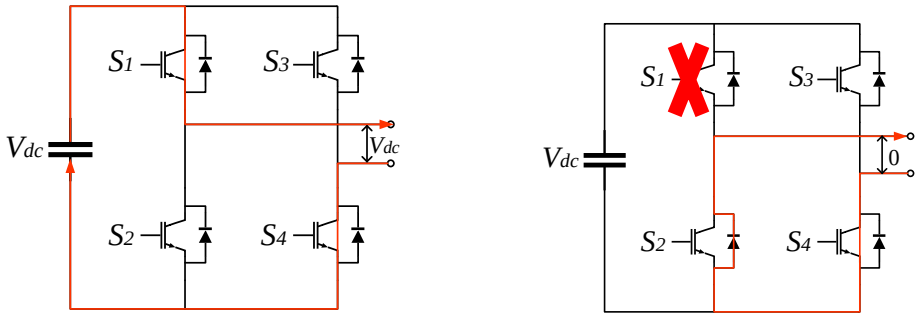

(a) All switches are healthy (b) S_1 Is Open

Fig.6.3. Comparison of Healthy and Unhealthy Situations with [S_{c1} S_{c3}] = [1 0] and Positive Current

However, there is no voltage deviation in some cases. Assuming the control signals [S_{c1} S_{c3}] is [1 1] and S_3 is open, the output voltage will not deviate from the expected value with positive current. Therefore, if the phase voltage does not deviate from expected value in one sampling time, the state is defined as unbiased state. Otherwise, when the phase voltage deviates from expected value, the state is biased.

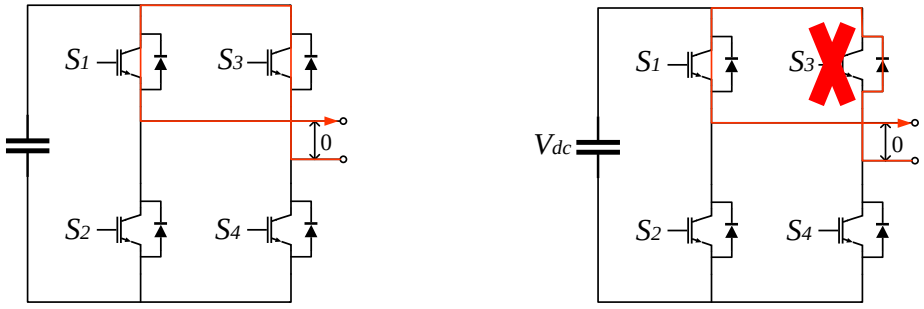

(a) All switches are Healthy (b) S_3 Is Open

Fig.6.4. Comparison of Healthy and Unhealthy Situations with [S_{c1} S_{c3}]=[1 1] and Positive Current

The effects of open fault in each switch are shown in Table.6.1[59]. It shows the output voltage deviation in single-phase H-bridge topology with positive and negative currents under different OC scenarios. With the control signals, current direction, and voltage deviations, the OC fault can be detected.

TABLE 6.1 OUTPUT VOLTAGE DEVIATIONS UNDER VARIOUS OPEN-CIRCUIT FAULT CONDITIONS IN EACH POWER CELL

Fault Location	Current Direction	Control Signals [S_{c1} S_{c3}]			
		[0 0]	[0 1]	[1 0]	[1 1]
S_1	$i > 0$	0	0	V_{dc}	V_{dc}
	$i < 0$	0	0	0	0
S_2	$i > 0$	0	0	0	0
	$i < 0$	$-V_{dc}$	$-V_{dc}$	0	0
S_3	$i > 0$	0	0	0	0
	$i < 0$	0	$-V_{dc}$	0	$-V_{dc}$
S_4	$i > 0$	V_{dc}	0	V_{dc}	0
	$i < 0$	0	0	0	0

From Table 6.1, if S_1 and S_4 are open, the output voltage will deviate from the expected value only when the current is positive. In addition, if S_2 and S_3 are open, the voltage deviation can be detected only when the current is negative. Therefore, to observe the open fault in the single-phase H-bridge inverter, the switches are categorized into two groups, [S_1 S_4] and [S_2 S_3]. The output voltage for H-bridge is sinusoidal, it means all OC fault cases can be determined during positive and negative cycles.

In a single phase CHB inverter, there are three power cells and voltage deviation for each phase is the summation of voltage deviation in each H-bridge as shown in (6.2):

$$\Delta V_{xN} = \Delta V_{oH1} + \Delta V_{oH2} + \Delta V_{oH3} (x = A, B, C) \tag{6.2}$$

From Table.6.1, if the current is positive, voltage deviations in all H-bridge inverters are positive or 0 in all fault cases. Also, voltage deviations in power cells are negative or 0 in all OC fault scenarios with negative output currents. It means the direction of voltage deviations in all power cells are the same (All positive or negative). From equation (6.2), the voltage deviation in phase voltage will be positive under positive load currents or be negative under negative load currents.

The next section analyzes the principle of fault detection and localization by the voltage deviation, current direction, and switching signals.

6.3. Fault Detection Scheme

From section.6.2, it can be concluded that to detect the open fault switch, the load current should flow through the healthy switch and the phase voltage V_{xN} (x=A, B, and C) will deviate from the desired value. From Table.6.1, the voltage deviation is positive when S_1 and S_4 are open in one power cell under positive load current. Also, the voltage deviation is negative with a negative output current if S_2 and S_3 are open. Although in some cases there is no voltage deviation because the current flows through the diode of the faulty switch, the voltage deviation in the phase voltage V_{xN} must happen if OC fault appears in the system with the control of the CHB motor drive. In Fig.6.5(a), it can be found that when an open switch fault happens in S_{11} at t=0.05s, the maximum voltage in the positive cycle cannot reach $3V_{dc}$. It means the voltage deviation happens in the waveforms of output voltages with OC fault in the power switches although there are some unbiased states in the control.

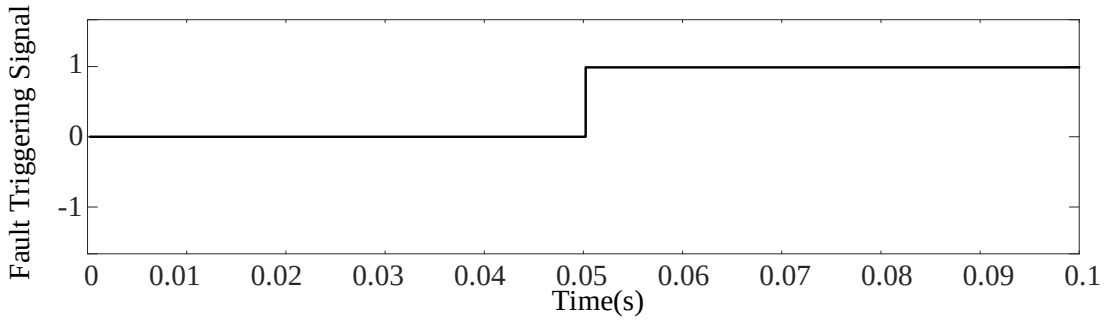

(a) OC Fault Signal

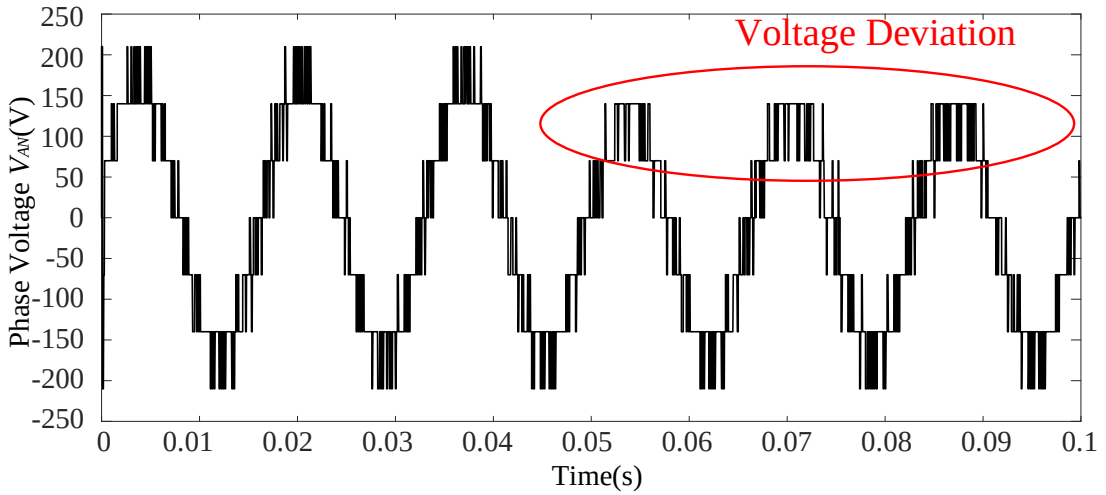

(b) Phase Voltage V_{AN}

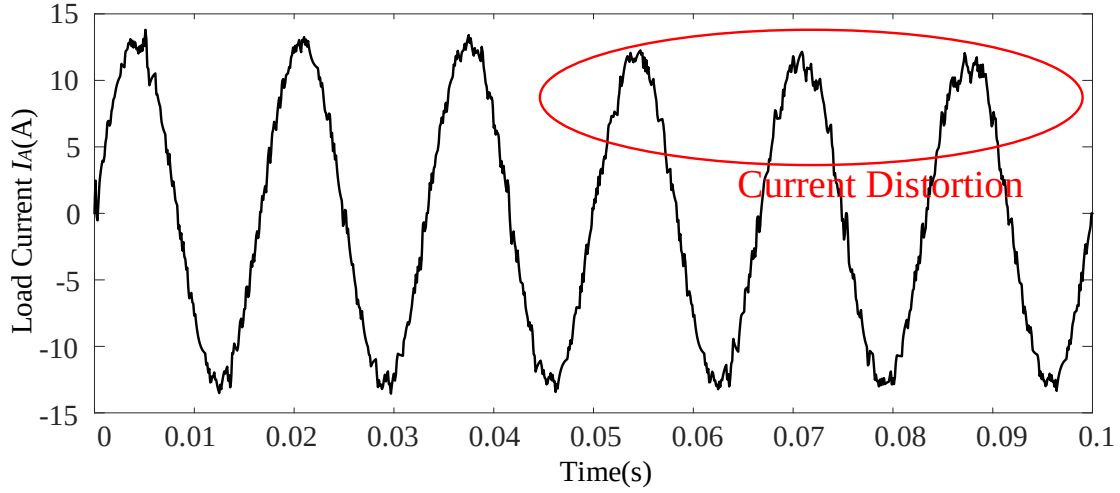

(c) Phase Current I_A

Fig.6.5. Waveform of Phase Voltage and Output Current with an Open Fault in S_{11}

In addition, the distortion of phase voltage leads to the output current distortion. From Fig.6.4(c), with an open fault appearing in S_{11}, the output current will distort from the reference value at t=0.05. However, the current distortion with M^{2}PC algorithm is small. Therefore, the method to detect and localize the open switches is by measuring the phase voltages.

Therefore, to detect the OC fault, only voltage deviation should be measured. The measured voltage deviation should be compared with the threshold value ε_V. For the healthy state, the voltage deviation ΔV_{xN} should be zero theoretically. If the absolute value of voltage deviation is smaller than the threshold value as (6.1), it means there is no open fault in the system. Otherwise, the signal for fault detection is triggered.

$$\Delta V_{xN} = V_{xN} - V_{xN-exp} \tag{6.1}$$

where $V_{xN\text{-}exp}$ and V_{xN} are desired and measured phase voltage values. The value of $V_{xN\text{-}exp}$ is calculated by (2.4). The threshold value in this simulation is set to $0.2V_{dc}$ to allow for the measurement noise. The flow chart of the proposed fault detection algorithm is as Fig.6.6.

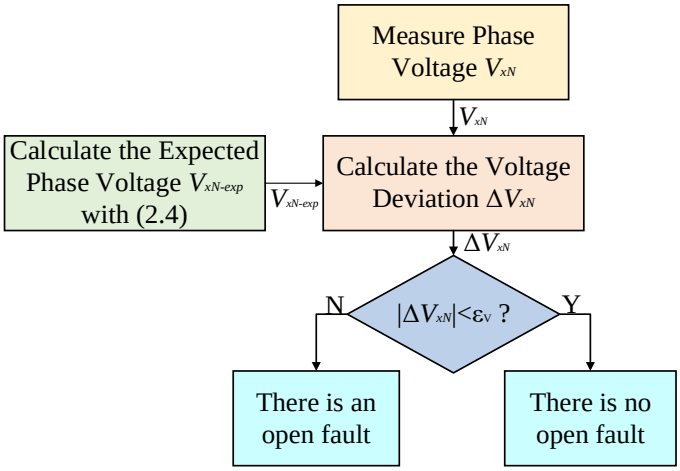

Fig.6.6 Flow Chart of Fault Detection Algorithm

With the fault detection algorithm, the OC fault in the CHB converter can be detected. Then, another important part is to localize the open fault in the CHB topology and isolate it for fault-tolerant control. In the next section, the algorithm for fault localization in CHB motor drive will be introduced.

6.4. Fault Localization Scheme

In the fault-tolerant control, the faulty power cell should be isolated. In this situation, there is a need to localize the open switch and affected power cell. Hence, to find the fault location, a fault localization matrix variable for the CHB inverter should be defined as F_x(x=A,B, and C) which in this case considered three power cell in each phase:

$$F_x = \begin{pmatrix} f_{11} & f_{12} & f_{13} & f_{14} \\ f_{21} & f_{22} & f_{23} & f_{24} \\ f_{31} & f_{32} & f_{33} & f_{34} \end{pmatrix} \tag{6.4}$$

This matrix represents the open situations of power switches in each phase and f_{ij} relates to the open situation in each IGBT. f_{ij} represents the fault localization variable for j^{th} switch in the i^{th} power cell. In the definition, if f_{ij} is 0, it means the power switch is healthy. Otherwise, there is an open fault in the corresponding switch if f_{ij} is 1.

According to Table.6.1, the voltage deviation with various switching signals under different fault scenarios. If S_1 or S_4 is open, the phase voltage deviates from reference value under positive currents. Also, the phase voltage deviates from reference value under negative currents when S_2 or S_3 is open. Therefore, fault localization for [S_1 S_4] and [S_2 S_3] should be analyzed separately. The switches can be grouped into two sets, S_{G1} and S_{G2}:

$$S_{G1} = S_{11}, S_{14}, S_{21}, S_{24}, S_{31}, S_{34}$$

$$S_{G2} = S_{12}, S_{13}, S_{22}, S_{23}, S_{32}, S_{33} \quad (6.5)$$

Section 6.4.1 introduces the fault switch identification with some fault cases by measuring the unbiased states. However, some special fault situations cannot be localized with the given fault localization algorithm. Therefore, another method which injects a control signal is introduced in Section 6.4.2.

6.4.1 Fault Switch Identification

The proposed fault localization works when the fault switch is detected. To localize the open faults, the control signals should be measured. The set of control signals is defined as S_c. S_{cij} represents the control signal for j^{th} switch in i^{th} cell.

$$S_c = [S_{c11} \quad S_{c13} \quad S_{c21} \quad S_{c23} \quad S_{c31} \quad S_{c33}] \quad (6.6)$$

Considering the situation that only phase voltage can be measured, it is impossible to localize the open switch when the phase voltage is detected to deviate from expected value. The reason is that it is difficult to distinguish which power cell generates the voltage deviation when only the sum of output voltage in all power cells is available. For instance, we assume a case that the voltage deviation is V_{dc} with positive current and S_c=[1 1 1 1 1 1]. In this case, there are three possibilities depending on Table.6.1: (1) S_{11} is open (2) S_{21} is open (3) S_{31} is open. However, it is impossible to know which power cell has the voltage deviation because only the phase voltage is measured. Therefore, we cannot exclude the healthy power cell and localize open switch with biased state. For this reason, the unbiased state is important for fault localization. In this state, there is no voltage deviation even if the OC fault is detected. Assuming that S_1 or S_4 in a power cell is open, there is voltage deviation in the output voltage with [S_{c1} S_{c3}] =[1 0] depending on Table.6.1. If there is no

voltage deviation, it means that the power cell is healthy. Therefore, the method is to use some special switching signals to exclude the healthy power cells and localize the OC fault. For instance, the output phase voltage is unbiased with the control signals S_c=[0 0 1 0 1 0] with the positive load current. In this case, the control signals for the second and third power cells are [1 0]. The two power cells are healthy because there is no voltage deviation. For the first power cell, voltage deviation should be measured if S_{14} is open from Table.6.1. Therefore, the open switch, S_{11} is localized with this method.

To localize the open fault, the first step is to detect the voltage deviation in one sampling time. The current direction is an important component for fault localization. Positive current is to localize open fault in S_1 or S_4 and negative current is to localize open fault in S_2 or S_3. Also, some special control signals for power switches should be observed and they are defined as judging control signals, S_{cj}. Then, the healthy power cells are excluded and the OC switch S_o is localized with the corresponding control signals S_{cj} and unbiased phase voltage. With the corresponding judging control signals S_{cj} and unbiased state in one sampling time, the OC switch can be determined. The flow chart of the proposed fault localization algorithm is as Fig.6.7. The relationship between S_o and S_{cj} with positive load current is shown in Table 6.2.

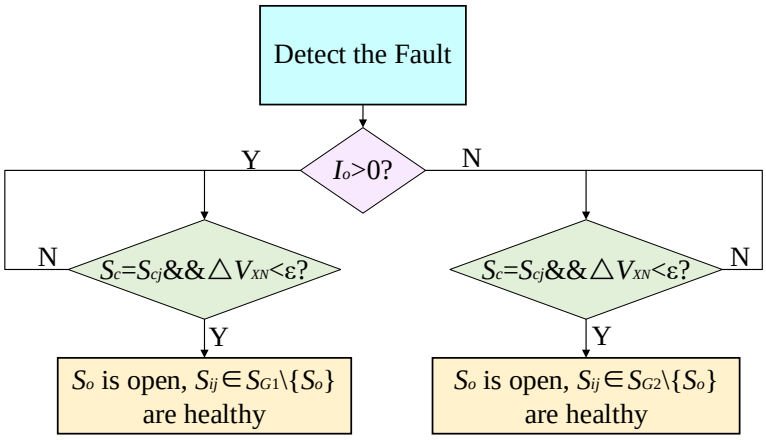

Fig.6.7. The Flow Chart of Fault Localization under Common OC Situations

TABLE 6.2 RELATIONSHIP BETWEEN FAULT LOCATION AND JUDGING CONTROL SIGNALS (POSITIVE CURRENT)

S_o	S_{cj}	S_o	S_{cj}
S_{11}	[0 0 1 0 1 0]	S_{11},S_{24}	[0 0 1 1 1 0]
S_{14}	[1 1 1 0 1 0]	S_{14},S_{21}	[1 1 0 0 1 0]
S_{21}	[1 0 0 0 1 0]	S_{11},S_{34}	[0 0 1 0 1 1]
S_{24}	[1 0 1 1 1 0]	S_{14},S_{31}	[1 1 1 0 0 0]
S_{31}	[1 0 1 0 0 0]	S_{21},S_{34}	[1 0 0 0 1 1]
S_{34}	[1 0 1 0 1 1]	S_{24},S_{31}	[1 0 1 1 0 0]

With the proposed fault localization algorithm, OC switches can be localized under the OC scenarios in Table.6.2. In all common open cases, the judging control signals to provide the unbiased state to exclude healthy power cells can be generated with phase-shifted modulation. For instance, if S_{11} is open, the judging control signal [0 0 1 0 1 0] will provide the unbiased state and exclude the second and third healthy power cells. The common cases includes two situations: (1) only one power switch is open (such as S_{11} is open) (2) the power switches in different positions of different power cells are open(such as S_{11} are S_{24} open).

However, there are some special open cases that cannot be determined because there is no unbiased state in these cases. Therefore, the fault localization algorithm should be improved to determine the special OC cases.

6.4.2 Fault Localization under Special Open Switch Scenarios

In the former section, the fault localization algorithm under common cases is discussed. However, in two OC fault situations, the given fault localization algorithm does not work because there is no unbiased state in the two special cases. The two situations are as given. Therefore, the improvement aimed at the special cases is introduced and the fault localization algorithm is updated.

***Case* 1**: Two switches in the same set in one power cell are open (such as S_{11} and S_{14} are open).

***Case* 2**: Switches in the same position of different power cells are open (such as S_{11} and S_{21} are open).

In the first case, the output voltage in the power cell will deviate from expected value in all switching signals with positive current. Therefore, there is no unbiased state if the two power switches, S_{11} and S_{14}, are open simultaneously. For the second Case, the judging control signal, S_{cj}, to localize S_{11} and S_{21} is [0 0 0 0 1 0]. The judging signal does not exist with phase-shifting modulation in M^2PC algorithm.

One method to solve this problem in the thesis is to inject some control signals for power switches. The injected control signals can provide the unbiased states to verify the two special cases. Before the injection of the control signals, the first step is to verify the existence of the two faulty cases. In the first Case, the output voltage of one power cell

deviates from expected value with the input control signal [0 0], [1 0], and [1 1] according to Table.6.1. In the second Case, with two power switches open, the possibility of voltage deviation is high. Therefore, the thesis assumes that if the voltage deviation is measured in consecutive sampling times, the two Cases are likely to appear. Then, the control signals to provide the desired states can be injected in the next several time intervals. The two requirements for injecting control signals are: (1) detect the open fault (2) find the voltage deviation in some consecutive sampling times.

The desired control signals should be injected in sequence. With each set of control signals, if the corresponding voltage deviation is measured, open switches can be localized in the two cases. For the first Case, if the desired voltage deviation is measured with the corresponding injected control signals, the open switches can be localized. For the second Case, if the unbiased state is measured with the injected control signals, the open switches can be determined as section 6.4.1. The flow charts of fault localization algorithm under the two Cases with positive load current are as Fig.6.8.

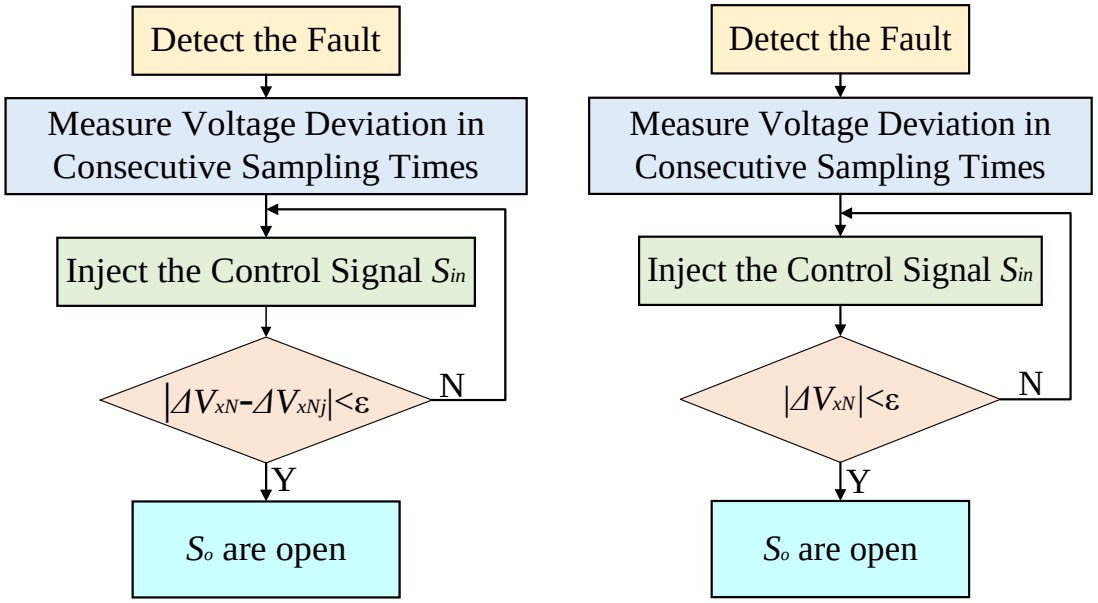

(a) Case 1 (b) Case 2

Fig.6.8. The Flow Chart of Fault Localization Algorithms

where S_{in} is the injected control signals in one phase. S_o is the open switch. ΔV_{xNj} is the judging voltage deviation values with S_{in} in Case 1. The relationship of S_o, S_{in} and ΔV_{xNj} for the first Case under the positive current are shown in Table.6.3. The relationship of S_o, S_{in} for the second Case under the positive current are in Table.6.4.

TABLE 6.3 RELATIONSHIP OF FAULT LOCATION, INJECTED CONTROL SIGNALS AND JUDGING VOLTAGE DEVIATION IN SITUATUION 1 (POSITIVE CURRENT)

S_o	S_{in}	ΔV_{xNj}
S_{11},S_{14}	[1 0 0 1 0 1]	$2V_{dc}$
S_{21},S_{24}	[0 1 1 0 0 1]	$2V_{dc}$
S_{31},S_{34}	[0 1 0 1 1 0]	$2V_{dc}$

TABLE 6.4 RELATIONSHIP OF FAULT LOCATION AND INJECTED CONTROL SIGNALS IN SITUATUION 2 (POSITIVE CURRENT)

S_o	S_{in}	S_o	S_{in}
S_{11},S_{21}	[0 0 0 0 1 0]	S_{14},S_{34}	[1 1 1 0 1 1]
S_{14},S_{24}	[1 1 1 1 1 0]	S_{21},S_{31}	[1 0 0 0 0 0]
S_{11},S_{31}	[0 0 1 0 0 0]	S_{24},S_{34}	[1 0 1 1 1 1]

For instance, if S_{11} and S_{14} are open, with the injected control signal S_c=[1 0 0 1 0 1] under positive current, the phase voltage deviation will be $2V_{dc}$. The voltage deviation with only S_{11} or S_{14} open is V_{dc}. If the judging voltage deviation is detected, the open switches, S_{11} and S_{14}, can be verified. For the second Case, Also, if S_{11} and S_{21} are open, the desired judging control signal is [0 0 0 0 1 0]. With the injection of this control signal, the open switches, S_{11} and S_{21}, can be determined with an unbiased state as section.6.3.1.

With the injection of judging signals, the two special fault scenarios can be verified. Therefore, open switches can be detected and localized with the improved FDL algorithm in all cases. The simulation results of FDL algorithm are as Section.6.4.

6.5. Simulation Studies of FDL Algorithm

To validate the FDL algorithm based on M^{2}PC algorithm, a seven-level CHB inverter topology is built in MATLAB/Simulink. The simulation results of M^{2}PC algorithm is provided in Chapter 4. Based on M^{2}PC algorithm, the simulation of the proposed FDL algorithm is given in this section. Several different OC fault scenarios are simulated by disabling the control signals. Also, the RMS value of load currents is set to 9A and RL load is used in the simulation studies.

In section.6.5.1, the simulation results of FDL algorithm based on common cases are provided. The two common cases are simulated in section.6.4.1： (1) S_{11} is open (2) S_{11} and S_{24} are open. The performance of FDL algorithm under special cases is provided in section.6.5.2. The simulation includes two cases: (1) S_{11} and S_{14} are open (2) S_{11} and S_{21} are open. In all simulations, the OC fault is detected in the system when the fault detection signal turns to 1.

6.5.1 FDL Algorithm under Common Cases

From Table.6.2, the relationship of open switches and judging signals under common cases is discussed. The first step is to detect the OC fault in the system by comparing the measured and desired phase voltages. In all common cases of open fault, if the unbiased state is measured with the corresponding judging signals, the open switch can be localized with Table.6.2. In this part, simulation results validate the feasibility of the proposed FDL algorithm under common cases.

In the first case, the switch, S_{11}, is assumed to be open at t=0.05s. The figures of load currents, fault detection signal, and fault localization signals are provided in Fig. 6.9. From this figure, the fault detection and localization signals are triggered in a short time with only S_{11} open. From the simulation, f_{11} turns to 1 which means the OC fault is detected and localized in S_{11} with the measured unbiased state.

In the second case, the switches, S_{11} and S_{24}, are assumed to be turned off at t=0.05s. The figures of load currents, fault detection signal, and fault localization signals are provided as Fig. 6.10. In the simulation, the fault signals of f_{11} and f_{24} turn to 1 and it means the OC faults are detected and localized in S_{11} and S_{24} with the unbiased state.

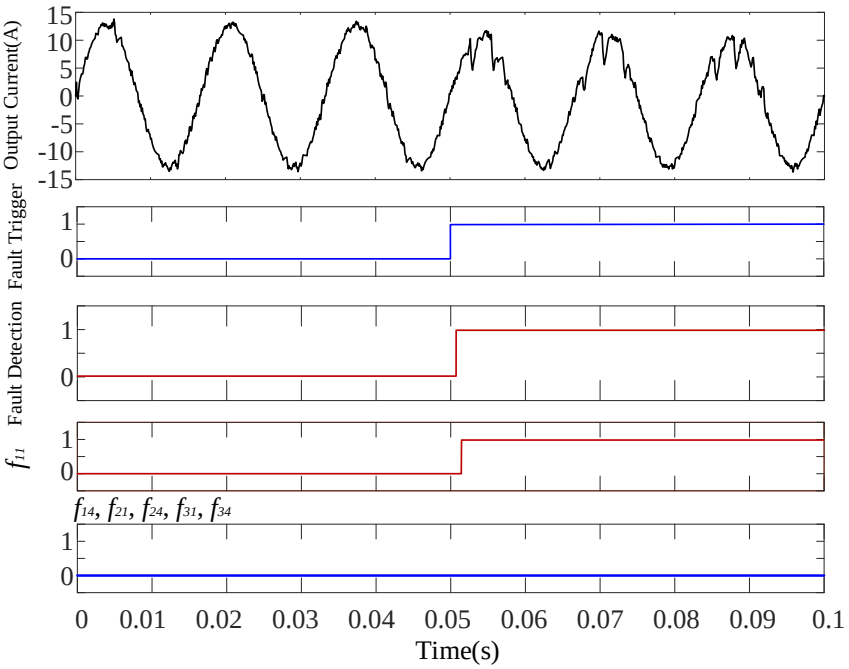

Fig.6.9. Simulation Results of FDL Algorithm with S_{11} open

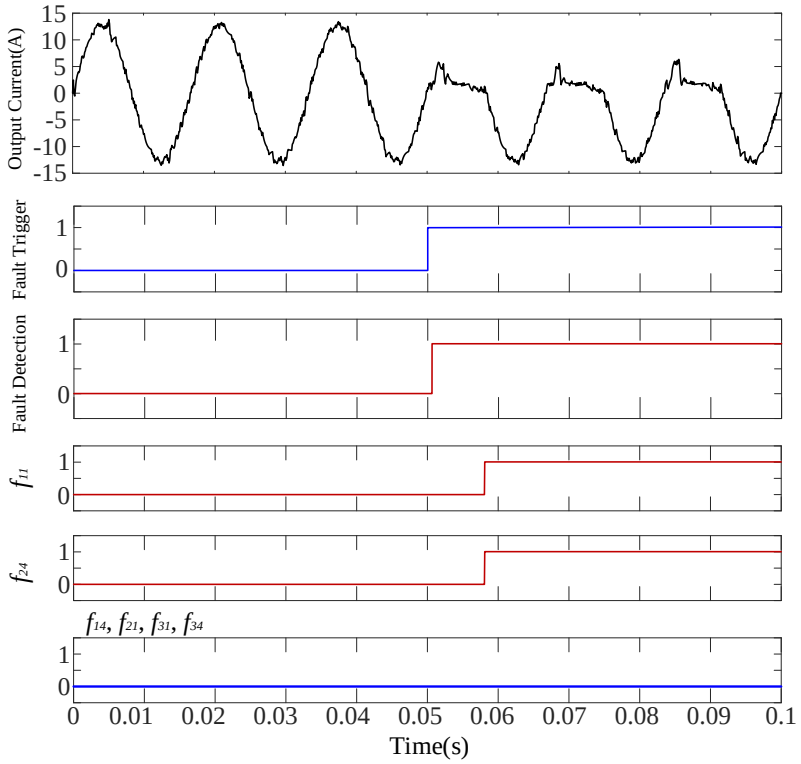

Fig.6.10. Simulation Results of FDL Algorithm with S_{11} and S_{24} open

From the simulation results, the FDL algorithm performs well under the two common cases. The OC fault can be detected with the measured phase voltage deviation and localized with the unbiased state and corresponding switching signals. Therefore, the FDL algorithm works in all other common cases. With Table.6.2, the FDL algorithm can detect the OC fault in the system and localize the OC switches.

6.5.2 FDL Algorithm under Special Cases

In this section, the special OC cases will be discussed. Because there is no unbiased state in these cases, some control signals should be injected to generate the state in need to localize the OC switches.

In the simulation, there are two special cases. Fig.6.11 shows the simulation result with S_{11} and S_{14} are open. The injected control signal for the phase is [1 0 0 1 0 1] and the judging voltage deviation ΔV_{xNj} is $2V_{\mathrm{dc}}$. The open faults are detected and localized in S_{11} and S_{14}.

In addition, Fig. 6.12 shows the simulation results with S_{11} and S_{21} are open. The injected judging switching signal is [0 0 0 0 1 0]. With this judging switching signal, if the unbiased state is measured, it means S_{11} and S_{21} are open. Therefore, open faults in the system are detected and localized in these cases.

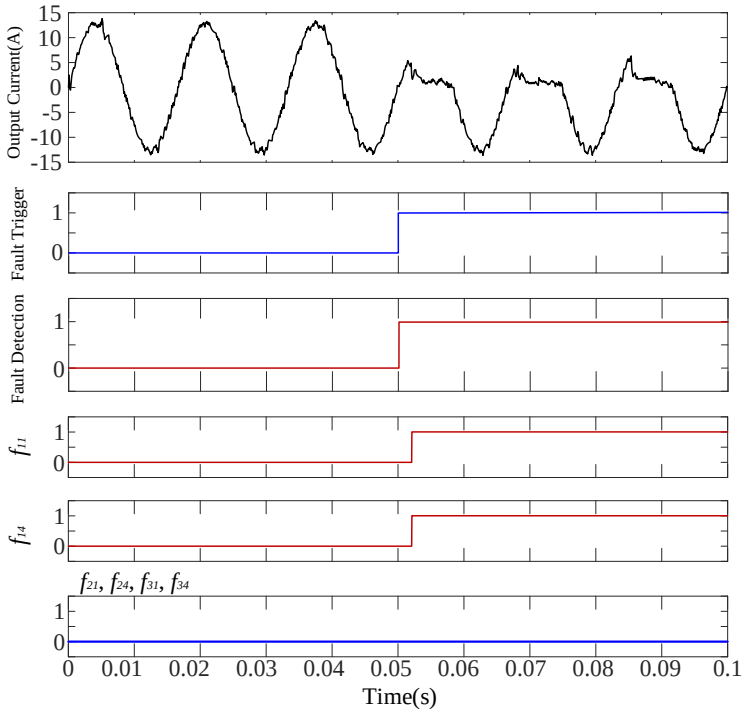

Fig.6.11. Simulation Results of FDL Algorithm with S_{11} and S_{14} open

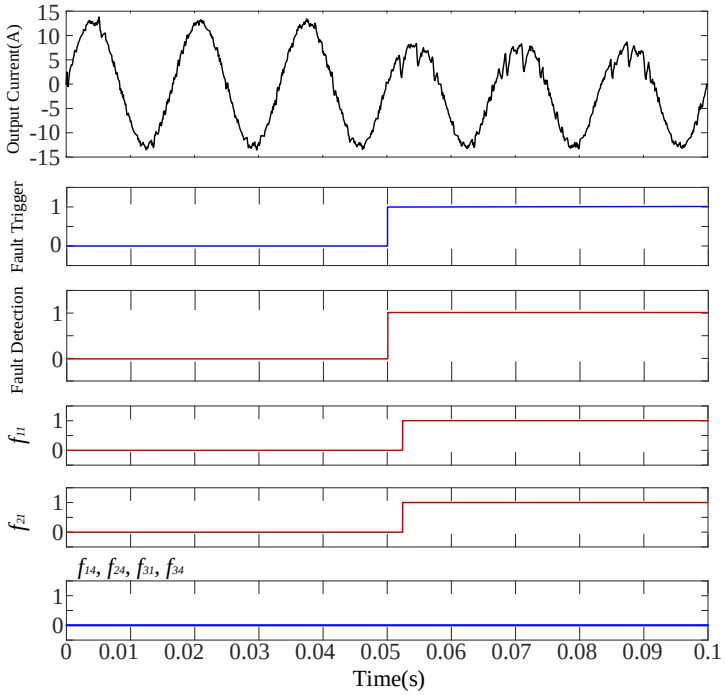

Fig.6.12. Simulation Results of FDL Algorithm with S_{11} and S_{21} open

From the two cases, the improved FDL algorithm performs well with the injection of judging control signals. Therefore, the FDL algorithm can be used to localize the open switches under special cases.

6.6. Summary

In this section, the FDL algorithm based on M^2PC algorithm is introduced. To detect the OC fault in the CHB inverter, the voltage deviation between measured and expected phase voltages should be calculated. If the voltage deviation is calculated, it means the OC fault must exist in the system. With the OC fault detected, the fault localization algorithm is used to find the fault locations under common and special cases by measuring the current direction, voltage deviation, and switching signals. From the simulation results, the open fault in the CHB inverter can be detected and open switches can be localized in all OC cases with the proposed FDL algorithm.

Chapter 7

Hardware Platform and Experimental Results

7.1. The Implementation of CHB Topology

The hardware setup of a 7-level CHB inverter with RL load is employed to verify the simulation results experimentally. For the construction of CHB inverter, there are three power cells in each phase. To make the experiment simple, the six-switch non-regenerative CHB power cells are selected in the experiments. The DC voltage in each power cell is provided with a six-pulse diode rectifier fed by a phase-shifting transformer. The overall structure of the CHB platform is shown in Fig.7.1.

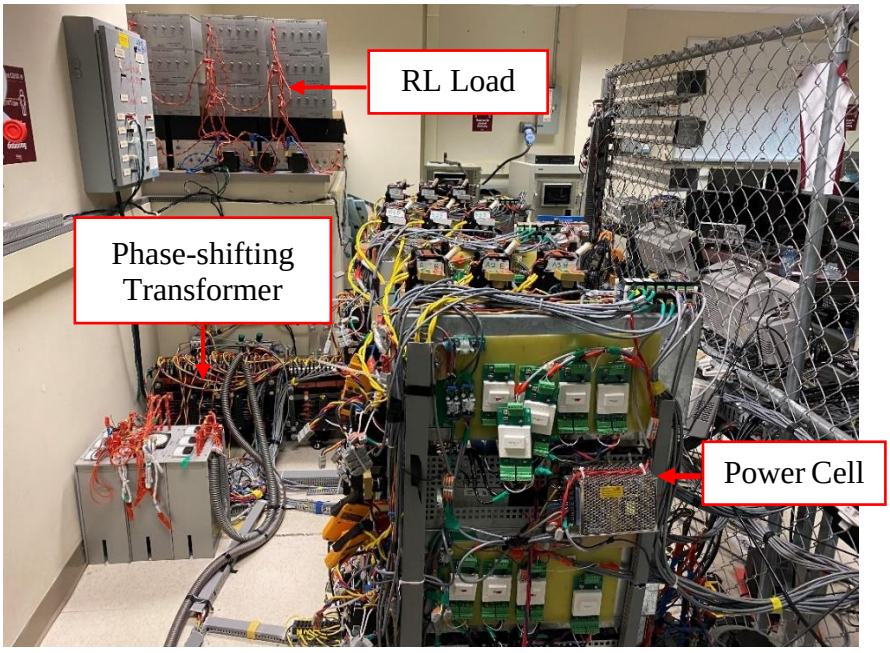

Fig.7.1. The CHB Hardware Setup

In the hardware setup, there are four different sections as follows:

1) **Grid-connected Circuits:** The circuits are connected to the grid directly to provide the three-phase AC voltages, including transformers and grid filter.

2) **Power Cells:** The structure is as Fig.1.4. Each power cell has a three-phase diode rectifier, DC capacitor, and single-phase H-bridge inverter.

3) **Controllers and Measurement Circuits:** This part provides the control signals for IGBTs in each power cell. Gate drivers are used to amplify the voltage signals to control the switches. The measurement circuits for voltages and currents are used for the control in the motor drive.

4) **Load:** RL load is selected at the output of the CHB inverter.

7.1.1 Grid-Connected Circuits

The connection between the grid and the power cell is realized by a phase-shifting transformer as Fig.7.2.

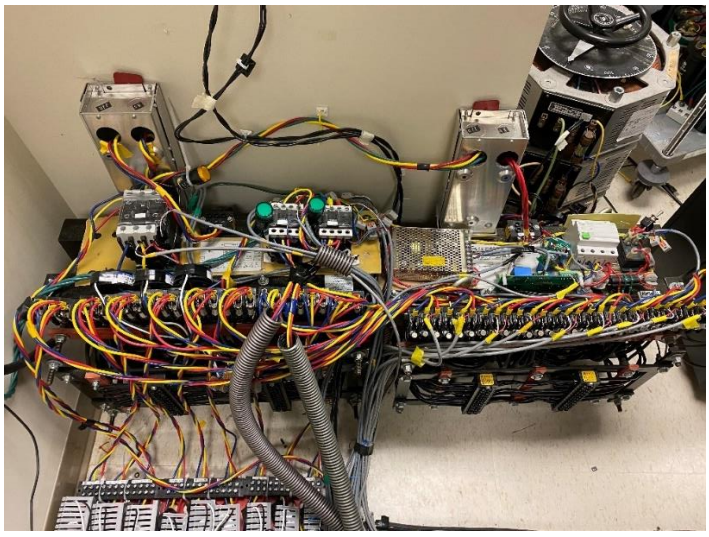

Fig.7.2. The Grid-connected Circuit

The primary side is connected to the bus line and the seconding side is connected to three-phase rectifier. With the grid-connected circuits, the DC capacitor is charged to the desired value for the control of power cells.

7.1.2 Power Cells

The details of power cells in the experiments are as shown in Fig.7.3. The three-phase diode rectifier utilizes six IGBTs to obtain the DC voltage for the capacitor. With the DC capacitor, the output inverter can produce the two-level voltage waveforms with the implementation of two half-bridge IGBT modules. With the series connection of all H-bridges in one phase, the CHB inverter can generate seven-level waveforms. Gate drivers are used to amplify the control signals for AFE and H-bridge inverters.

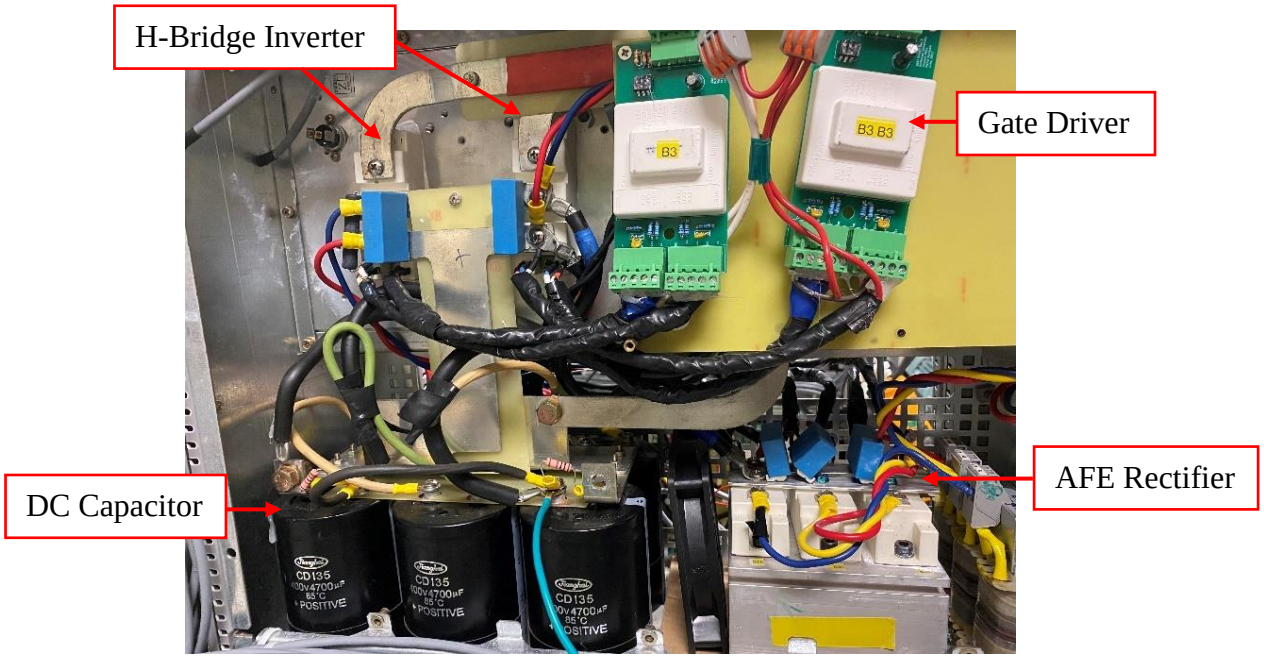

Fig.7.3. The Structure of Power Cell

7.1.3 Controller and Measurement Circuits

To implement the control algorithm, the dSpace MicroLabBox controller is programmed to provide the control signals for IGBTs in the CHB motor drive to produce the desired output currents. In addition, for the M^2PC and M^2FPC algorithm, the load currents should be measured in the control module. The phase voltages, DC capacitor voltages, and three-phase grid currents should be monitored to ensure the system operate normally. Therefore, the measurement circuits are also necessary in the platform. The dSpace MicroLabBox controller and measurement circuits are shown in Fig.7.4.

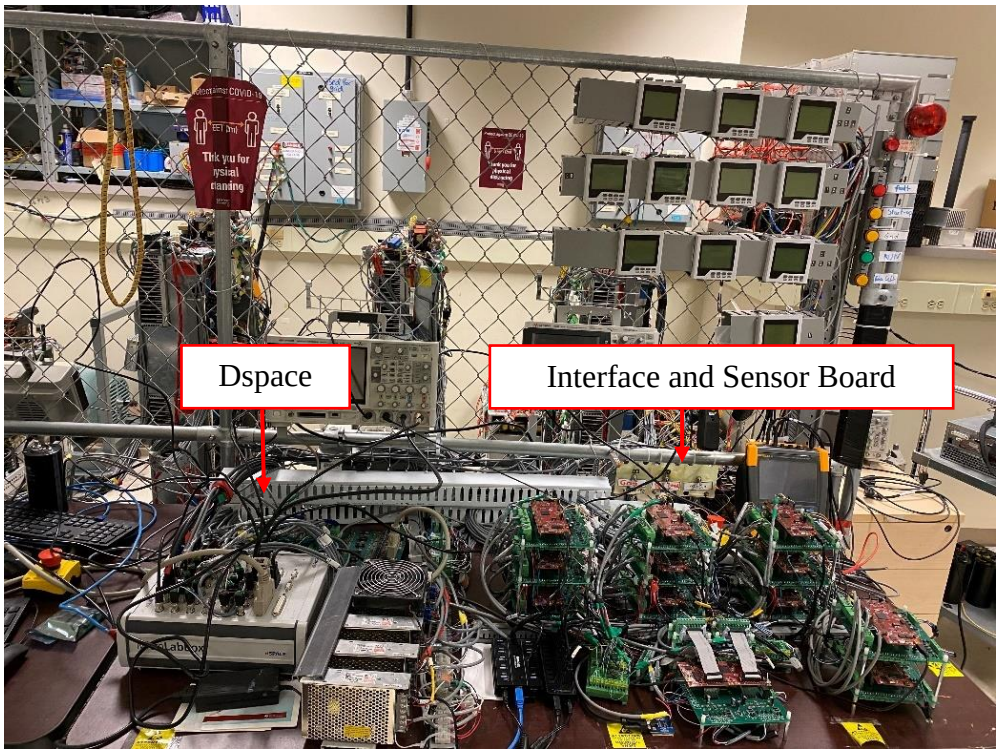

Fig.7.4. The Structure of Controllers and Measurement Circuit

7.1.4 RL Load

For all experiments, the RL load is selected. The load inductance is 5mH and the load resistance is 13Ω. Therefore, the resistors are connected in parallel and the single-phase inductor is connected to the resistor bank in serious.

7.2. Experimental Validation of Modulated Model Predictive Control in a Seven-level CHB Inverter

The CHB setup is used to verify the theoretical and simulation studies. For the modulated model predictive control in the hardware platform, the DC capacitor voltages are fixed to 70V. The DC-link capacitance is 2.3mF. The waveforms of output currents and phase voltage with M^{2}PC algorithm are shown in Fig.7.5 and Fig.7.6 respectively. In this experiment, the RMS value of load current is set to 9A. In the experiment, the THD value of load currents is 3.27%.

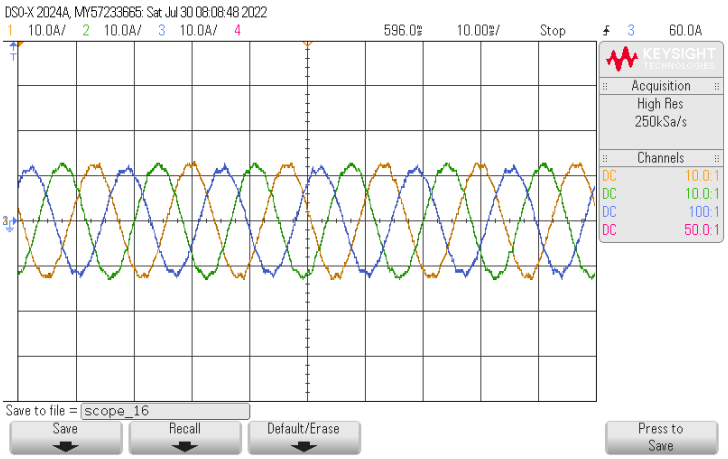

Fig.7.5. Waveforms of Load Currents in Three Phases(I_x)

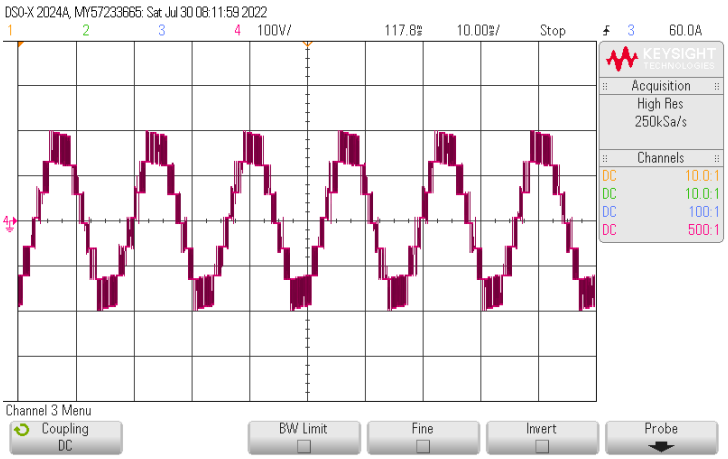

Fig.7.6. Waveform of Output Phase Voltage(V_{AN})

From the experimental results, the M^{2}PC algorithm performs well under steady state condition. Also, to evaluate the dynamic performances of M^{2}PC algorithm load change and frequency change are shown in Fig.7.7 and Fig.7.8. These figures show the output currents under amplitude and frequency changes. In the amplitude change, the RMS value of load currents increases from 6A to 9A. In the frequency change, the operation frequency decreases from 60Hz to 10Hz.

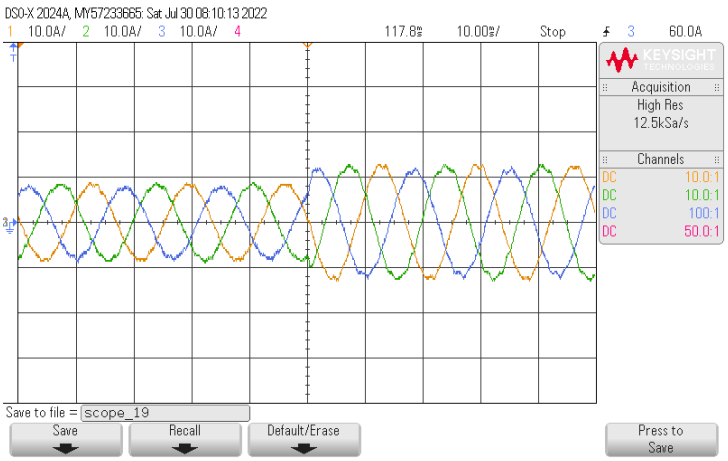

Fig.7.7. Waveforms of Load Currents under Amplitude Change

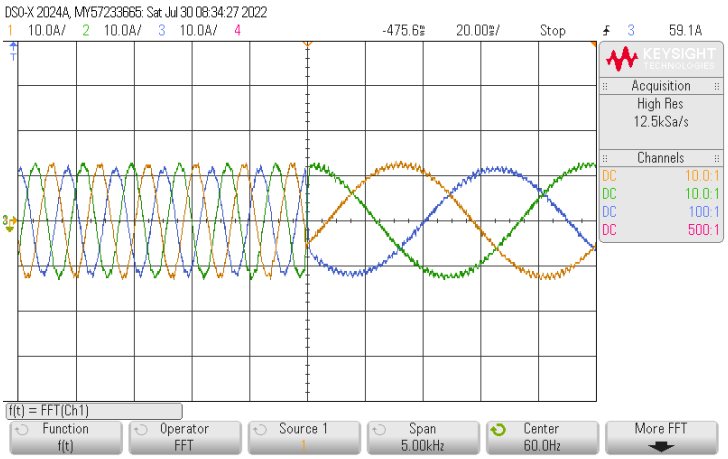

Fig.7.8. Waveforms of Load Currents under Frequency Change

From the experiments under steady-state and dynamic performances, M^{2}PC algorithm performs well in the control of output currents. It means M^{2}PC algorithm inherits all advantages of conventional MPC. In the control module, only nine voltage vectors need to be calculated, which reduces the computation burden compared with the conventional MPC which evaluate 127 different voltage vectors. In addition, with the application of phase-shifted modulation to produce the control signals, the switching frequency of output currents is fixed to 900Hz compared to variable value with conventional switching frequency. The fixed switching frequency makes the waveform quality better and is convenient for filter design.

7.3. Experimental Validation of Modulated Model-free Predictive Control

Also, the CHB platform is used for the experimental validation of M^{2}FPC algorithm. The load resistance and inductance are 13Ω and 5mH respectively. The DC voltage for each capacitor is 70V. In the steady-state performance, the waveforms of load currents are

shown in Fig.7.9. In the simulation, M^{2}FPC algorithm works well under steady-state performance. The THD value of load currents is 4.62%.

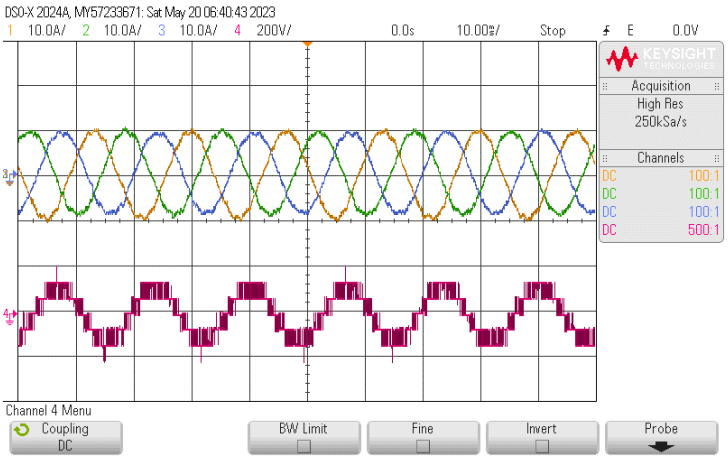

Fig.7.9. The Waveforms of Load Currents And Phase Voltage with M^{2}FPC Algorithm under Steady-state Performance

In addition, the dynamic performance of M^{2}FPC algorithm is validated with the experiments. The performances of amplitude and frequency changes are as Fig.7.10 and 7.11. In the amplitude change, the RMS value of load currents increases from 6A to 8A. In the frequency change, the operation frequency of load currents decreases from 60Hz to 10Hz. The M^{2}FPC algorithm works also well under dynamic performances from experimental results.

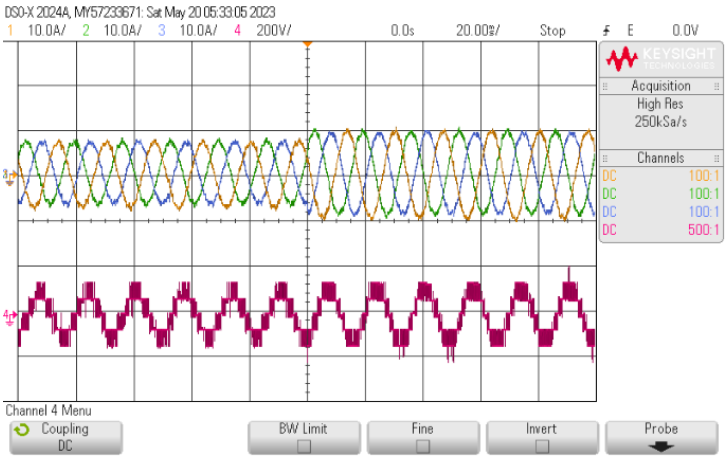

Fig.7.10. The Waveforms of Load Currents And Phase Voltage with M^{2}FPC Algorithm under Amplitude Change

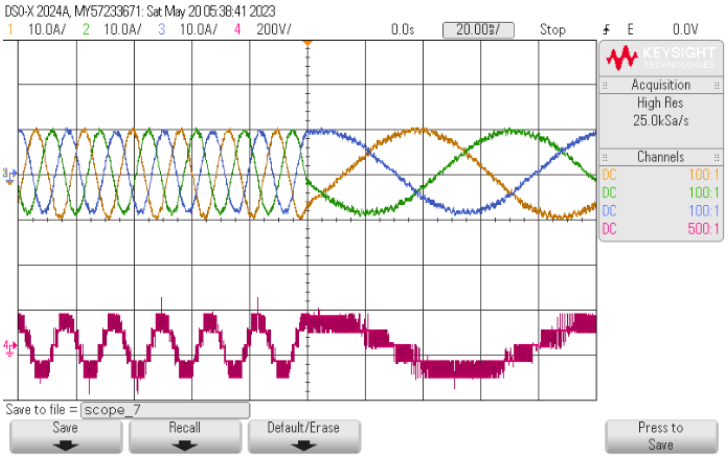

Fig.7.11. The Waveforms of Load Currents And Phase Voltage with M^{2}FPC Algorithm under Frequency Change

Finally, the comparison of M^{2}PC and M^{2}FPC algorithms under parameter mismatch are provided. The RMS value of load currents is 8A. The load resistance and inductance in the controller are set to $0.3R_o$ and $0.3L_o$ respectively. From the experimental results, the amplitude of load currents cannot reach reference value with M^{2}PC method, however it can reaches the reference value by M^{2}FPC method.

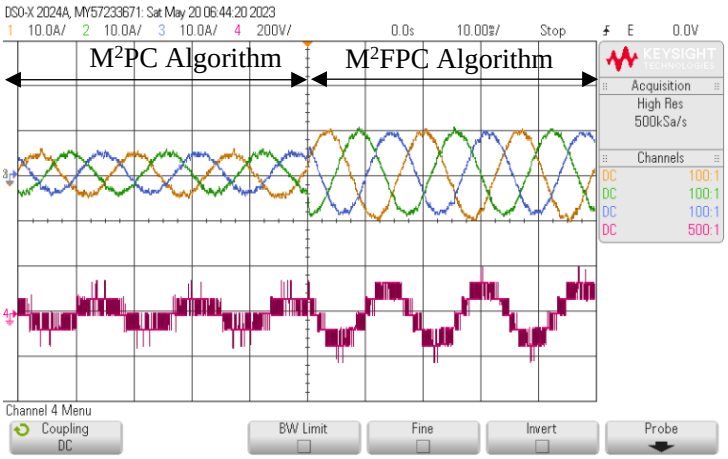

Fig.7.12. Comparison of M^{2}PC and M^{2}FPC Algorithms under Parameter Mismatch

7.4. Summary

The output currents of the seven-level CHB inverter are controlled with the M^{2}FPC algorithm. The experimental results validate the operations of M^{2}FPC algorithm. The RLS estimator to estimate the coefficients of ARX model can be used to replace the discrete-time model of the RL load. Therefore, the algorithm reduces the dependence of given parameters and model in the experiments.

Chapter 8

Conclusion and Future Work

8.1. Conclusion

The cascaded H-bridge multilevel inverter is a state-of-the-art and an attractive multilevel inverter for medium voltage motor drive applications. The CHB structure has the advantages of modularity, scalability, and fault-tolerant capability. The grid provides the power to CHB MV drive and then diode rectifiers or AFE module generate the DC voltage in each power cell for the control of CHB inverter. The output voltage is generated with the control of IGBTs. With three power cells (which are considered in this thesis without losing the generality), the CHB drive can produce seven levels in the output voltage.

Modulation schemes are applied in the CHB inverter to produce sinusoidal output currents. In this thesis, various kinds of SPMW modulation are analyzed. With the comparison between carrier and modulation waveforms, switching signals are generated and the control of output currents is realized. To control the amplitude of output currents, the amplitude modulation index m_a can be modified.

The conventional MPC algorithm for the CHB inverter with RL and PMSM load is studied. FCS-MPC algorithm has the advantages of good dynamic performance, muti-objective control, and a good inclusion for nonlinearity and simple structure. In the FCS-MPC, the cost function is defined to find the optimal switching signals. One drawback of

conventional FCS-MPC is that the switching frequency is variable. Also, the computation burden for CHB inverter is too large.

Based on conventional the MPC scheme, the M^2PC algorithm is developed for the control of the CHB inverter to inherit the advantages of MPC and obtain the fixed switching frequency. In this algorithm, the set of voltage vector is determined with the reference and measured current. Therefore, the search step in the definition is adaptive to realize self-adjusting. With the optimal voltage vector obtained by the minimization of cost function, the amplitude modulation index can be calculated and phase-shifted modulation scheme is applied to generate control signals. In the M^2PC algorithm, only nine possible voltage vectors in α-β coordinate are calculated and the computation number is reduced.

Based on the proposed M^2PC algorithm, it still requires the accuracy of the given parameters and model. It means the if there is parameter or model mismatch, the performance of M^2PC algorithm is not good. The RLS algorithm can build the discrete-time model with observed values. The ARX model does not need the given parameters and model. Therefore, the accuracy of parameters and model will not affect the performance of M^2PC algorithm negatively.

In addition, the structure of CHB inverter is convenient for fault-tolerant control. Therefore, the fault information is necessary and FDL algorithm is introduced as well. The proposed FDL algorithm can detect the OC fault and localize the open switch by comparing the voltage deviation, current direction and switching signals. One challenge of FDL algorithm is that it is impossible to localize the open switch with biased state. Therefore, to determine the OC switches, the unbiased state is used to exclude the healthy switches

and localize the OC switches. Another challenge is that some OC scenarios cannot be detected because the desired switching states do not exist with SPWM modulation. To solve this problem, the desired switching signals should be injected to the switches directly to provide the state in need and the special OC scenarios can be detected.

The thesis introduces the proposed M^2PC algorithm, M^2FPC algorithm and M^2PC-based FDL algorithm in the seven-level CHB inverter. The simulation results are provided to verify the principles of the proposed MPC and FDL algorithms.

The hardware setup is employed by building the three-phase regenerative power cells. Experiments are done to validate the operation of the M^2PC and M^2FPC algorithms.

8.2. Contribution

The contributions of the presented work can be outlined as follows:

- A review of CHB converter has been done and corresponding modulation schemes are discussed. Also, FDL algorithms are reviewed.
- MPC algorithms are studied and performance, advantages, and drawbacks of them are reviewed.
- Modulated MPC has been proposed in the CHB motor drive and developed for a CHB inverter, and its advantages compared with the conventional MPC algorithm.
- Modulated model-free predictive control algorithm is proposed and developed for a CHB inverter. With RLS algorithm, the convergence of current prediction model is fast. It's performance under parameter mismatch is also compared with the M^2PC algorithm. In addition, the simulation and experimental results are presented to verify its feasibility.

- A new FDL algorithm to detect and localize the open switch fault in the CHB motor drive is proposed. The performance analysis and principles of the proposed FDL scheme are provided. Simulation results can validate the M^2PC-based FDL algorithm in a CHB inverter.

8.3. Future Work

The research in this thesis shows the model predictive control and FDL algorithms applied in a CHB motor drive. The further analysis and experiments of the proposed algorithms can develop a better performance of the control algorithms and fault -tolerant control in the CHB motor drive. Some future tasks are summarized as follows:

- Analysis of these control algorithms for AFE rectifier in regenerative power cells
- Fast computation of M^2FPC algorithms
- Considering the M^2FPC algorithm with the three-phase unbalanced loads
- Further research on other adaptive filter applications in the control of CHB motor drive
- Experimental Validation of FDL algorithms in CHB inverters
- Analysis and experimental validation of fault-tolerant control in the CHB motor drive along with the FDL algorithm

References

[1] S. Rizzo and N. Zargari, "Medium voltage drives: what does the future hold?," The 4th International Power Electronics and Motion Control Conference, 2004. IPEMC 2004., Xi'an, China, 2004, pp. 82-89 Vol.1.

[2] J. Rodriguez, S. Bernet, B. Wu, J. O. Pontt and S. Kouro, "Multilevel Voltage-Source-Converter Topologies for Industrial Medium-Voltage Drives," in IEEE Transactions on Industrial Electronics, vol. 54, no. 6, pp. 2930-2945, Dec. 2007,

[3] Z. Yang, J. Sun, X. Zha and Y. Tang, "Power Decoupling Control for Capacitance Reduction in Cascaded-H-Bridge-Converter-Based Regenerative Motor Drive Systems," in IEEE Transactions on Power Electronics, vol. 34, no. 1, pp. 538-549, Jan. 2019.

[4] Z. Ni, A. Abuelnaga and M. Narimani, "A Novel High-Performance Predictive Control Formulation for Multilevel Inverters," in IEEE Transactions on Power Electronics, vol. 35, no. 11, pp. 11533-11543, Nov. 2020.

[5] “Medium Voltage Drives Report - 2021”, 2021. [Online]. Available: https://omdia.tech.informa.com/-/media/tech/omdia/brochures/electric-motor-systems/1-medium-_-voltage-drives-_-report---2021.pdf. [Accessed: 19-Feb-2023]

[6] "GLOBAL MEDIUM VOLTAGE ELECTRIC DRIVES MARKET-GROWTH, TRENDS, COVID-19 IMPACT, AND FORECASTS (2023 - 2028)". [Online].

Available: https://www.mordorintelligence.com/industry-reports/global-medium-voltage-electric-drives-market [Accessed: 19- Feb- 2023].

[7] B. Wu, and M. Narimani, "High-Power Converters and AC drives ", *Wiley-IEEE Press*, 2017, ISBN: 978-1-119-15603-1.

[8] " PowerFlex 6000 Medium Voltage Variable Frequency Drive Firmware, Parameters, and Troubleshooting Manual ", 2019. [Online]. Available: https://literature.rockwellautomation.com/idc/groups/literature/documents/td/6000-td004_-en-p.pdf. [Accessed: 19- Feb- 2023].

[9] " Altivar Process ATV6000 Variable Speed Drives Handbook Manual", 2021. [Online]. Available: https://download.schneider-electric.com/files?p_enDocType=Catalog&p_File_Name=ATV6000_Handbook_Manual_EN_QGH83255_03.pdf&p_Doc_Ref=QGH83255 [Accessed: 19- Feb- 2023].

[10] "SINAMICS Perfect Harmony GH180", 2021. [Online]. Available: https://assets.new.siemens.com/siemens/assets/api/uuid:e9d52b04c5acad9232c4c701743b9ec3312a3a3e/genv-gh180-520-brochure-june2018update-lowres.pdf. [Accessed: 19- Feb- 2023].

[11] " Medium Voltage Drives T300MV2", 2021. [Online]. Available: https://www.toshiba.com/tic/datafiles/brochures/T300MV2_8pg_ESSENCE.pdf. [Accessed: 19- Feb- 2023].

[12] " Adjustable Speed Drives MTX2-60 (Extreme Outdoor)", 2019. [Online]. Available:https://www.toshiba.com/tic/datafiles/brochures/MTX2-60.pdf. [Accessed: 19- Feb- 2023].

[13] "ACS 1000 Medium Voltage Drives", 2021. [Online]. Available: https://library.e.abb.com/public/a9ba044f69174e2fae063eea07df3448/ACS1000_medium_voltage_drive_catalog_3BHT490400R0001_RevL_EN_lowres.pdf. [Accessed: 19- Feb- 2023].

[14] "Efficient use of your most valuable resources", 2022. [Online]. Available: https://www.eaton.com/content/dam/eaton/products/medium-voltage-power-distribution-control-systems/motor-control/literature/brochures/eaton-sc9000-ci-vfd-product-aid-pa020010en-en-us.pdf. [Accessed: 19- Feb- 2023].

[15] "ALSPA Drive Range", 2001. [Online]. Available: http://alsintec.com/documents/alstom/drives/alspa%20drive%20range_drives%20solutions.pdf. [Accessed: 19- Feb- 2022].

[16] S. S. Barah and S. Behera, "An Optimize Configuration of H-Bridge Multilevel Inverter," 2021 1st International Conference on Power Electronics and Energy (ICPEE), Bhubaneswar, India, 2021, pp. 1-4.

[17] M. Vijeh, M. Rezanejad, E. Samadaei and K. Bertilsson, "A General Review of Multilevel Inverters Based on Main Submodules: Structural Point of View," in IEEE Transactions on Power Electronics, vol. 34, no. 10, pp. 9479-9502, Oct. 2019.

[18] D. Kang, S. Badawi, Z. Ni, A. H. Abuelnaga, M. Narimani and N. R. Zargari, "Review of Reduced Switch-Count Power Cells for Regenerative Cascaded H-Bridge Motor Drives," in IEEE Access, vol. 10, pp. 82944-82963, 2022.

[19] R. Rao and S. Hou, "Model Predictive Control for Cascaded Multilevel Inverter Based on Lyapunov Function," *2019 IEEE Innovative Smart Grid Technologies - Asia (ISGT Asia)*, Chengdu, China, 2019, pp. 2314-2318.

[20] V. Blahnik, J. Talla, T. Kosan and Z. Peroutka, "Control of three phase 7-level CHB voltage-source active rectifier," 2015 International Conference on Applied Electronics (AE), Pilsen, Czech Republic, 2015, pp. 7-10.

[21] P. Cortés, A. Wilson, S. Kouro, J. Rodriguez and H. Abu-Rub, "Model Predictive Control of Multilevel Cascaded H-Bridge Inverters," in IEEE Transactions on Industrial Electronics, vol. 57, no. 8, pp. 2691-2699, Aug. 2010.

[22] Q. Wang, M. Rivera, J. A. Riveros and P. Wheeler, "Modulated Model Predictive Current Control for PMSM Operating With Three-level NPC Inverter," 2019 IEEE 15th Brazilian Power Electronics Conference and 5th IEEE Southern Power Electronics Conference (COBEP/SPEC), 2019, pp. 1-5.

[23] M. Vijayagopal, P. Zanchetta, L. Empringham, L. De Lillo, L. Tarisciotti and P. Wheeler, "Modulated model predictive current control for direct matrix converter with fixed switching frequency," 2015 17th European Conference on Power Electronics and Applications (EPE'15 ECCE-Europe), 2015, pp. 1-10.

[24] X. Liu, Z. Zeng, S. Tang, C. Zhang, D. Wang and J. Wang, "Modulated Model Predictive Control Based on Voltage-Error Vector Analysis for Direct Matrix Converter," 2020 IEEE 9th International Power Electronics and Motion Control Conference (IPEMC2020-ECCE Asia), 2020, pp. 853-857.

[25] M. Rivera et al., "Modulated model predictive control (M2PC) with fixed switching frequency for an NPC converter," 2015 IEEE 5th International Conference on Power Engineering, Energy and Electrical Drives (POWERENG), 2015, pp. 623-628.

[26] J. Xu, T. B. Soeiro, F. Gao, H. Tang and P. Bauer, "A Simplified Modulated Model Predictive Control for a Grid-Tied Three-Level T-Type Inverter," 2020 IEEE 29th International Symposium on Industrial Electronics (ISIE), 2020, pp. 618-623.

[27] J. Rodríguez, R. Heydari, Z. Rafiee, H. A. Young, F. Flores-Bahamonde and M. Shahparasti, "Model-Free Predictive Current Control of a Voltage Source Inverter," in IEEE Access, vol. 8, pp. 211104-211114, 2020.

[28] P. G. Ipoum-Ngome, D. L. Mon-Nzongo, R. C. C. Flesch, J. Song-Manguelle, M. Wang and T. Jin, "Model-Free Predictive Current Control for Multilevel Voltage Source Inverters," in IEEE Transactions on Industrial Electronics, vol. 68, no. 10, pp. 9984-9997, Oct. 2021.

[29] M. Chai, N. B. Y. Gorla and S. K. Panda, "Fault Detection and Localization for Cascaded H-Bridge Multilevel Converter With Model Predictive Control," in IEEE Transactions on Power Electronics, vol. 35, no. 10, pp. 10109-10120, Oct. 2020.

[30] R. S. Chokhawala, J. Catt and L. Kiraly, "A discussion on IGBT short-circuit behavior and fault protection schemes," in IEEE Transactions on Industry Applications, vol. 31, no. 2, pp. 256-263, March-April 1995.

[31] G. N. Brahmendra Yadav and S. Kumar Panda, "Survey of Open-circuit Fault Detection and Localization Methods Applicable to Cascaded H-bridge Multilevel Converters," IECON 2020 The 46th Annual Conference of the IEEE Industrial Electronics Society, Singapore, 2020, pp. 3988-3994.

[32] M. Chai, N. B. Y. Gorla and S. K. Panda, "Fault Detection and Localization for Cascaded H-Bridge Multilevel Converter With Model Predictive Control," in IEEE Transactions on Power Electronics, vol. 35, no. 10, pp. 10109-10120, Oct. 2020.

[33] N. B. Y. Gorla, S. Kolluri, M. Chai and S. K. Panda, "An Open-Circuit Fault Detection and Localization Scheme for Cascaded H-Bridge Multilevel Converter Without Additional Sensors," in IEEE Transactions on Industry Applications, vol. 58, no. 1, pp. 457-467, Jan.-Feb. 2022.

[34] N. B. Y. Gorla, S. Kolluri, M. Chai and S. K. Panda, "A Novel Open-Circuit Fault Detection and Localization Scheme for Cascaded H-Bridge Stage of a Three-Stage Solid-State Transformer," in IEEE Transactions on Power Electronics, vol. 36, no. 8, pp. 8713-8729, Aug. 2021.

[35] Z. Ni et al., "Control of Regenerative CHB Motor Drives at Fundamental Switching Frequency," in IEEE Transactions on Power Electronics, vol. 38, no. 3, pp. 3352-3362, March 2023.

[36] Jian Wang and Yongdong Li, "PWM rectifier in power cell of cascaded H-bridge multilevel converter," 2007 International Conference on Electrical Machines and Systems (ICEMS), Seoul, Korea (South), 2007, pp. 18-21.

[37] M. A. Perez, J. R. Espinoza, J. R. Rodriguez and P. Lezana, "Regenerative medium-voltage AC drive based on a multicell arrangement with reduced energy storage requirements," in IEEE Transactions on Industrial Electronics, vol. 52, no. 1, pp. 171-180, Feb. 2005.

[38] P. Udakhe, D. Atkar, S. Chiriki and V. B. Borghate, "Comparison of different types of SPWM techniques for three phase seven level cascaded H-Bridge inverter," 2016 IEEE 1st International Conference on Power Electronics, Intelligent Control and Energy Systems (ICPEICES), Delhi, India, 2016, pp. 1-5.

[39] S. Rahman, M. Meraj, A. Iqbal, B. P. Reddy and I. Khan, "A Combinational Level-Shifted and Phase-Shifted PWM Technique for Symmetrical Power Distribution in CHB Inverters," in IEEE Journal of Emerging and Selected Topics in Power Electronics, vol. 11, no. 1, pp. 932-941, Feb. 2023.

[40] Z. Nie, M. Preindl and N. Schofield, "SVM strategies for multiphase voltage source inverters," 8th IET International Conference on Power Electronics, Machines and Drives (PEMD 2016), Glasgow, UK, 2016, pp. 1-6.

[41] A. Singh and R. N. Mahanty, "Simulation of simplified SVM technique for three phase five-level cascaded H-bridge inverter," 2017 International Conference on Information, Communication, Instrumentation and Control (ICICIC), Indore, India, 2017, pp. 1-6.

[42] J. Muñoz et al., "Multilevel Selective Harmonic Elimination for an Asymmetric Converter," 2018 International Symposium on Power Electronics, Electrical Drives, Automation and Motion (SPEEDAM), Amalfi, Italy, 2018, pp. 485-490.

[43] G. Nalcaci and M. Ermis, "Selective harmonic elimination for three-phase voltage source inverters using whale optimizer algorithm," 2018 5th International Conference on Electrical and Electronic Engineering (ICEEE), Istanbul, Turkey, 2018, pp. 1-6, doi: 10.1109/ICEEE2.2018.8391290.

[44] A. Kavousi, B. Vahidi, R. Salehi, M. K. Bakhshizadeh, N. Farokhnia and S. H. Fathi, "Application of the Bee Algorithm for Selective Harmonic Elimination Strategy in Multilevel Inverters," in IEEE Transactions on Power Electronics, vol. 27, no. 4, pp. 1689-1696, April 2012, doi: 10.1109/TPEL.2011.2166124.

[45] Z. Ni and M. Narimani, "A New Model Predictive Control Formulation for CHB Inverters," 2020 IEEE Applied Power Electronics Conference and Exposition (APEC), New Orleans, LA, USA, 2020, pp. 2462-2466.

[46] A. Bahrami and M. Narimani, "A New Five-Level T-Type Nested Neutral Point Clamped (T-NNPC) Converter," in IEEE Transactions on Power Electronics, vol. 34, no. 11, pp. 10534-10545, Nov. 2019.

[47] A. G. Bartsch, G. H. Negri, M. S. M. Cavalca, J. de Oliveira and A. Nied, "Cost function tuning methodology for FCS-MPC applied to PMSM drives," 2017 Brazilian Power Electronics Conference (COBEP), Juiz de Fora, Brazil, 2017, pp. 1-6.

[48] X. Zhang, H. Bai and M. Cheng, "Model predictive control for PMSM drives with switching frequency optimization," 2021 IEEE 4th International Electrical and Energy Conference (CIEEC), Wuhan, China, 2021, pp. 1-6, doi: 10.1109/CIEEC50170.2021.9510607.

[49] Q. Xiao et al., "Modulated Model Predictive Control for Multilevel Cascaded H-Bridge Converter-Based Static Synchronous Compensator," in IEEE Transactions on Industrial Electronics, vol. 69, no. 2, pp. 1091-1102, Feb. 2022.

[50] J. Wang, X. Liu, Q. Xiao, D. Zhou, H. Qiu and Y. Tang, "Modulated Model Predictive Control for Modular Multilevel Converters With Easy Implementation and Enhanced Steady-State Performance," in IEEE Transactions on Power Electronics, vol. 35, no. 9, pp. 9107-9118, Sept. 2020.

[51] C. -K. Lin, C. A. Agustin, J. -T. Yu, Y. -S. Cheng, F. -M. Chen and Y. -S. Lai, "A Modulated Model-Free Predictive Current Control for Four-Switch Three-Phase Inverter-Fed SynRM Drive Systems," in IEEE Access, vol. 9, pp. 162984-162995, 2021.

[52] W. Yuchen, L. Hongmei, M. Jingkui, H. Jiandong, L. Rundong and L. Liwen, "Modulated Model-free Predictive Control of PMSM Drive System," 2019 22nd

International Conference on Electrical Machines and Systems (ICEMS), Harbin, China, 2019, pp. 1-6.

[53] C. Ma, J. Rodriguez, C. Garcia and F. De Belie, "Integration of Reference Current Slope Based Model-Free Predictive Control in Modulated PMSM Drives," in IEEE Journal of Emerging and Selected Topics in Power Electronics, vol. 11, no. 2, pp. 1407-1421, April 2023.

[54] H. Quanzhen, G. Zhiyuan, G. Shouwei, S. Yong and Z. Xiaojin, "Comparison of LMS and RLS Algorithm for Active Vibration Control of Smart Structures," 2011 Third International Conference on Measuring Technology and Mechatronics Automation, Shanghai, China, 2011, pp. 745-748.

[55] Bar-Shalom, Y., Li, R. X., & Kirubarajan, T. (2001). Estimation with Applications to Tracking and Navigation (1st ed.). Wiley-Interscience.

[56] Bar--Shalom, Y. (1996). Statistical Digital Signal Processing and Modeling (1st ed.). Wiley.

[57] Z. Ni, A. H. Abuelnaga and M. Narimani, "A New Fault-Tolerant Technique Based on Nonsymmetrical Selective Harmonic Elimination for Cascaded H-Bridge Motor Drives," in IEEE Transactions on Industrial Electronics, vol. 68, no. 6, pp. 4610-4622, June 2021.

[58] A. Abuelnaga and M. Narimani, "Open Circuit IGBT Fault Classification using Phase Current in a CHB Converter," IECON 2019 - 45th Annual Conference of the IEEE Industrial Electronics Society, 2019, pp. 4636-4641

[59] J. Lamb and B. Mirafzal, "Open-Circuit IGBT Fault Detection and Location Isolation for Cascaded Multilevel Converters," in IEEE Transactions on Industrial Electronics, vol. 64, no. 6, pp. 4846-4856, June 2017.